University of Twente

EEMCS / Electrical Engineering
Control Engineering

The Netherlands
Organization for Applied
Scientific Research

Development and Implementation of Compliant Controller On Manus Robot Arm

Ali Rıza Konuk

M.Sc. Thesis

Supervisors
prof.dr.ir. J. van Amerongen
dr.ir. Stefano Stramigioli
ir. Bart Driessen, ir. Michiel Dorrepaal

October 2004

Report nr. 025CE2004
Control Engineering
EE-Math-CS
University of Twente
P.O. Box 217
7500 AE Enschede
The Netherlands

Abstract

In this thesis three different controllers, active stiffness controller (ASC), parallel position/force regulator (PPFR), and impedance control with inner velocity loop (ICWIVL), are implemented on MISO (Multiple Input Single Output) conceptual mechanical setup of the new generation MANUS rehabilitation robotic arm. These controllers are compared with each other using the tracking and force detection performance. The performance is boasted with the addition of a state-observer. According to the experimental analysis PPFR and ICWIVL gives the best results. These controller schemes can be used for low friction and high flexible links with additional absolute encoder and torque sensor besides collocated incremental encoder. In another view point, the performances of the controllers are tested for flexible rotary joint with a large gear play in the gearbox. It is also found out that inner velocity control with outer position loop controller is high performing while compensating for gearbox backlash. Besides, the observer compensates well for the flexibility of the setup with better external force detection.

Another concept covered here is the implementation of a compliant controller on MANUS_502012. A new hybrid force/position and adaptive impedance control schemes are introduced suitably for MANUS equipped with a 6 DOF (Degree of Freedom) wrist force sensor. Schemes can work efficiently in spite of the high transmission complexity of the robot mechanical structure and interfere with the low level controller under the actuator subspace. Both of the controllers, namely force servo and impedance controller, have been implemented in MATLAB Simulink environment and run on a real-time Linux PC. Performances of the controllers are tested by using the following case studies of some of the difficult daily user tasks of the handicapped person:

a) Opening the bottle cap with the aid of four axes force-servo controller.
b) Pulling the door with the aid of two axes force-servo controller
c) Impact reduction with the use of six axes impedance controller.

Controllers are then categorized and tabulated according to applicability of these tasks. Finally, mechanical properties of the MANUS_502012 have been assessed based on the experimental outcome. As a result, the mechanical transmission of the manipulator should be reduced to improve the performance of the implemented controller.

Preface

This report is the result of the MSc. graduation project on analysis and validation of compliant control implemented on 6 degree of freedom (DOF) robotic arm. The work is done in TNO-TPD robotics laboratory in Delft under supervision of ir. Michiel Dorrepaal (TNO-TPD), ir. Bart Driessen (TNO-TPD), and dr. ir. Stefano Stramigioli (University of Twente)

The master thesis assignment for the MANUS project has been divided into three parts. The initial goal is to make a literature study on application of the compliant control methods on 6-DOF robotic manipulators. In the next stage it is supposed to make a feasibility study of compliant controller design on the 1 DOF conceptual setup of the new generation MANUS. The final goal would be the implementation of the compliant controller on existing 6 DOF MANUS manipulator.

The text is organized in three parts. First part starts with the literature study on compliant control strategies. In the Part I a survey of compliant control dating till 40's is made. Chapter 1 is an introduction to MANUS project and it defines general manipulator characteristics. Chapter 2 describes basic robotics theory. In chapter 3 the parameter identification is briefly discussed. The main topic force control is discussed in chapter 4. Second part concentrates on the application and validation of suitable compliant control strategies on 1 DOF test setup. This flexible joint torque sensor embedded setup demonstrates one conceptual design of new generation MANUS robot. In chapter 5 the mechanics and the electronics of the setup will be introduced. Then the identification of the parameters of the setup will be given in chapter 6. A model in 20-sim will be developed in chapter 7. Active stiffness control, parallel position/force regulator, impedance control with inner velocity methods will be applied to the conceptual design and the results are compared in chapter 8. The last part, Part III, will be about the implementation and validation of the compliant controller on the MANUS rehabilitation robotic arm. The part will start with introduction of screw theory in chapter 9. The necessary details of the electronics, firmware, and mechanics of the MANUS is mentioned in chapter 10. Frame assignment, forward and inverse kinematic problem solutions discussed in chapter 11. Chapter 12 is about the derivation of the MANUS Jacobians, which plays an important role for force/torque transformation. The new two controllers force servo and impedance control strategies are applied to MANUS in chapter 13. Eventually, the outcome of the thesis is given in chapter 14.

Acknowledgement

I would like to thank Professor Stefano Stramigioli for his generous patience, guidance throughout my graduation work beside his busy schedule, and for giving me the chance to be in TNO-TPD robotics labs. Here, there are two people Bart Driessen and Michiel Dorrepaal who have always supported me with their experience.

I would like to thank Dr. Nuray Kayakol for her recommendations while I was writing the literature study part. I would like to extend my thanks to all my past and present Dutch lab mates in the TNO-TPD Robotics laboratory, especially, Jasper van Weeren, Hilco Suy, and Bart Loffeld for sharing their inputs and ideas. Furthermore, there are also anonymous reviewers and thanks for their fruitful comments.

Finally, I wish to dedicate this work to my parents whose motivating support and selfless goodwill has been my constant source of inspiration, which made this work possible. Besides, there is one more person, my girl friend Fei Liu, who has supported me with her love and patience all over this work.

Contents

Part I-Literature Study

Starting from the 40's the force feedback control on robotic manipulator increased popularity. From this time up to now many researches and developments have been made to improve the performance of the controller types. In this part a collection of the publications in the literature are investigated to find the most suitable one's for the MANUS manipulator series.

We will start with the introduction of the project and discuss mechanical challenges due to the design as a background in the first chapter. Then we will talk about the MANUS robotic manipulator and give some basic knowledge and formulation on some common robotic terms. In chapter 3 we will mention the parameter identification for robotic platforms. Chapter 4 will be the formulation, experimental validation, and classification of the commonly used compliant control strategies, which can be found in the literature.

Chapter 1

Introduction

MANUS also known as ARM (Assistive Robot Manipulator) is a robotic arm attached to the wheel chair of a handicapped person who is suffering from muscle diseases such as muscular dystrophy causing the individual barely moves their limbs. MANUS assists handicapped person to fulfill their daily life needs such as drinking, eating, scratching, etc. In the rehabilitation robotics market there is an operating version supplied by Exact Dynamics™ for the use of the handicapped people. In this version the rotation of the manipulator's revolute links are controlled by non-adaptive PI controllers. The nature of PI position control makes MANUS stiff against the environment. This controller strategy may cause undesirable results such as malfunctions of the manipulator or destruction of the environment. For this reason in this report we investigate literally available active control strategies and experimentally test the most suitable two, impedance control and force servo control, for achievement of the compliant and constrained rehabilitation tasks on a 6 degree-of-freedom (6 DOF) robotic arm.

MANUS should not be confused with the other kinds of industrial manipulators since it is designed for rehabilitation. Thus, this design allows the users to command the robotic arm slowly and assistive different then the industrial manipulators which are moving fast and aggressive. Thus, the requirements of the MANUS manipulator control are not too high. As it is commanded by a disabled person the manipulator control is not necessarily required to be as fast as an industrial manipulator. Thanks to the specifications that it makes the design of the 6-dimensional control simpler even on the mobile platform in this case it is wheeled chair.

On the other hand, since the robot is designed for personal use the transmission components such as gearboxes and geared belt transmission systems are not manufactured using the high precision technologies. The main reason for this is to reduce the final cost of the personal robotic arm. As a result, this increases the gear backlash and non-linearity of the mechanism. These two factors are challenging for the design of a stable compliant controller.

In the robot force literature there are many strategies for the control of the external force exerted by the robot. After making an intensive literature search the two broad approaches, impedance control and force servo control are found applicable on the MANUS considering the required rehabilitation task achievement. In impedance control, a prescribed static or dynamic relation is sought to be maintained between the robot end-effector force and position (Hogan, N., 1985). One way to determine the impedance might be controlling the inner position/velocity parameters with respect to the observed external force. With this approach an adaptive impedance controller is designed and the compliance requirement is tested on soft

and hard materials. In force servo control, the end-effector force is equalized to zero in selected directions and the end-effector position is controlled in the remaining (complementary) directions. In this aspect the controller resembles to *implicit hybrid force* control. (Raibert, M. H., Craig, J. J., 1981, Mason, M. T., 1981). In *implicit hybrid control*, the end-effector force is controlled indirectly by modifying the reference trajectory of an inner loop joint position/velocity controller based on the sensed force error. This type of control was proposed in (De Schutter, J., van Brussel, H., 1988) with the aim of implementing force control on traditional industrial manipulators. Controllers based on this approach usually do not require the rigid body dynamical model of the robot.

This report is organized in three parts. In the first part the basic robotics theory and the result of literature study has been reported. In part II active stiffness controller (ASC), parallel position/force regulator (PPFR), and impedance control with inner velocity loop (ICWIVL), are implemented on 1-DOF conceptual mechanical setup of the new generation MANUS rehabilitation robotic arm. The compliance, trajectory and collision performance of those tested. In the final part force servo and impedance controller have been implemented on MANUS robotic arm. Performance of the controllers is tested by using the several case studies of some of the difficult daily user tasks for the handicapped person.

Chapter 2

Robot Manipulator

In this chapter we will classify and introduce the MANUS which has been used as an experimental setup for the thesis. Later, we will discuss the desired characteristics of an advanced manipulator and find-out which are satisfied by MANUS. Since our subject is compliance in rehabilitation robotics it is important to list the common daily tasks which are necessarily be achieved by a rehabilitation robot. After these concepts this chapter will introduce the robotics theory which explains the solutions of the problems such as kinematics, singularities, and dynamics.

2.1. Robot Type Classification

The MANUS robot is non-redundant manipulator since it has 6 DOF. Therefore, the redundant control strategies will not be included in this report.

Before getting involved in the theory behind the control of the robot it is better to get acquainted with the MANUS product specifications. Exact Dynamics™, the commercial distributor and the manufacturer company of the MANUS, presents their product as "The MANUS service manipulator (also known as "ARM") is a 6+1 DOF robot which assists disabled people with a severe handicap at their upper limbs". It compensates their lost arm and hand functions. It is mounted on an electric wheelchair (or mobile base) and allows numerous daily living tasks to be carried out at home, at work, and outdoors. By means of an input device like a keypad (4x4 buttons), a joystick (e.g. of the wheelchair) or another device attached to a non-disabled body part, the manipulator can be operated to grasp objects with its gripper. When it's not in use the MANUS can be conveniently folded in (parked) beside the wheelchair. World wide user studies have shown the immense benefits of the MANUS for its users. They become more self-supportive and increase their participation in society. Therefore the quality of life increases significantly.

2.2. Characteristics of an Advanced Manipulator

It is stated that (An, C.H., Atkeson, C.G., Hollerbach J.M., 1988) there is a general consensus about what characteristics an advanced manipulator system should have, and most papers on advanced robot control presume some or all of the following characteristics:

- an ideal rigid-body dynamic model of the arm
- fast speed and adequate payload capability

- accurate joint torque control
- accurate position sensing
- accurate velocity sensing
- a force control capability
- adequate bandwidth and accessibility of the robot controller
- adequate computational power for real-time implementation of advanced control algorithms

Unfortunately, there are almost no manipulators that satisfy all or even some of these characteristics. Commercial robots in fact satisfy virtually none of them, and hence cannot serve as experimental test beds for most theoretical robot control work. For MANUS, fast speed, accurate velocity sensing, and the adequate bandwidth characteristics may not be satisfied either in the requirement or due to the design of the manipulator.

One major problem with many commercial manipulators is the use of gears, necessary to amplify the limited torque capabilities of most electric motors. The gears amplify the motor torque by a factor equal to the gear ratio, allowing the robot designer to use smaller motors. Until recently, increasing the motor size to reduce the gear ratio was not feasible, due to the unfavorable scaling relation between motor torque and combined weight of the motor plus supporting structures. Gears introduce the following problems.

- *Friction and backlash.* These nonlinear effects are due to preloading, tooth wear, misalignment, and gear eccentricity. They are extremely difficult to model, although parametric models of friction have been attempted (Mukerjee, A., 1986) Rather than modeling, it seems more appropriate to minimize backlash and friction by mechanical tuning techniques (Dagalakis, N. G., Myers, D. R., 1985) . Friction torques can be so large as to dominate link dynamics. From the measurements of the MIT Artificial Intelligence Laboratory on PUMA 600 manipulator, the friction terms account for as much *at 50%* of the motor torques. (An, C.H., Atkeson, C.G., Hollerbach J.M., 1988)

- *Joint flexibility.* Particularly for robots with harmonic drives, such as the ASEA robot, the gear elements act like springs and will deflect varying amounts depending on the load and link configuration. Joint flexibility will cause loss of accuracy at the endpoint, particularly complicating kinematic calibration. It also adds undesirable transmission dynamics causing difficulties in designing a wide bandwidth controller (Good, M. C., Sweet, L. M., Strobel, K. L., 1985).

- *Speed limitations.* All electric motors have a maximum speed at which they can operate, due to back EMF and characteristics of the power amplifiers. Commercial robots often operate near this limit, but the resulting joint speed is not very fast due to the gear reduction. Moreover, the amplifiers impose a slew rate limitation, so that joint acceleration is limited. The end result is that geared robots are relatively slow, and their dynamics are dominated by gravity and friction.

- *Dominance of rotor inertias.* A gear ratio of α multiplies an electric motor's rotor inertia by α^2. Many commercial robots are designed with gear ratios that cause rotor inertia to match or dominate link inertias. For example, a typical gear ratio of 100: 1 reduces the inertia effects of the links by 10^{-4}. The end result is that the dynamics of commercial robots are well approximated by single joint dynamics, and the nonlinear rigid-body dynamic interacts can be ignored (Goor, 1985a,

1985b; Good, Sweet, and Strobel, 1985). From one standpoint, high rotor inertia is an advantage because it makes control easier: one is dealing with separable and independent joint controllers, and any payload at the end can be ignored.

When these points are taken together, geared robots such as new generation MANUS do not conform to the rigid-body dynamic models hypothesized in most theoretical robot controllers. Dynamic interactions between moving links are insignificant, because (1) rotor inertia dominates link inertia, (2) friction torques dominates inertial torques, and (3) gravity torques dominate inertial torques. Hence robot controllers for commercial robots are designed as parallel single-input, single-output systems.

A more severe problem with commercial robots is the inability to control joint torques, yet virtually all advanced control strategies are predicated on thin capability. The reasons why joint torque control is difficult to implement on commercial robots is the nonlinear joint dynamics due to gear friction and backlash make the measurement and specification of the joint torque very difficult. Motor current cannot then be used to infer the joint torque, and the alternative of mounting joint torque sensors at the output side of a gear train is problematical and seldom done (Luh, J. Y. S., Fisher, W. D, and Paul, R., 1983).

2.3. Rehabilitation Robot Tasks

Daily living tasks which are necessary to be assisted by the MANUS can be listed as follows:

- Assisting for eating and drinking
- Assisting for the use of kitchen inventory, e.g. microwave, coffeemaker
- Assisting for taking medicine
- Scratching and itching the body parts
- Personal hygiene, such as electrical shaving, brushing teeth
- Housekeeping, e.g. watering the plants
- Operating switches and buttons
- Insertion tasks, e.g. inserting a tape into VCR, inserting diskette into computer
- Leisure activities, e.g. playing chess, painting and turning pages
- Opening a door, cupboard or drawer
- Outdoor activities, e.g. shopping

These activities can be categorized in following point of view to understand in which tasks may require compliance. Mainly tasks can be summarized in three categories from easier to complex as picking, alignment, and constrained tasks, respectively.

Free Motion Task	Alignment Tasks	Constrained Tasks
Carrying a glass	Inserting the cassette into VCR	Twisting the door handle
Carrying a donut	Inserting an electric plug	Pulling a drawer

Carrying a bottle from the shop rack	Operating switch

Figure 2.3-1: Task categorization

Insertion of the cassette to the video player is one of the tasks that the robot manipulator should achieve. This task is in the category of insertion of a peg-in-hole. To accommodate the insertion of the cassette the gripper should provide high stiffness in the direction of the insertion and high compliance along the other directions. (Siciliano, B., Villani, 1999)

2.4. Basics of Robot Kinematics

The basics of the robotics theory can be found in any robotics books such as homogeneous transformations and rigid body motions. (Paul, R.P., 1981; Spong, M. W., Vidyasagar, M., 1989; Yoshikawa, T., 1990; Stramigioli, S., 2001; Sciavicco, L., Siciliano, B., 2000; Angeles, J., 1997)

David-Hartenberg frame assignment is commonly be used in robotics. In summary the steps for calculating the forward kinematics are as follows: (Spong, M. W., Vidyasagar, M., 1989)

1. Locate and label the joint axes $z_0,\ldots,z_{n-1}$
2. Establish the base frame. Set the origin anywhere on the z_0-axis. The x_0 and y_0 axes are chosen conveniently to form a right-hand frame.
3. For $i=1,\ldots,n-1$, perform Steps 3 to 5.
4. Locate the origin o_i, where the common normal to z_i, and z_{i-1} intersects z_i. If z_i, intersects z_{i-1} locate o_i at this intersection. If z_i and z_{i-1} are parallel, locate o_i, at joint i.
5. Establish x_i, along the common normal between z_{i-1} and z_i, through o_i, or in the direction normal to the z_{i-1} - z_i, plane if z_{i-1} and z_i, intersect.
6. Establish y_i, to complete a right-hand frame.
7. Establish the end-effector frame $o_n x_n y_n z_n$. Assuming the n^{th} joint is revolute, set $\mathbf{k}_n = \mathbf{a}$ along the direction z_{n-1}. Establish the origin o_n, conveniently along z_n, preferably at the center of the gripper or at the tip of any tool that the manipulator may be carrying. Set $\mathbf{j}_n = \mathbf{s}$ in the direction of the gripper closure and set $\mathbf{i}_n = \mathbf{n}$ as $\mathbf{s}\times\mathbf{a}$. If the tool is not a simple gripper set x_n and y_n conveniently form a right-hand frame.
8. Create a table of link parameters $a_i, d_i, \alpha_i, \theta_i$

   a_i = distance along x_i from o_i to the intersection of the x_i and z_{i-1} axes

   d_i = distance along z_{i-1} from o_{i-1} to the intersection of the x_i and z_{i-1} axes. d_i is a variable if joint *i* is prismatic

   α_i = the angle between z_{i-1} and z_i measured about x_i

   θ_i = the angle between x_{i-1} and x_i measured about z_{i-1}. θ_i is a variable if joint *i* is revolute

9. Form the homogeneous transformation matrices A_i by substituting the above parameters into David-Hartenberg convention.

10. Form $T_0^n = A_1 \cdots A_n$. This then gives the position and orientation of the tool frame expressed in base coordinates.

2.5. Velocity Kinematics-Jacobian

Mathematically, the forward kinematic equations define a function between the space of cartesian positions and orientations and the space of joint positions. (Spong, M. W., Vidyasagar, M., 1989) The velocity relationships are then determined by the Jacobian of this function. The Jacobian is a matrix-valued function and can be thought of as the vector version of the ordinary derivative of a scalar function. This Jacobian or Jacobian matrix is one of the most important quantities in the analysis and control of robot motion. It arises in virtually every aspect of robotic manipulation: in the planning and execution of smooth trajectories, in the determination of singular configurations, in the execution of coordinated (anthropomorphic) motion, in the derivation of the dynamic equations of motion, and in the transformation of forces and torques from the end-effector to the manipulator joints.

For an n-link manipulator we first derive the Jacobian representing the instantaneous transformation between the n -vector of joint velocities and the 6-vector consisting of the linear and angular velocities of the end-effector. This Jacobian is then a *6xn* matrix. The same approach is used to determine the transformation between the joint velocities and the linear and angular velocity of any point on the manipulator. This will be important when we discuss the derivation of the dynamic equations of motion.

Consider an n-link manipulator with joint variables $q_1, \ldots, q_n$. Let

$$T_0^n(\mathbf{q}) = \begin{bmatrix} R_0^n(\mathbf{q}) & \mathbf{d}_0^n(\mathbf{q}) \\ 0 & 1 \end{bmatrix} \tag{2.1}$$

Denote the transformation from the end-effector frame to the base frame where $\mathbf{q} = (q_1, \ldots, q_n)^T$ is the vector of joint variables. As the robot moves about, both the joint variables q_i and the end-effector position $\mathbf{d}_0^n$ and orientation R_0^n will be functions of time. The objective of this section is to relate the linear and angular velocity of the end-effector to the vector of joint velocities $\dot{q}(t)$. Let

$$S(\omega_0^n) = \dot{R}_0^n (R_0^n)^T \tag{2.2}$$

define the angular velocity vector ω_0^n of the end-effector, and let

$$\mathbf{v}_0^n = \dot{\mathbf{d}}_0^n \tag{2.3}$$

denote the linear velocity of the end effector. We seek expressions of the form

$$\mathbf{v}_0^n = J_{\mathbf{v}} \dot{\mathbf{q}} \tag{2.4}$$

$$\omega_0^n = J_{\boldsymbol{\omega}} \dot{\mathbf{q}} \tag{2.5}$$

where $J_{\mathbf{v}}$ and J_{ω} are $3 \times$n matrices. We may write (4.4) and (4.5) together as

$$\begin{bmatrix} \mathbf{v}_0^n \\ \omega_0^n \end{bmatrix} = J_0^n \dot{\mathbf{q}} \tag{2.6}$$

where J_0^n is given by

$$J_0^n = \begin{bmatrix} J_v \\ J_\omega \end{bmatrix} \tag{2.7}$$

The matrix J_0^n is called the *manipulator Jacobian* or *Jacobian* for short. Note that J_0^n is a $6 \times n$ matrix where n is the number of links. Later, the geometrical Jacobian will be introduced since it's more convenient to adapt it for the theory that is used to control the MANUS.

The above procedure works not only for computing the velocity of the end-effector but also for computing the velocity of any point of the manipulator.

2.6. Singularities

Since the Jacobian is a function of the configuration $\mathbf{q}$, those configurations for which the rank of J decreases are called *singularities* or *singular configurations*. (Hunt, K., 1978)

2.7. Theory of Robot Dynamics

A standard method deriving the dynamic equations of the mechanical systems is via the so-called Euler-Lagrange equations. (Spong, M., 1987)

$$\frac{d}{dt}\frac{\partial L}{\partial \dot{\mathbf{q}}} - \frac{\partial L}{\partial \mathbf{q}} = \tau \tag{2.8}$$

where $\mathbf{q} = (q_1, \ldots, q_n)^T$ is a set of generalized coordinates for the system, L, the Lagrangian, is the difference, $K - P$, between the kinetic energy K and the potential energy P, and $\boldsymbol{\tau} = (\tau_1, \ldots, \tau_n)^T$ is the vector of generalized forces acting on the system. An important special case, which is true of the robot manipulator, arises when the potential energy $P = P(q)$ is independent of $\dot{\mathbf{q}}$, and when the kinetic energy is the quadratic function of the vector $\dot{\mathbf{q}}$ of the form

$$K = \frac{1}{2}\sum_{i,j}^{n} d_{ij}(\mathbf{q})\dot{q}_i\dot{q}_j = \frac{1}{2}\dot{\mathbf{q}}^T D(\mathbf{q})\dot{\mathbf{q}} \tag{2.9}$$

where the $n \times n$ *inertia matrix* $D(\mathbf{q})$ is symmetric and positive definite for each $\mathbf{q} \in R^n$. The generalized coordinates in this case are the joint positions.

The Euler-Lagrange equations for such a system can be derived as follows. Since

$$L = K - P = \frac{1}{2}\sum_{i,j}^{n} d_{ij}(\mathbf{q})\dot{q}_i\dot{q}_j - P(\mathbf{q}) \tag{2.10}$$

we have that

$$\frac{\partial L}{\partial \dot{q}_k} = \sum_j d_{kj}(\mathbf{q})\dot{q}_j \tag{2.11}$$

and

$$\begin{aligned} \frac{d}{dt}\frac{\partial L}{\partial \dot{q}_k} &= \sum_j d_{kj}(\mathbf{q})\ddot{q}_j + \sum_j \frac{d}{dt} d_{kj}(\mathbf{q})\dot{q}_j \\ &= \sum_j d_{kj}(\mathbf{q})\ddot{q}_j + \sum_{i,j} \frac{\partial d_{kj}}{\partial q_i}\dot{q}_i\dot{q}_j \end{aligned} \tag{2.12}$$

Also

$$\frac{\partial L}{\partial q_k} = \frac{1}{2}\sum_{i,j}\frac{\partial d_{ij}}{\partial q_k}\dot{q}_i\dot{q}_j - \frac{\partial P}{\partial q_k} \tag{2.13}$$

Thus the Euler-Lagrange equations can be written as

$$\sum_j d_{kj}(\mathbf{q})\ddot{q}_j + \sum_{i,j}\left\{\frac{\partial d_{kj}}{\partial q_i} - \frac{1}{2}\frac{\partial d_{ij}}{\partial q_k}\right\}\dot{q}_i\dot{q}_j - \frac{\partial P}{\partial q_k}, k = 1,\ldots,n \tag{2.14}$$

By interchanging the order of summation in the second term above and taking the advantage of the symmetry of the inertia matrix, we can show that

$$\sum_{i,j}\left\{\frac{\partial d_{kj}}{\partial q_i} - \frac{1}{2}\frac{\partial d_{ij}}{\partial q_k}\right\}\dot{q}_i\dot{q}_j = \sum_{i,j}\frac{1}{2}\left\{\frac{\partial d_{kj}}{\partial q_i} + \frac{\partial d_{ki}}{\partial q_j} - \frac{\partial d_{ij}}{\partial q_k}\right\}\dot{q}_i\dot{q}_j \tag{2.15}$$

The coefficients

$$c_{ijk} = \frac{1}{2}\left\{\frac{\partial d_{kj}}{\partial q_i} + \frac{\partial d_{ki}}{\partial q_j} - \frac{\partial d_{ij}}{\partial q_k}\right\} \tag{2.16}$$

In (2.16) are known as *Christoffel symbols* (of the first kind). If we set

$$\phi_k = \frac{\partial P}{\partial q_k} \tag{2.17}$$

Then we can write the Euler-Lagrange equations (2.14) as

$$\sum_j d_{kj}(\mathbf{q})\ddot{q}_j + \sum_{i,j} c_{ijk}\dot{q}_i\dot{q}_j + \phi_k(\mathbf{q}) = \boldsymbol{\tau}_{k,} k = 1,\ldots,n \tag{2.18}$$

In the above equation there are three types of terms. The first involve the second derivative of the generalized coordinates. The second are quadratic terms in the first derivatives of the **q**, where the coefficients may depend on **q**. These are further classified into two types. Terms involving a product of the type $\dot{q}_i^2$ are called *centrigugal*, while those involving a product of the type $\dot{q}_i\dot{q}_j$, where $i \neq j$, are called *Coriolis* terms. The third type of terms is those involving only **q** but not its derivatives. Clearly the latter arise from differentiating the potential energy.

It is common to extend the well-known dynamic equation (2.18) of a general rigid manipulator having n degree of freedom by adding the external force term as

$$D(\mathbf{q})\ddot{\mathbf{q}} + C(\mathbf{q},\dot{\mathbf{q}}) + g(\mathbf{q}) + J^T(\mathbf{q})F = \boldsymbol{\tau} \tag{2.19}$$

where $q \in R^n$ is the joint revolution vector, $\tau \in R^n$ is the applied joint torque, $D(q) \in R^{n\times n}$ is the inertia matrix, $C(q,\dot{q})\dot{q} \in R^n$ is the vector function characterizing *Coriolis* and *centrifugal forces*, $g(q) \in R^n$ is the gravitational force, $J(q) = \partial x(q)/\partial q \in R^{n\times n}$ is the Jacobian matrix which is assumed to be non-singular in finite work space, and $x \in R^n$ is the position and angles the end-effector in Cartesian space, $F \in R^n$ is the vector of forces/moments on the environment exerted by the robot at the end-effector. (corresponding to x, forces are decomposed along the Cartesian axes, and moments are decomposed along the rotation axes defining the angles, which may not be orthogonal)

Chapter 3

Dynamic Parameter Identification

A major practical step for the implementation of the proposed controller structure is the parameter identification. The identification step is mutually dependent to the mechanical design of the robotic system. Because of the large number of dynamic parameters, it's necessary to divide them in several groups, which were identified separately.

Basic steps for identification of robot parameters, estimation of link inertial parameters, estimation of load inertial parameters can be found in (An, C.H., Atkeson, C.G., Hollerbach J.M., 1988) Friction parameters were identified based on current, torque and speed measurements on relevant trajectories for the whole robot. (Spong, M. W., Vidyasagar, M., 1989) The FEM evaluation for the joint elasticity was not precise enough, so we determined it from the joint oscillation frequency, knowing the inertia. For the new robot, the available sensors enable online computation of the elasticity. (Spong, M. W., Vidyasagar, M., 1989)

Although the characteristics of the current controlled motors can be identified together with the friction parameters, this leads to a bad conditioning of the optimization problem. Therefore the motor parameters were also identified separately using a motor testbed. (Spong, M. W., Vidyasagar, M., 1989)

Chapter 4

Force Control Strategies

In this chapter some of the common used force control strategies are summarized.(Chiaverini, S., Siciliano, B., Villani, L., 1999). It is stated that when in contact, the end-effector position is constrained along certain task-space directions by the presence of the environment, and a suitable compliant behavior of the manipulator is required to accommodate the interaction. The basic strategy to achieve this purpose is stiffness control (Salisbury, J.K., 1980) which corresponds to proportional-derivative (PD) control with gravity compensation. The amount of the proportional gain sets the manipulator (active) stiffness which has to be properly tuned versus the surface (passive) stiffness.

Stiffness control is designed to achieve a desired static behavior of the interaction. In order to achieve a desired dynamic behavior, the actual mass and damping at the contact are to be considered besides the stiffness, leading to impedance control. (Hogan, N., 1985) The resulting impedance is a function of the manipulator configuration; measurement of contact force is needed to obtain configuration-independent impedance.

A common shortcoming of the above strategies is that the contact force is controlled only indirectly by acting on the impedance parameters. An effective way to realize direct force control (Whitney, D.E., 1977) is to close an outer force feedback loop around an inner velocity or position feedback loop (De Schutter, J., van Brussel, H., 1988), where an integral action on the force error is typically needed to regulate the contact force to a desired value (Volpe, R., Khosla, P., 1993).

In order to provide motion control capabilities, the parallel force/position control approach can be adopted (Chiaverini, S., Sciavicco, L., 1993), where a position feedback loop acts in parallel to a force feedback loop. Dominance of the force control action ensures force regulation along the constrained task-space directions, while the position control action can be designed to achieve either regulation or tracking of the end-effector position along the unconstrained task-space directions.

All of the above strategies are conceived to handle interaction without knowledge of a geometric description of the contact. It should be clear, however, that it is advantageous to exploit such information whenever available, so as to discriminate between task components to be force controlled and task components to be position controlled (Mason, M. T., 1981), leading to the well-known hybrid position/force control (Raibert, M. H., Craig, J. J., 1981) and subsequent developments and improvements (Yoshikawa, T., 1987).

So far a survey of several interaction control schemes that are developed according to the strategies of stiffness control, impedance control, force control, parallel force/position control, and hybrid control is presented.

Note that the advanced adaptive force control strategies will not be treated here.

4.1. Classification

Strategies described before can be put into two classes, namely, those using static model-based compensation, and those using dynamic model-based compensation. The former class is aimed at guaranteeing good system performance at steady state and, thus, the only requirement is the knowledge of manipulator kinematics and gravity torques; impedance control with static model-based compensation (hereafter called stiffness control), force control, and parallel force/position regulator are considered. On the other hand, the latter class is aimed at enhancing the behavior of the system during the transient and, thus, it is required to know the full dynamic model and have a force sensor; impedance control with dynamic model-based compensation (hereafter called impedance control), impedance control with inner position loop, force control with inner velocity loop, force control with inner position loop, and parallel force/position control are considered.

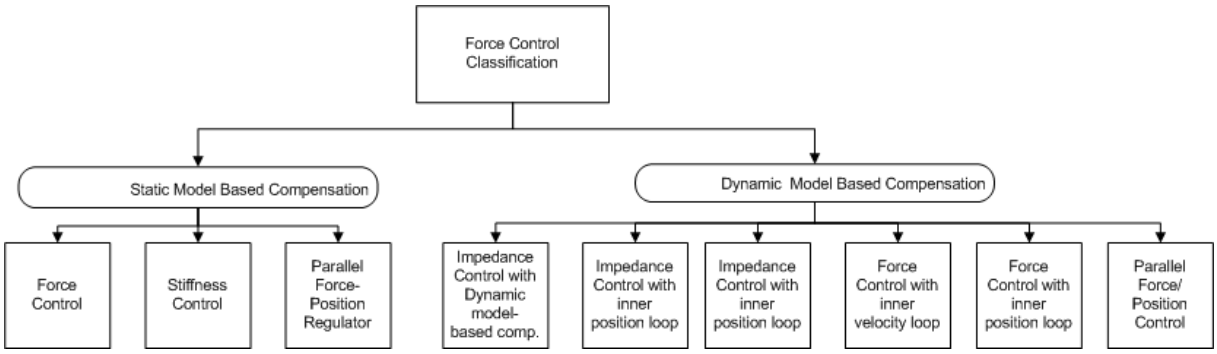

Figure 4.1-1: Force control classification

4.2. Static Model-based Compensation

This class of schemes is aimed at guaranteeing good system performance at steady state. Hence, the only model-based compensation requirements concern static terms, i.e., the manipulator Jacobian and the gravity torques. (Chiaverini, S., Siciliano, B., Villani, L., 1999)

4.2.1. Stiffness(Compliance) Control

Stiffness control (Salisbury, J.K., 1980) derives from a position control scheme of PD type with gravity compensation. Let p_d denote the desired end-effector position; the driving torques are chosen as

$$\tau_d = J^T(\mathbf{q})k_p(\mathbf{p}_d - \mathbf{p}) - k_v\dot{\mathbf{q}} + \mathbf{g}(\mathbf{q}) \tag{4.1}$$

where k_p is the gain of an active stiffness on the end-effector position error, and k_v is the gain of a joint damping action. The purpose of this control is to make the end effector compliant with respect to contact forces by acting on k_p. For such a reason, this strategy is also referred to in the literature as (active) compliance control; also, since damping is controlled besides stiffness, the control law (4.1) can be regarded as an impedance control (Hogan, N., 1985) with static model-based compensation. Notice that no force measurement is required.

Stability analysis of the closed-loop system under control (4.1) derives from the seminal work in (Takegaki, M., Arimoto, S., 1981) using energy-based Lyapunov functions and is discussed in, e.g., (Takegaki, M., Arimoto, S., 1981)

To demonstrate the performance of the stiffness control a case study was developed by (Chiaverini, S., Siciliano, B., Villani, L., 1999) The experimental results are shown below

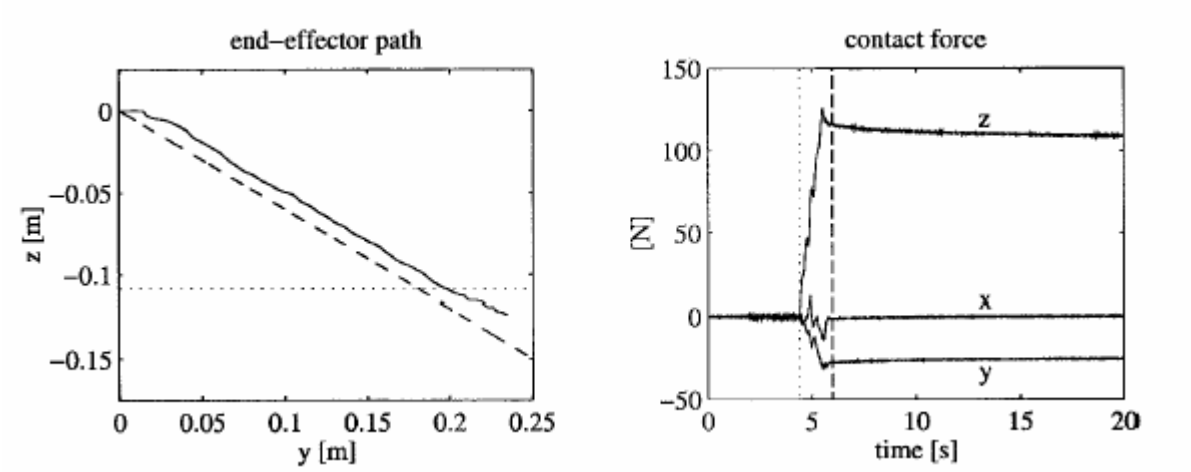

Figure 4.2-1: Experimental results under stiffness control

In the experiment the robot manipulator 3 DOF links hits to cupboard along z axis. Meanwhile the manipulator also moves along the y-axis to demonstrate the constraint motion.

The results are presented in Figure 4.2-1 in terms of the desired (dashed) and the actual (solid) end-effector path, together with the time history of the contact force; in order to facilitate interpretation of the results, the approximate location (dotted) of the surface is illustrated on the plot of the end-effector path, while the instant of contact (dotted line) and the instant of the end of the motion trajectory (dashed line) are evidenced on the plot of the contact force.

It can be recognized that path tracking accuracy is rather poor during execution of the whole task. On the other hand, the contact force along *z* reaches a steady-state value, but its amount is rather large. Reduction of the contact force could be obtained by decreasing k_p, although at the expense of a larger end-effector position error. If a force sensor were available, k_p could be conveniently adjusted before and after the contact as a function of the measured force.

Finally, notice the presence of an appreciable value of contact force along *y* at steady state due to contact friction, which was not modeled in the above analysis.

4.2.2. Force Control

This control type (Whitney, D.E., 1977) is suitable to regulate only the contact force without controlling the position. There are different approached to design the control law. Some of them will be included in the following parts.

In this section (Spong, M. W., Vidyasagar, M., 1989) discusses pure force control, which in theory should be the best way to control both the transient and steady state forces exerted by the manipulator on the environment.

The control along a single degree-of-freedom is discussed in here. Given a compliance frame together with a set of natural constraints this approach gives a method of controlling the end-effector force along directions in which a natural position constraint exists.

Consider the simplified system shown in Figure 9-14 consisting of an end-effector contacting the environment along the direction labeled x. The environment is modeled as a second order system consisting of inertia M_e stiffness k_e, and damping B_e. The environment inertia M_e consists of everything beyond the wrist force sensor, for example the inertia of the end-effector itself plus the inertia of any tool in the gripper, etc. The stiffness k_e includes the compliance of the surface being contacted as well as any passive compliance of the wrist and the stiffness of the force sensor itself. The equation governing the behavior of this system is then

$$M_e\ddot{x} + B_e\dot{x} + k_e x = F - F_{dist} \tag{4.2}$$

where F is the (input) force exerted by the end-effector and F_{dist} is a disturbance force.

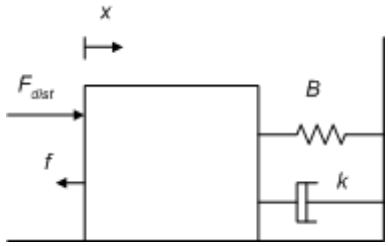

Figure 4.2-2: Mass-damper system

Suppose we desire to regulate the force exerted on the environment. In the absence of disturbances then this force is given by $F_e = k_e x$. In terms of the variable F_e equation (4.2) can be written

$$\ddot{F}_e + \frac{B_e}{M_e}\dot{F}_e + \frac{k_e}{M_e}F_e = \frac{k_e}{M_e}(F - F_{dist}) \tag{4.3}$$

If a desired force trajectory is now given as $F_e^d(t)$ then a feed-forward control scheme analogous to the position control law can now be employed. In other words by choosing the input force

$$F = -K_1 F_e - K_2\dot{F}_e + \phi(t) \tag{4.4}$$

where $\phi(t)$ is as yet an unspecified feed-forward signal, we may achieve tracking and disturbance rejection in the same way as in the position control.

In the case of the force control law (4.4), however, the robustness issues are again quite difficult. Since the force measurements F_e are noisy in practice, it is difficult to obtain the term $\dot{F}_e$ in (4.4). Using the linear relationship $F_e = k_e x$, we may use $k_e\dot{x}$ in place of $\dot{F}$, but this requires first that the environment force be a linear function of the position x and second that the stiffness k_e be accurately known.

Another type belongs to this category is the force control of (Chiaverini, S., Siciliano, B., Villani, L., 1999) Force control can be entrusted to the adoption of a proportional-integral (PI) action on the force error plus desired force feedforward. Let f_d denote the constant desired contact force which shall be aligned with n being the unit vector of direction the driving torques are chosen as

$$\boldsymbol{\tau}_d = J^T(\mathbf{q})(k_p(\mathbf{p}_f - \mathbf{p}) + f_d) - k_v\dot{\mathbf{q}} + \mathbf{g}(\mathbf{q}) \tag{4.5}$$

with

$$\mathbf{p}_f = k_c(f_d - f) + k_{ic}\int_0^t (f_d - f)d\tau \tag{4.6}$$

where k_c is the gain of a proportional action on the force error, and k_{ic} is the gain of an integral action on the force error. Notice in (4.5) that an inner loop on the end-effector position is used, which, in turn, corresponds to leaving the proportional action for motion control in the task space; this is in accordance with the fact that a position feedback loop is usually available in an industrial robot controller.

In order to show the performance of force control, a case study was developed on the experimental setup of PRISMA lab industrial robot, Comau SMART-3 S.

The end effector was placed but, of course, no trajectory could be assigned to the end-effector position. The desired force along *z* was taken to 20 N according to a trapezoidal velocity profile with cubic blends, and null initial and final first and second time derivatives, and duration of 2 s. The constant value was kept for the remaining portion of the task.

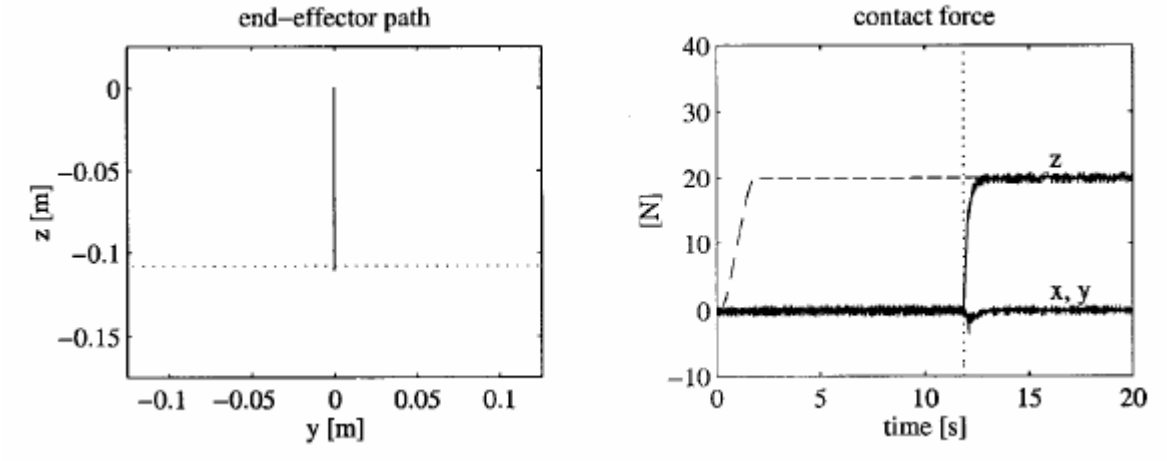

Figure 4.2-3: Experimental results under force control

Initially, the desired force trajectory causes a downward vertical motion, since the end effector is required to push in the air; this brings the end effector to come in contact with the surface at t = 12 s. Then, the contact force is successfully regulated to the desired value. The components of contact friction force along x and y are nearly zero, since no motion is commanded along those directions.

4.2.3. Parallel Force/position Regulator

In order to combine the features of stiffness control and force control, a parallel force/position regulator can be designed; where a PI force control action plus desired force feedforward is used in parallel to a PD position control action. (Chiaverini, S., Siciliano, B., Villani, L., 1999) The driving torques is chosen as

$$\tau_d = J^T(\mathbf{q})(k_p(\mathbf{p}_d - \mathbf{p}) + f_d + k_f(f_d - f) + k_i\int_0^t (f_d - f)d\tau) - k_v\dot{\mathbf{q}} + \mathbf{g}(\mathbf{q}) \tag{4.7}$$

where the integral action on the force error ensures dominance of the force loop over the position loop.

Stability of the closed-loop system under control of (4.7) using the energy-based Lyapunov functions is discussed in (Chiaverini, S., Siciliano, B., Villani, L., 1994)

In order to show the performance of parallel force/position regulator, a case study was developed on the experimental setup of PRISMA lab.

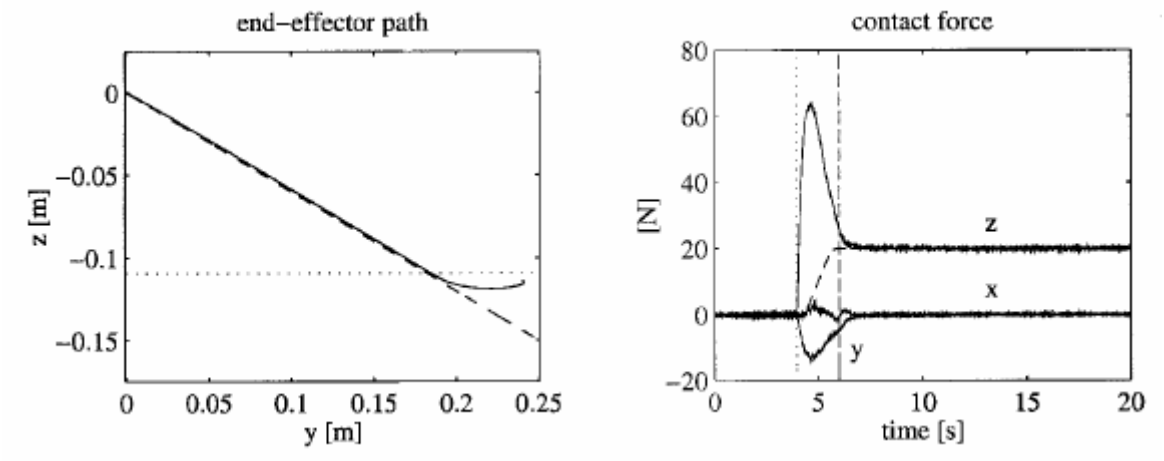

Figure 4.2-4: Experimental results under parallel force/position regulator

It can be recognized from the Figure 4.2-4 that path tracking accuracy is satisfactory during unconstrained motion, even with a simple PD position control action plus gravity compensation. On the other hand, during constrained motion, after a transient the contact force reaches the desired value; the peak on the component along *z* is due to the nonnull value of end-effector velocity at the contact, as well as to the imposed motion into the surface, whereas the appreciable deviation from zero of the component along *y* can be inputted to contact friction and local deformation of the surface resulting from the imposed end-effector motion.

In any case, both components of contact friction force along *x* and *y* are regulated to zero in view of the integral action on all the components of the force error, whereas the component along *z* reaches a steady-state value which guarantees exact force regulation according to (13) and (14).

4.2.4. Hybrid Control

Given a compliance frame we wish to design a position control law along force constrained directions and a force control law along the position controlled directions.

To implement the hybrid position/force scheme we now design both a position and a force control law for each degree of freedom and implement the overall control through the use of so-called selection matrices. (Spong, M. W., Vidyasagar, M., 1989) Such an overall control scheme is shown in Figure 4.2-5.

The Cartesian positions and the velocities are computed from the joint positions and velocities, respectively, by direct or forward kinematics. (Raibert, M. H., Craig, J. J., 1981) Neglecting the integral terms,

$$\boldsymbol{\tau}_d = \mathbf{K}_{pj}\mathbf{J}^{-1}\mathbf{S}(\mathbf{x}_d - \mathbf{x}) + \mathbf{K}_{vj}\mathbf{J}^{-1}\mathbf{S}(\dot{\mathbf{x}}_d - \dot{\mathbf{x}}) + \mathbf{K}_f\mathbf{J}^T(\mathbf{I} - \mathbf{S})(\mathbf{f}_d - \mathbf{f}) \tag{4.8}$$

Where $\mathbf{x}$ and $\mathbf{x}_d$ are the actual and desired Cartesian positions, $\mathbf{f}$ and $\mathbf{f}_d$ are the actual and desired external forces, $\mathbf{J}$ is the Jacobian matrix, $\mathbf{K}_{pj}$ and $\mathbf{K}_{vj}$ are the position and velocity gain matrices in task space, $\mathbf{I}$ is the identity matrix, and $\mathbf{S}$ is the diagonal selection matrix. The (i, i) entry of S is 1 if the i^{th} axis is to be position controlled, and 0 if it is to be force controlled.

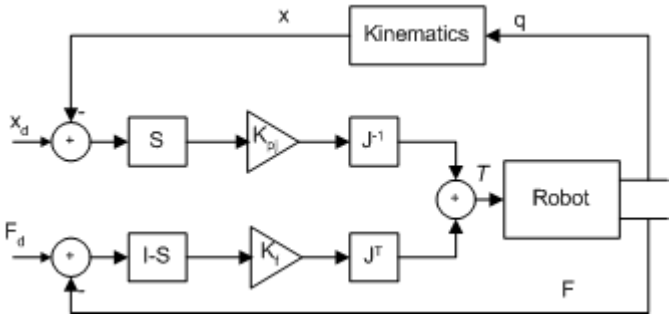

Figure 4.2-5: Hybrid controller shown without the velocity terms

The selection matrix $\mathbf{S}$ shown is a diagonal matrix with a 1 on the diagonal entries corresponding to degrees of freedom in the compliance frame that are to be position controlled. Note that $\mathbf{I}-\mathbf{S}$ automatically is a diagonal matrix with a 1 on the diagonal entries corresponding to degrees-of-freedom that are to be force controlled. In this way each degree-of-freedom is uniquely specified as being either position controlled or force controlled. The previously derived position and force control strategies can now be inserted into this control architecture.

As a conclusion, this controller requires information about the contact surface. For this reason this controller may not be used for MANUS.

4.3. Dynamic Model-based Control

In order to enhance the dynamic behavior of the system, full compensation of the terms in the dynamic model, as well as force measurement, are needed. (Chiaverini, S., Siciliano, B., Villani, L., 1999)

According to the well-known concept of inverse dynamics (Luh, J.Y.S., Walker, M.W., Paul, R.P.C., 1980), the driving torques are chosen as

$$\tau_d = B(\mathbf{q})J^{-1}(\mathbf{q})(\mathbf{a}-\dot{J}(\mathbf{q},\dot{\mathbf{q}})\dot{\mathbf{q}})+C(\mathbf{q},\dot{\mathbf{q}})\dot{\mathbf{q}}+\hat{\mathbf{d}}(\mathbf{q},\dot{\mathbf{q}})+\mathbf{g}(\mathbf{q})+J^T(\mathbf{q})\mathbf{f} \tag{4.9}$$

where $\hat{\mathbf{d}}$ denotes the available estimate of the friction torques and $\mathbf{f}$ is the measured contact force.

Notice that it is reasonable to assume accurate compensation of the terms in the dynamic model (1), e.g., as obtained by a parameter identification technique (Caccavale, F., Chiacchio, P., 1994) except for the friction torques. To the scope of the present work, the following model of friction has been used in the implementation of (4.9):

$$\hat{\mathbf{d}} = \mathbf{D}\dot{\mathbf{q}} \tag{4.10}$$

which corresponds to the including joint viscous friction only.

Substituting the control law (4.9) in dynamic equation of the robot and accounting for the time derivative of end-effector position/rotation gives

$$\ddot{\mathbf{p}} = \mathbf{a}-\eta \tag{4.11}$$

that is a resolved end-effector acceleration for which the term

$$\eta = JB^{-1}(\mathbf{d}-\hat{\mathbf{d}}) \tag{4.12}$$

can be regarded as a disturbance. In the case of mismatching on other terms in the dynamic model, such a disturbance would include additional contributions. The new control input $\mathbf{a}$ is available to provide interaction control capabilities.

A drawback of inverse dynamics control is that tracking control performance relies on the feedback linearization of the system.

4.3.1. Impedance Control

Impedance control (Hogan, N., 1985) is aimed at realizing a desired dynamic relationship between end-effector position and contact force. This behavior was already achieved by the stiffness control, but, thanks to the use of a dynamic model-based compensation, now the impedance behavior can be assigned independently of the manipulator dynamics. The new control input in (4.11) is chosen as

$$\mathbf{a} = \ddot{\mathbf{p}}_d + \frac{\mathbf{d}_d}{m_d}(\dot{\mathbf{p}}_d - \dot{\mathbf{p}}) + \frac{k_d}{m_d}(\mathbf{p}_d - \mathbf{p}) - \frac{1}{m_d} f \tag{4.13}$$

where the parameters m_d, d_d, and k_d are, respectively, the mass, damping, and stiffness of the desired mechanical impedance between the end-effector position error and the contact force, unless for the disturbance. The closed-loop system dynamic behavior is described by

$$m_d(\ddot{\mathbf{p}}_d - \ddot{\mathbf{p}}) + \mathbf{d}_d(\dot{\mathbf{p}}_d - \dot{\mathbf{p}}) + k_d(\mathbf{p}_d - \mathbf{p}) = f + m_d\eta \tag{4.14}$$

Notice that feedforward desired acceleration and velocity terms are usually not present in the impedance equation, so as to guarantee passivity of the system when the end effector is in contact with the environment. Notwithstanding, such terms are introduced to the purpose of ensuring full end-effector trajectory tracking before contact and tracking along the unconstrained task-space directions after contact.

On the other hand, the behavior of the system at steady state is substantially equivalent to that with stiffness control, where k_d in (4.13) plays the role of k_p of stiffness control law.

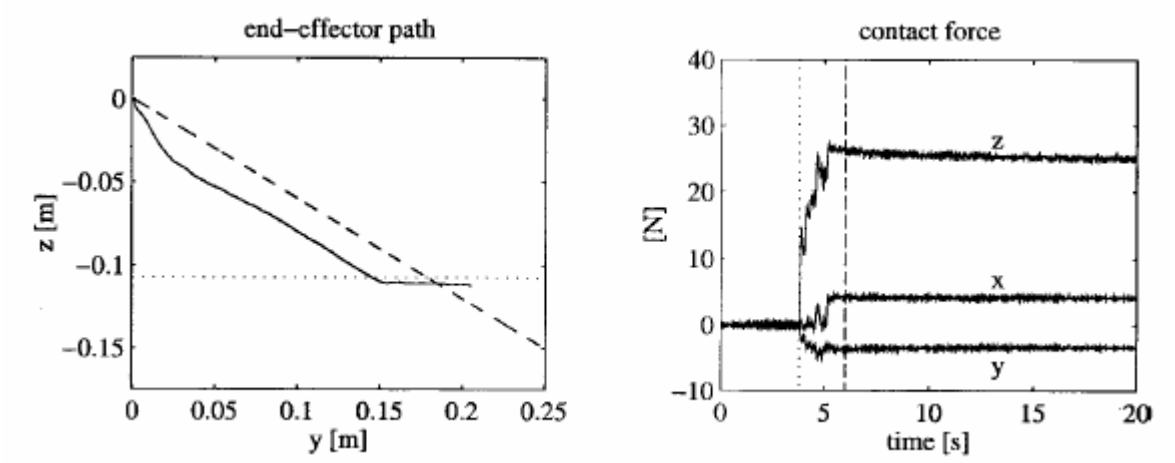

Figure 4.3-1: Experimental results under impedance control

It can be recognized that path tracking accuracy is poor during execution of the whole task; this is imputable to the disturbance term on the right-hand side of (4.14). On the other hand, the contact force along *z* is limited during the transient and reaches a constant value at steady state. Improvement of the position tracking accuracy might be achieved by increasing *kd,* however, this would give rise to larger contact forces. Finally, notice the presence of an appreciable value of contact friction force along both *x* and *y* at steady state, which is caused by the end-effector position deviation along both *x* and *y* (although the former is not visible in the figure).

In order to improve path tracking accuracy, an approximate compensation of static friction at the joints can be added to (4.10), e.g. as

$$\hat{\mathbf{d}} = \mathbf{D}\dot{\mathbf{q}} + \mathbf{d}_c \tag{4.15}$$

where the i^{th} component of vector d_c is given by the model

$$\mathbf{d}_{ci} = \begin{cases} \mathbf{D}_{ci}\,\mathrm{sgn}(\dot{\mathbf{q}}_i), & |\dot{\mathbf{q}}_i| \geq \dot{\mathbf{q}}_{si} \\ \dfrac{\mathbf{D}_{ci}}{\dot{\mathbf{q}}_{si}}\dot{\mathbf{q}}_i, & |\dot{\mathbf{q}}_i| < \dot{\mathbf{q}}_{si} \end{cases} \tag{4.16}$$

where the D_{ci}*'s are* the estimated Coulomb friction coefficients and the $\dot{q}_{si}$*'s are* suitable velocity thresholds.

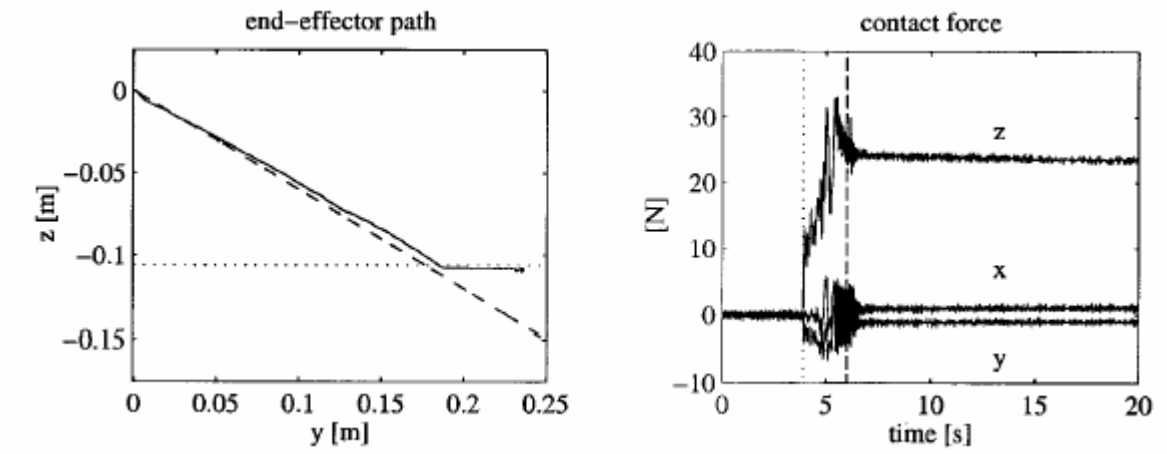

Figure 4.3-2: Experimental results under impedance control with Coulomb friction compensation

The same case study as above was developed. The results in Figure 4.3-2 show that path tracking accuracy is improved, although at the expense of an undesirable chattering behavior on all components of contact force; this phenomenon, due to the Coulomb friction compensating term, could be mitigated by choosing a wider threshold, but tracking accuracy would then become worse again. Therefore, in the remainder, compensation of static friction is no longer considered.

4.3.2. Impedance Control with Inner Position Loop

In order to reduce the effects of the disturbance term $\boldsymbol{\eta}$ on the system, a modified impedance control scheme can be designed by introducing an inner position loop. (Chiaverini, S., Siciliano, B., Villani, L., 1999) The new control input in (4.11) is chosen as

$$\mathbf{a} = \ddot{\mathbf{p}}_r + \frac{k_v}{k_a}(\dot{\mathbf{p}}_r - \mathbf{p}) + \frac{k_p}{k_a}\left(\mathbf{p}_r - \mathbf{p}\right) \tag{4.17}$$

where k_p, k_v, and k_a are the gains of the inner position control loop, the reference p_r of which is the solution to

$$m_d(\ddot{\mathbf{p}}_d - \ddot{\mathbf{p}}_r) + \mathbf{d}_d(\dot{\mathbf{p}}_d - \dot{\mathbf{p}}_r) + k_d(\mathbf{p}_d - \mathbf{p}_r) = f \tag{4.18}$$

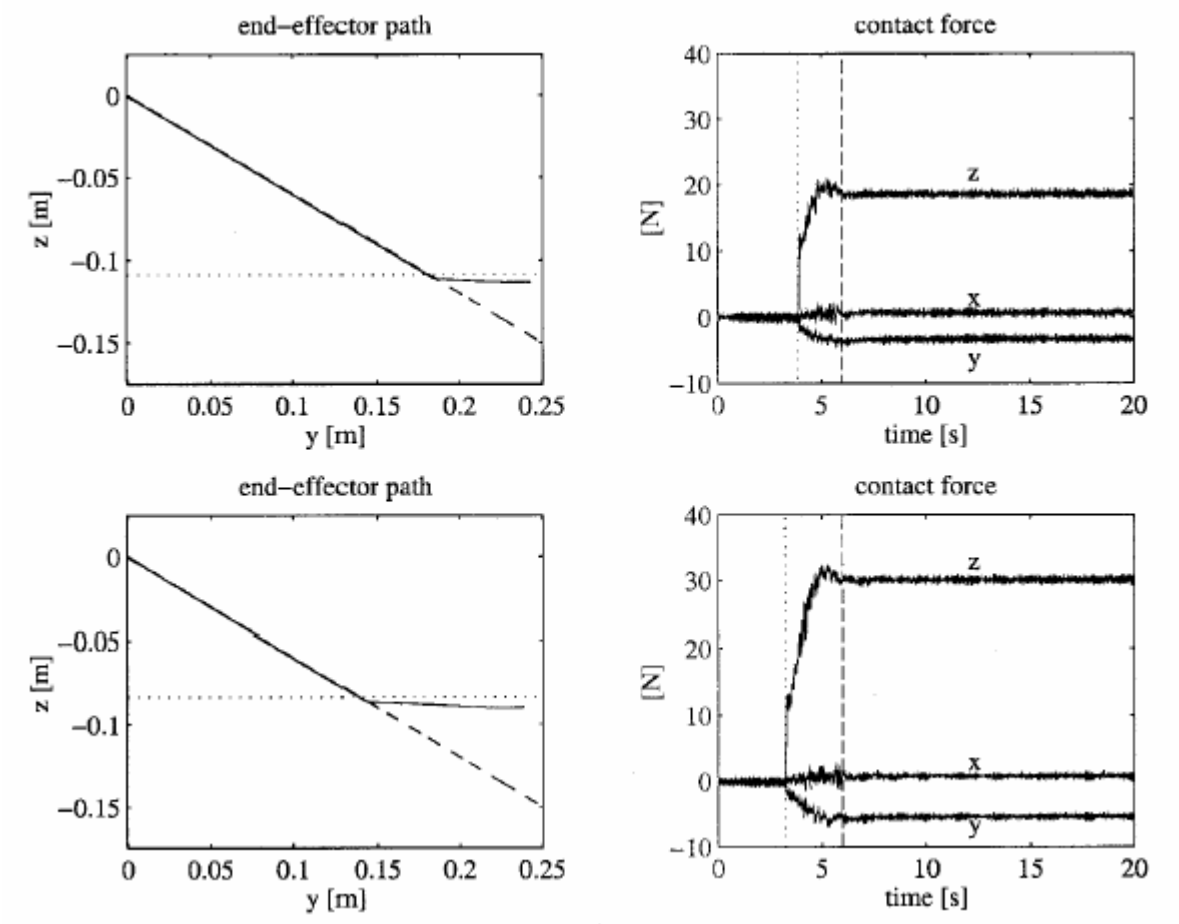

Figure 4.3-3: Experimental results under impeadance control with inner position loop

From the experiments of (Chiaverini, S., Siciliano, B., Villani, L., 1999) it can be recognized that path tracking accuracy is noticeably improved with respect to that obtained with the previous scheme and now is very good; this confirms the effective rejection of the disturbance thanks to the inner position loop. In this respect, this scheme does not suffer from lack of compensation of static friction which, thus, becomes unnecessary.

On the other hand, the contact force along z is still limited during the transient and reaches an approximate value of 20 N at steady state, as wished with the choice of k_d above. As before, an appreciable value of contact friction force along y occurs that remains at steady state, while the good end-effector tracking accuracy essentially causes no contact friction along x by maintaining the motion in the yz plane.

To investigate robustness of the scheme with respect to changes in the environment location, the task was repeated with the same impedance parameters and inner position loop gains as before, but the cardboard box was raised by about 0.025 m. From the results presented in the lower part of Fig. 8, it can be recognized that the imposed motion would require the end effector to penetrate into the surface by a larger amount and, thus, the same value of k_d gives rise to a different (larger in this case) contact force at steady state. It is worth noticing that the larger value of contact force yields larger contact friction as well.

4.3.3. Parallel Force/Position Control

This control method develop from the hybrid force/position control technique which was first introduced by (Raibert, M. H., Craig, J. J., 1981)

In order to combine the features of impedance control and force control, a parallel force/position control can be designed which has capabilities of controlling contact force along the unconstrained task-space direction and end-effector position along the constrained task-space directions. The new control input in resolved acceleration control is chosen as the sum of a position control action and a force control action

$$\mathbf{a} = \mathbf{a}_p + \mathbf{a}_f \tag{4.19}$$

where $\mathbf{a}_f$ shall prevail over $\mathbf{a}_p$, so as to effectively handle the interaction.

In the face of the robustifying action provided by the inner position loop for both the above impedance and force control schemes, the two control actions are selected as

$$\mathbf{a}_p = \ddot{\mathbf{p}}_d + \frac{k_v}{k_a}(\dot{\mathbf{p}}_d - \dot{\mathbf{p}}) + \frac{k_p}{k_a}(\mathbf{p}_d - \mathbf{p}) \tag{4.20}$$

$$\mathbf{a}_f = \ddot{\xi} + \frac{k_v}{k}\dot{\xi} + \frac{k_p}{k}\xi \tag{4.21}$$

where ξ is the solution of

$$\ddot{\xi} + \frac{k_b}{k_a}\dot{\xi} = \frac{k_f}{k_a}(f_d - f) \tag{4.22}$$

The experimental results of this control strategy again demonstrated by (Chiaverini, S., Sciavicco, L., 1993)

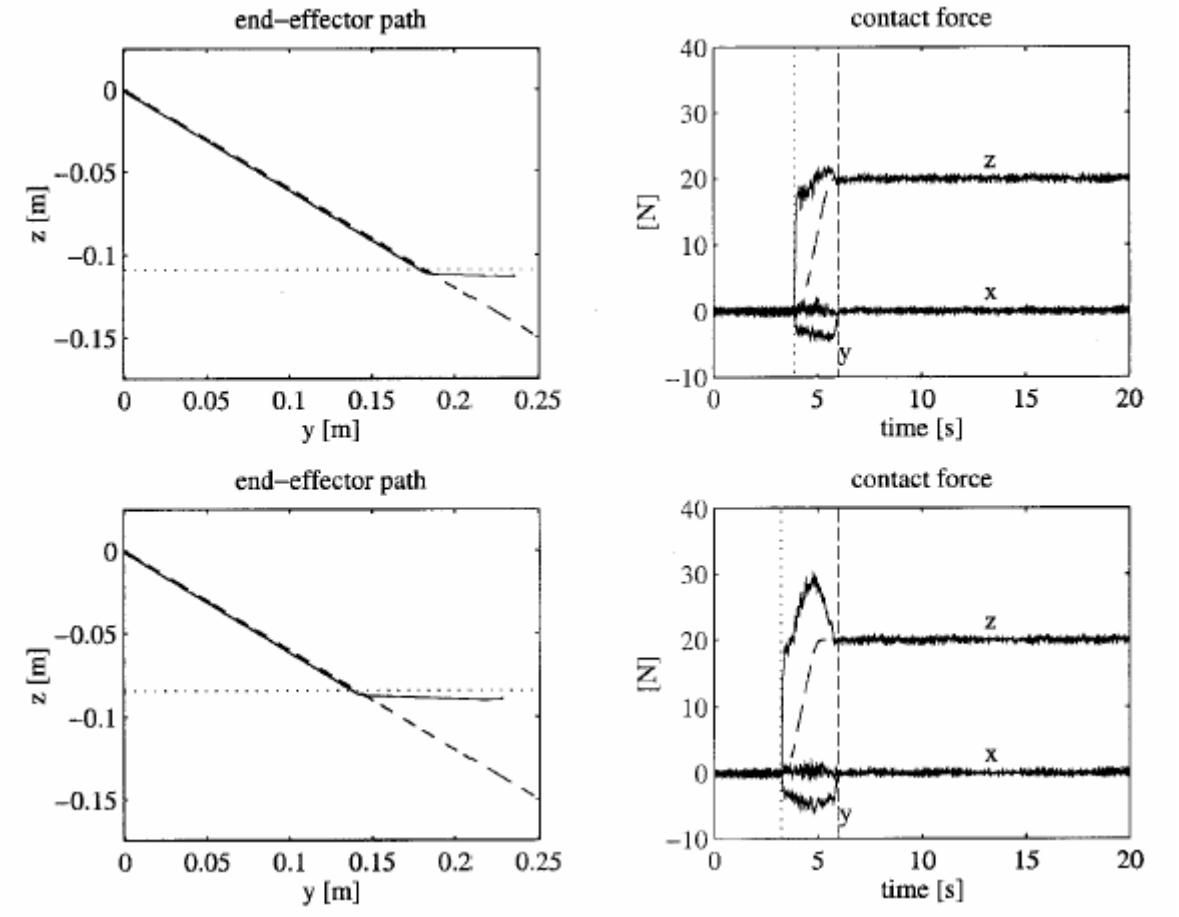

Figure 4.3-4: Experimental results under parallel force/position control

It can be recognized that path tracking accuracy is very good during unconstrained motion. On the other hand, the response of the contact force is faster than that with parallel regulator, for the same motivation regarding inverse dynamics as in the previous case study. As a consequence, the peak on the contact force along z is greatly reduced and successful regulation to the desired value is achieved. A smaller deformation of the surface occurs which also contributes to reducing the contact friction force along y by a factor of about two.

Part II – 1-DOF Compliant Control Implementation and Validation

The essential goal in this project is to implement a stable and robust compliant controller on the MANUS for operation in an unstructured environment while leaving the user in the loop. For this reason in an unstructured environment the compliance of the robotic arm is vital to prevent damage and hazardous situation.

This part is intended for application of a suitable controller introduced in the first part and demonstration of the result. In this part following chapters includes the modeling, control, and identification theories, methods and the experiments on the one-degree of freedom (1-DOF) setup of the new generation MANUS (ARM) rehabilitation robotics manipulator. The findings here will supply information for the controller design on the new generation MANUS.

The report is organized as follows. Chapter 5 describes the electronic and mechanical design of the 1-DOF setup. Chapter 6 is about overall identification procedure of 1-DOF setup. Chapter 7 describes the dynamical 20-sim model with the simulation results. The main issue, control strategies, is discussed in Chapter 8. In Chapter 9 we will give an introduction to screw theory which will be used in the next part.

Chapter 5

Experimental 1-DOF Setup

After reading this chapter the reader will get insight into the 1-DOF setup that demonstrates the link wise functional mechanical model of the new generation MANUS robotic manipulator. The design details of the mechanics and electronics will be elaborated in here part by part. The control strategies introduced in the next sections will base on the details given here.

5.1. Setup Mechanics

For the next generation of the robotic arm the mechanical structure seen in the Figure 5.1-1 is designed. This structure is intended to be used in every link of the manipulator and therefore the analysis of the mechanical setup in control point of view is vital for the robot controller design. All of the experiments explained in the following sections are implemented on this mechanical setup with horizontal and vertical configurations. Additionally, in order to include the gravity effect due to the robot link configuration payload is mounted on the arm of the model.

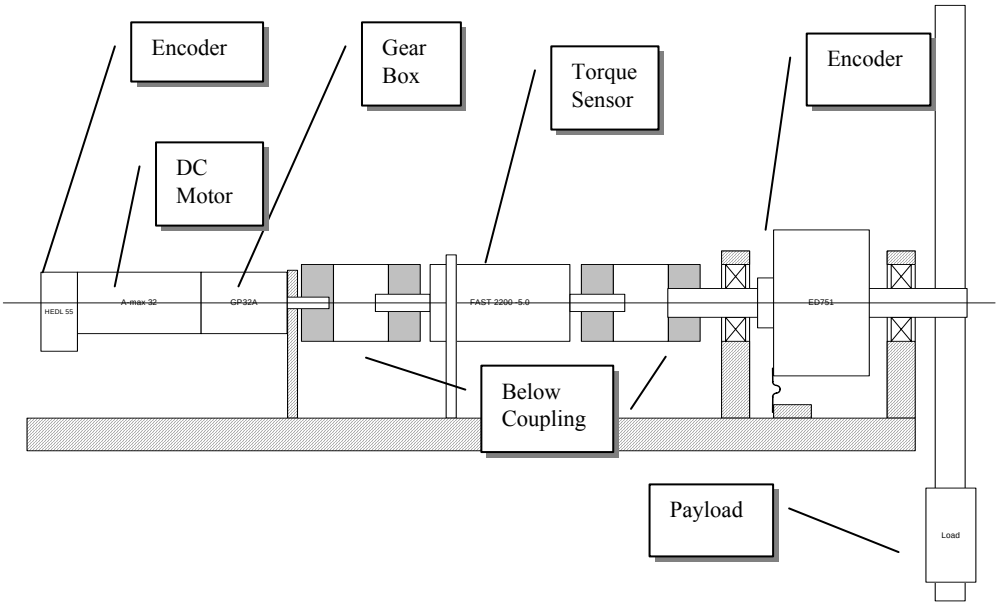

Figure 5.1-1: Drawing of the 1-DOF functional mechanical model

The mechanical component details are given one by one from left to right according to the Figure 5.1-1. The digital incremental motor encoder connected directly to the rotor is capable of measuring 500 counts per rotation. The 15W *permanent magnet DC motor* with graphite brushes drives the link over three layer planetary gearbox with 1 degree backlash. Two below couplings are used to prevent the misalignments of the shafts. The analog torque sensor is capable of measuring the nominal torque within the range of ±5 Nm. 4096 count per revolution digital incremental encoder is used to measure the orientation of the link. Since the link encoder is incremental, it is necessary to initiate an action to find the index of the encoder. After finding the index rotation the direction of the gravity vector can be calculated from the absolute position of the encoder. Gravity vector is used to calculate arithmetically the gravitational torque of the payload observed by the torque sensor. The payload weighs comparable that the other links of the robot are fixed to and orientation. By sliding the payload over the arm will demonstrate the different static kinematic configurations of the robot.

5.2. Setup Electronics

The setup can be classified as SIMO (single input multiple output) system. Motor current from the linear power amplifier is the only control input and the rotor rotation, link orientation, and the shaft torque is the three outputs of the system.

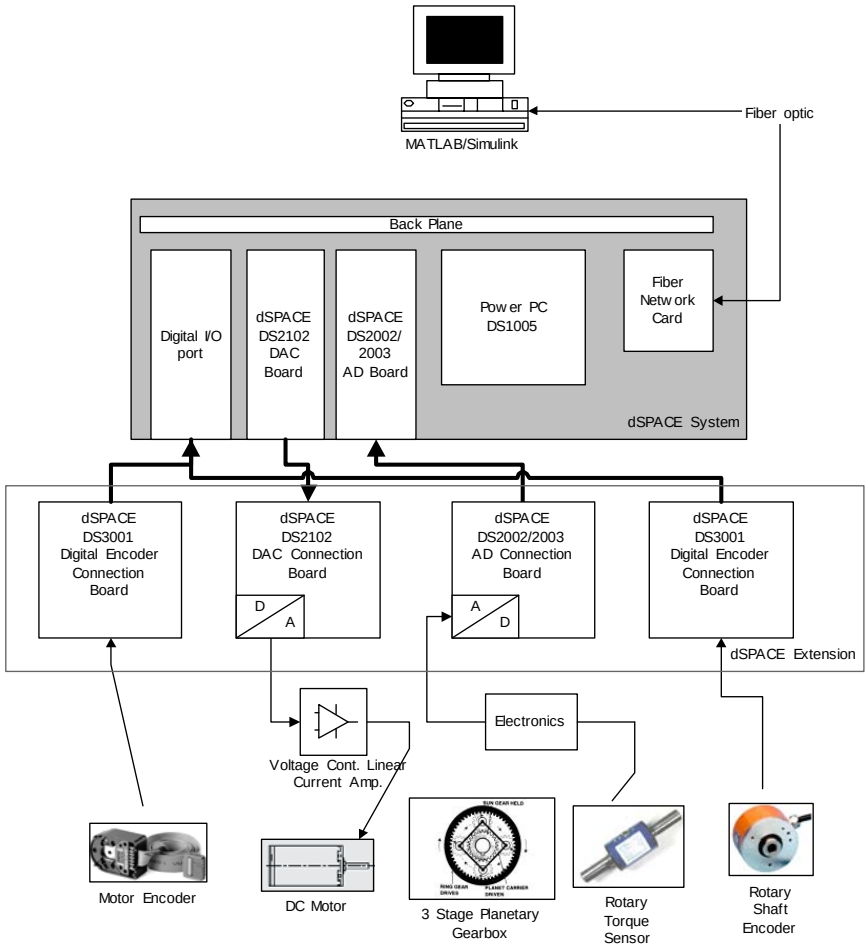

Figure 5.2-1: Electronic Schematics of the setup

In the above figure the electronic connection of the overall test setup is given. The controller is designed on a fast 64-bit PC in MATLAB Simulink environment. The designed

controller can directly be downloaded via fiber optic cable into the *real-time* dSPACE DS1005 board from the Simulink environment.

The heart of the *real-time* environment DS1005 PowerPC board is a processor board, which provides the basis of the dSPACE modular system. It gives the real-time calculation power to the modular system, but also provides the interface to the I/O boards and to the host PC. (dSPACE, 2003) The dSPACE modular system has an extension board includes the I/O connectors. The electronic connections between the 1-DOF actuators and sensors and the dSPACE system are accomplished via this extension board.

The *power amplifier* operates in the current mode and drives the 24V DC motor. The amplifier is controlled with one of the D/A channels of the dSPACE system. It can be deduced that the amplifier converts the dSPACE voltage value into motor current. Linearity of the conversion is guaranteed by the specification of the *power amplifier*. The amplifier is powered by 24 V 2.5A regulated power supply. This power supply is the main source of the power distribution to the setup.

The dSPACE extension board is capable of direct connection of the *digital encoders* in this case the motor and the rotary shaft encoder. The *rotary torque sensor* however needs extra electronics for power since it requires a supply voltage is between 9-12 V it cannot be fed through the power supply of the power amplifier which operates with 24V.

The analog voltage output of the torque sensor is connected to the A/D converter of the dSPACE system. 1 KHz bandwidth of the torque sensor that is supplied in data sheet limits the torque frequency spectrum of the torque measurement. For the experiments 1 ms *step size*, which corresponds to 1 KHz step frequency is used. As it is necessary to use at least 2 KHz *sampling frequency* according to the Nyquist rate, the necessity of using anti-aliasing filter emerges. This problem, however, is solved using simple digital processing techniques, called *downsampling*. The *sampling frequency* of the A/D converter is set above 2 KHz and the output is down-sampled to 1 KHz that is step frequency. Another experiment is achieved to see the noise frequency spectrum of the torque measurement. The noise of the sensor is sampled with 10 Khz for 10 secs. The standard deviation of the sampled data gives the averaged noise. From this experiment SNR of the torque sensor with its electronics is found as 42 dB, which is quite high and for this reason noise of the sensor can be neglected. The power spectrum of the torque sensor from the experiment can be seen in the figure below.

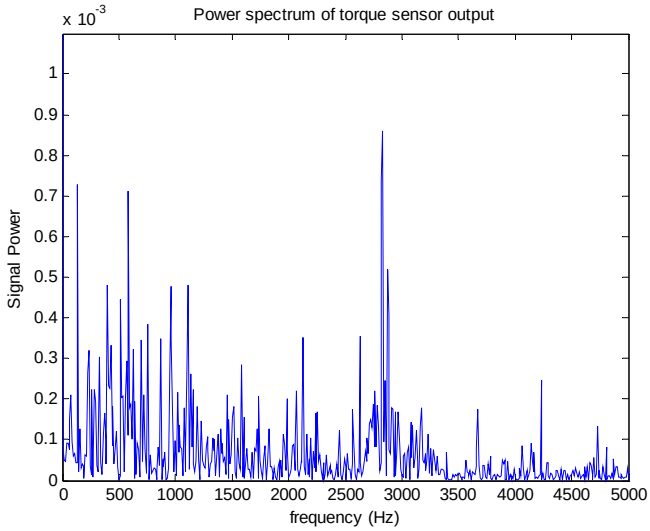

Figure 5.2-2: Noise measurement of the torque sensor

Chapter 6

Identification of The 1-DOF Setup

This part shows various system parameter identification steps different for every element of the system. Some of the critical parameters are experimentally identified and some of them are validated from the datasheet values. After this part of the report parameters are embedded into a competent model of the 1-DOF setup and the experiments are made based on this model.

6.1. Permanent Magnet DC Motor

The *permanent magnet DC motor* parameters that are necessary for the dynamic model are supplied from the manufacturer. Nevertheless, validation of some of the important parameters is necessary.

One of those is the *motor torque constant* K_t. We can identify the torque constant K_t when the rotor is stalled with measuring the blocked-rotor torque τ_{m_0} and the motor current i_m. The relationship in between is given as

$$K_t = \frac{\tau_{m_0}}{i_m} \tag{6.1}$$

The torque sensor in most of the robotic systems, however, is placed near the link side just like our 1-DOF setup. For this case, the gearbox ratio n_{gb} should also be included. Now the equation has this additional term

$$\tau_s = n_{gb} \cdot \tau_{m_0} \tag{6.2}$$

where τ_s represents the measured torque. Combining the two equations K_t yields

$$K_t = \frac{\tau_s}{n_{gb} \cdot i_m} \tag{6.3}$$

From the experiments, τ_s and i_m are measured as 1.23 Nm and 0.25 A, respectively. The torque constant is found as 0.04 Nm/A using the equation (6.3). This is very close to the value to the value given in datasheet that is 0.0382 Nm/A.

The datasheet values of the other motor parameters *terminal resistance* R_a and *terminal inductance* L_a are used for dynamic model of the motor. The brush friction is identified in friction part of chapter 3 and the inertia of the rotor is discussed next.

You would find the summary of the parameters discussed in this part in **Error! Reference source not found.** below.

Parameter	Physical Property	Model Validation
K_t	Motor torque constant	0.0382 Nm/A
R_a	Motor terminal resistance	7.13 Ohm
L_a	Motor terminal inductance	1.05 mH

Table 6.1-1: Validated model parameters

6.2. Inertias

6.2.1. Shaft and Link

The link inertia and the payload attached contribute most to the overall inertia of the link side. For this reason the inertias of shaft, torque sensor shaft, below couplings are neglected.

In order to find the inertias of link and the load some measurements are made. These measurements are tabulated in Table 6.2-1.

Parameter	Physical Property	Measured Value
m_l	Mass of the arm	0.51 kg
l_l	Arm length	0.430 m
m_{ld}	Load mass	0.87 kg
l_{ld}	Load moment dist.	0.145 m

Table 6.2-1: Measured parameters of the inertial elements

The inertia of the link can be found using the following formula

$$J_l = \frac{1}{3} m_l l_l^2 \tag{6.4}$$

where m_l is the mass of the arm and l_l is the length of the arm that carries the payload shown in the Figure 5.1-1. Using above formula the inertia of the link J_l is found as $3.14\text{x}10^{-2}$ kgm^2 with the related measurements.

Calculation of the inertia of the load J_{ld} can be done using

$$J_{ld} = m_{ld} r_{ld}^2 \tag{6.5}$$

Here m_{ld} stands for the mass of the link and r_{ld} is the distance of the *center of mass* (COM) of the load from the rotation axis. This formula yields that the inertia J_{ld} is $1.83\text{x}10^{-2}$ kgm^2

The overall inertia of the link side then makes

$$J_{l+ld} = 4.97 \times 10^{-2} kgm^2 \tag{6.6}$$

6.2.2. Motor Side

The manufacturer luckily has already supplied motor inertia and the gearbox inertia. These values are taken as granted without making an identification.

Parameter	Physical Property	Supplied Value
J_m	rotor inertia	$4.19\text{x}10^{-6}$ kgm^2
J_{gb}	Gearbox inertia	$0.7\text{x}10^{-7}$ kgm^2

The overall inertia from the motor side

$$J_m + J_{gb} = 4.19\times10^{-6} + 0.07\times10^{-6} = 4.26\times10^{-6}\,kgm^2$$

The translated inertia J'_{m+gb} to the link side via *gear ratio* n can be calculated as follows

$$J'_{m+gb} = \frac{J_{m+gb}}{n^2} \tag{6.7}$$

$$J'_{m+gb} = \frac{4.26\times10^{-6}}{\left(\frac{1}{123}\right)^2} = 6.45\times10^{-2}\,kgm^2 \tag{6.8}$$

As a conclusion it is found out that the translated inertia of the motor side is comparable to the overall link side inertia. This implies that a minimum 4th order equation should be used to model the 1-DOF setup as we have at least 1 degree backlash between two inertias. Besides, we will see next that the flexibility of the gear teeth and the torque sensor cannot be neglected.

6.3. Gearbox and Torque Sensor Compliance

The experiments show that the mechanics of the setup is flexible. This flexibility is observed when the payload in 90 degrees position under position control, even the motor encoder shows no rotor motion under applied torque on the arm the shaft encoder indicates slight rotation. This behavior should be identified for the model to study later the stability of the controller implemented.

The identification of the compliance parameters of the link side is quite simple. After the payload is set to 90 degrees as shown in the Figure 6.3-1 force impulse is applied on the load by tapping slightly by finger not to excite the backlash in the gearbox. When the payload is 90 degrees since the gears are engaged and the gear compliance will be observed besides shaft and torque sensor compliances.

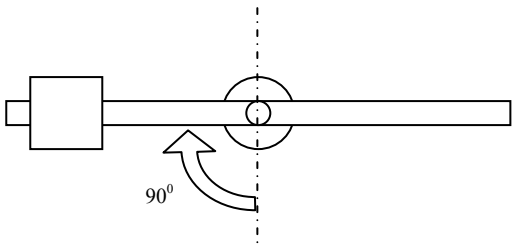

Figure 6.3-1: Payload position for impulse test

For the experiment analog torque sensor output data is collected instead of 4096-count/rev resolution shaft encoder output. The reason is the resolution of the shaft encoder is not good enough to measure small displacements to characterise the response. The offset in the torque measurement due to the gravity effect of the hanging mass was subtracted from the response.

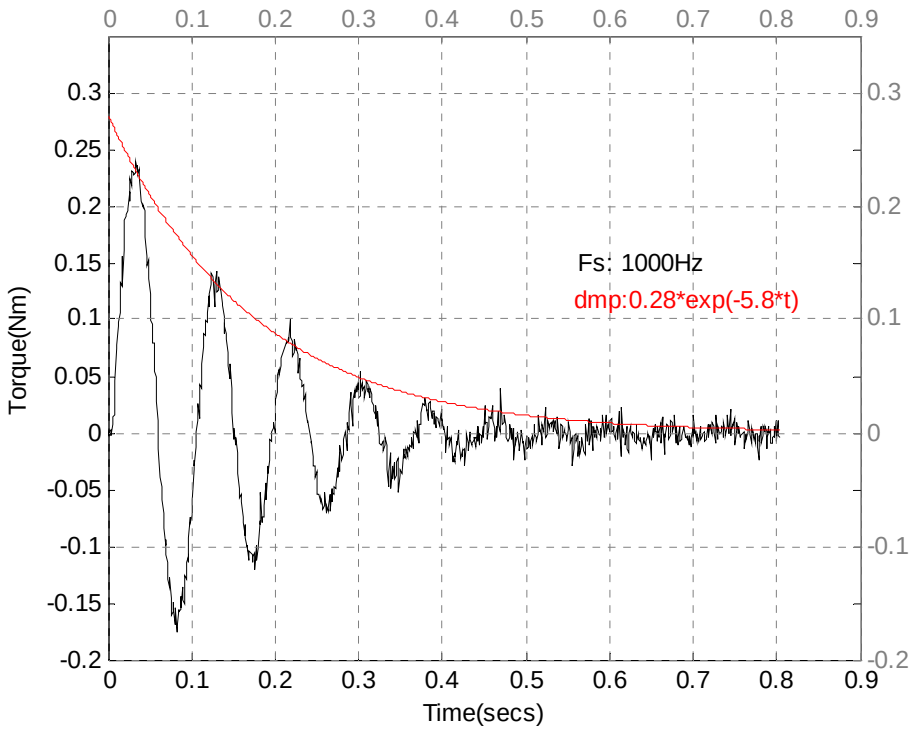

Figure 6.3-2: Transient impulse response of the system

Expected under-damped second order behaviour is observed as shown in the Figure 6.3-2. From this figure we only need to extract the oscillation frequency and the attenuation factor of the response, which are closely related with the overall stiffness and the link side damping parameters of the system, respectively. Overall stiffness includes the stiffness of the gearbox, torque sensor and the shaft. The rotational stiffness of the below couplings is very large compared with the rotational stiffness of shaft from the specs. (9050 Nm/rad >> 240 Nm/rad) The stiffness of the shaft is derived later in this section. The link side damping is due to the friction of the bearings of the shaft shown in Figure 5.1-1. The damping of the motor elements is not considered because it is observed that the rotor doesn't rotate during the experiment.

In order to find the linear dynamic relation of this compliant behaviour if the gravity force is subtracted from the plot the general differential equation can be written in this form.

$$C(s) = \frac{\omega_n^2}{s^2 + 2\zeta\omega_n s + \omega_n^2} \tag{6.9}$$

where ζ is the damping factor, ω_n is the natural frequency. The transient solution of the following generalized Laplace transfer function for under-damped condition $0 \le \zeta < 1$ is

$$c(t) = \frac{\omega_n}{\sqrt{1-\zeta^2}} e^{-\zeta\omega_n t} \sin \omega_n \sqrt{1-\zeta^2}\, t \tag{6.10}$$

When the experimental data is manually fitted to the above solution

$$\begin{aligned} \zeta\omega_n &= 5.8 \\ \omega_n\sqrt{1-\zeta^2} &= 2\pi 11 \end{aligned} \tag{6.11}$$

this equations leads to

$$\begin{aligned} \omega_n &= 69.37 rad/s \\ &= 11.04 Hz \\ \zeta &= 8.6 \times 10^{-2} \end{aligned} \tag{6.12}$$

The amplitude of the impulse input is 1 unit. The tapping gives an impulse that the amplitude cannot be calculated. For this reason the amplitude of the response doesn't fit to the curve. Fitted curve is shown in Figure 6.3-3

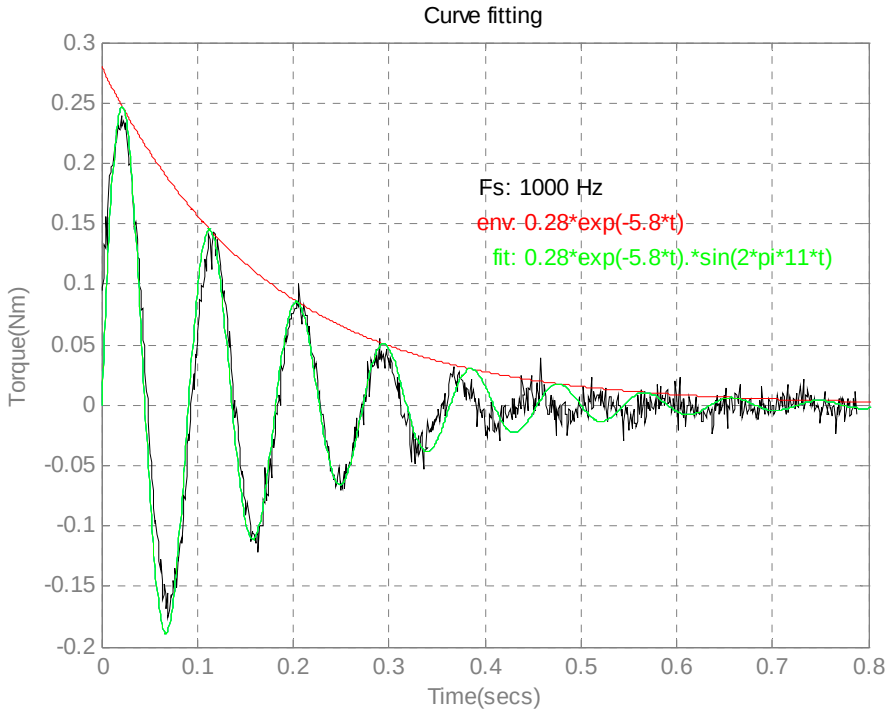

Figure 6.3-3: Curve fit

First part of the curve fits pretty well to the experimental data, however, in the middle part the non-linearity is observed and this gives a phase shift to rest of the response. This non-linearity is believed to be the result of from the rolling friction of the engaged gears and stiction of the bearings.

The natural frequency ω_n and the damping factor ζ are related to the overall inertia of link side J_{l+ld}, rotational stiffness between gearbox and the arm c_l, and rotational damping b_l

$$\begin{aligned} \omega_n &= \sqrt{\frac{c_l}{J_{l+ld}}} \\ \zeta &= \frac{b_l}{2\sqrt{J_{l+ld} c_l}} \end{aligned} \tag{6.13}$$

If we solve the first equation for c_l, we get

$$\begin{aligned} c_l &= \omega_n^2 J_{l+ld} \\ &= (69.37 rad/s)^2 (4.97 \times 10^{-2} kgm^2) \\ &= 239.17 Nm/rad \end{aligned} \tag{6.14}$$

and when we solve it for b_l

$$
\begin{aligned}
b_l &= 2\zeta\sqrt{J_{l+ld}c_l} \\
&= 2(8.6\times10^{-2})(\sqrt{(4.97\times10^{-2}\,kgm^2)(239.17\,Nm/rad)}) \\
&= 0.59\,kgm^2/rads
\end{aligned}
\tag{6.15}
$$

6.4. Backlash

The value of the backlash is supplied in the datasheet of the gearbox vendor. The value is given as 1 degree, which is quite high for a precision operation. Since the application doesn't require high precision and the user in the manipulator control loop will correct the tracking errors this is reasonable for collocated control. The impact of this backlash will be on the stability of the arm and decision of the control strategies applicable to our situation. Generally speaking, the use of the inner position controller is highly limited due to 1 degree backlash.

6.5. Friction

6.5.1. Dry Friction

The necessity of modeling friction comes from the experimental results of (An, C.H., Atkeson, C.G., Hollerbach J.M., 1988). They mention that when gearbox transmission is used instead of direct drive system to drive the link of the robot 50 % of the torque of the motor is reduced due to the friction. Especially, the influence of the *stiction* must be compensated to increase the *end-effector* positioning precision and tracking performance for the link close to the base of the robotics manipulator with the fact that when the *end-effector* is away from the base the translation of the link rotation error significant in *end-effector* coordinates.

The amount of the dc motor friction Fs_{mot} that motor brushes mostly contribute to the link side is considerably high. Moreover, the sliding gear friction Fs_{gb} of the gearbox on load shouldn't be neglected on higher loads since it's contribute is a function of the payload.

Obviously, The DC motor brushes add more friction than the motor bearings. For this reason Fs_{mot} can be assumed as *dry friction*. The *dry friction* consists of static, *Stribeck*, and *Coulomb* frictions.

In the literature there are several dynamic friction models. Karnopp, Leine, Dahl, and LuGre are some of the well-known ones. For the model of the friction LuGre model is used and an identification experiment is made.

6.5.2. Experiments

The setup is very complicated because of the backlash in the system. There should be a better way to identify the friction that it shouldn't activate the other states of the systems such as gear collision due to the backlash and compliance of the gearbox. The solution is very simple. Since we have two inputs from the torque sensor and the motor encoder these inputs can be used to measure the friction torque $\tau_{friction}$. If we assume that the motor torque constant is giving the precise value of motor torque τ_m related with the input current we can take the difference between measured torque τ_{meas} and the motor torque τ_m. The difference will give the friction torque $\tau_{friction}$ which will be the y-axis of the friction-velocity plot. On the x-axis there will be the velocity of the rotor. The velocity can be found with numerically differentiating the motor encoder value. This will give a precise observation if it is passed through a low pass filter to remove the discrete effect of the digital output. Another important assumption is that during the experiment the backlash shouldn't be activated. This can be

achieved using a small slope velocity profile. This small slew rate will also guarantee that the phase lag due to the low pass filtered velocity can be ignored.

The experiments show that the friction with low speeds has the following characteristics shown in the Figure 6.5-1. The friction of the system is modeled with LuGre (Lund-Grenoble) model (De Wit, C. C., Olsson, H., Astrom, K. J., Lischinsky, P., 1995) as stated before. The model is given below

$$\frac{dz}{dt} = \omega - \frac{\lambda_0 |\omega|}{g(\omega)} z \tag{6.16}$$

$$g(\omega) = \alpha_0 + \alpha_1 e^{(-(\frac{\omega}{v_{sk}})^2)} \tag{6.17}$$

$$\tau_{friction} = \lambda_0 z + \lambda_1 \frac{dz}{dt} + \alpha_2 \omega \tag{6.18}$$

In this 6 parameter friction model α_0 is *Coulomb* friction, α_1 is *Stribeck* friction, α_2 is viscous friction, λ_0 is bristles stiffness, λ_1 is bristles damping, and v_{sk} is *Stribeck* velocity coefficients. The static coefficients are estimated with MATLAB non-linear least square optimization method. The dynamic coefficients are more difficult to be identified because the internal state z is not observable. For this reason the dynamic parameters are estimated by trial and error. According to the estimated values a simulation is made and compared with the experimental data. You will find two plots for short and the long ranges of the rotational velocity.

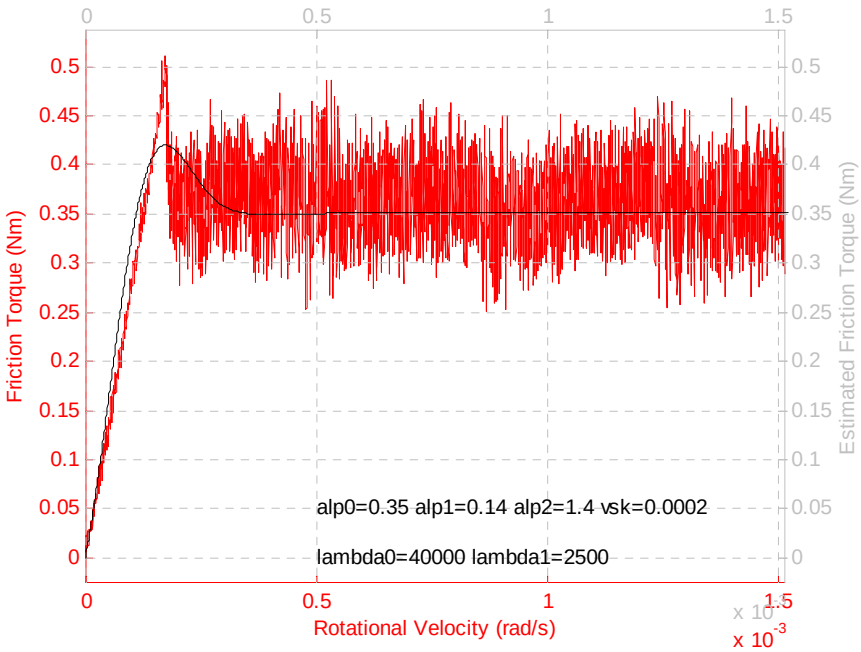

Figure 6.5-1: Experimental friction and fitted LuGre Model near zero velocities

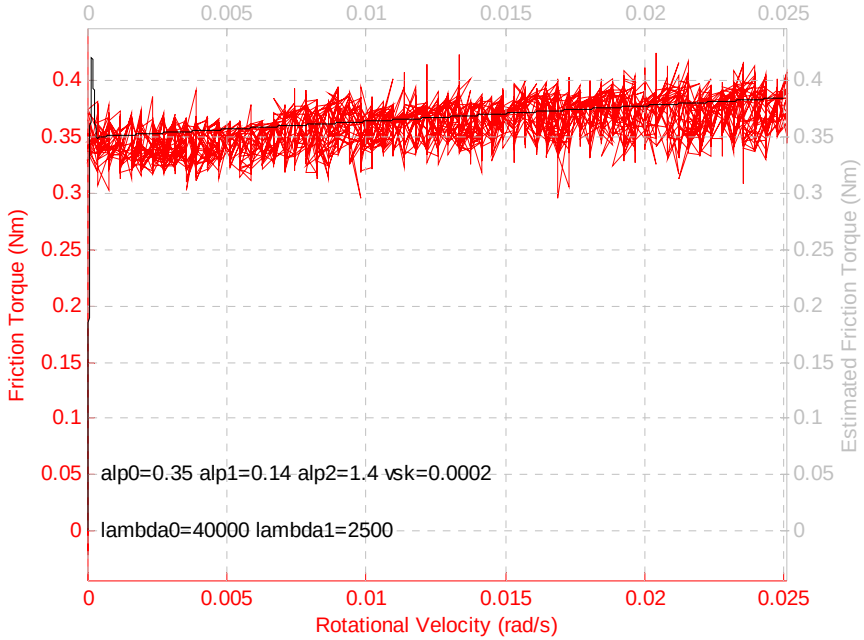

Figure 6.5-2: Experimental friction and fitted LuGre Model in long range of positive velocities

Parameter	Physical Property	Estimated Parameter
α_0	*Coulomb* friction	0.35 Nm
α_1	*Stribeck* friction	0.14 Nm
α_2	viscous friction	1.4 Nms/rad
λ_0	bristles stiffness	0.4×10^6 Nm/rad
λ_1	bristles damping	2.5×10^3 Nms/rad
v_{sk}	*Stribeck* velocity	0.2×10^{-3} rad/s

Table 6.5-1: Identified friction parameters

6.5.3. Normal Force Influence

In addition to the motor brush friction gearbox also introduce considerable amount of friction to the system dynamics. From a magnified point of view when we consider the gear tooth engagement of two spur gears in the planetary gearbox during the drive of the motor, it can be realized that the friction is a function of the payload.

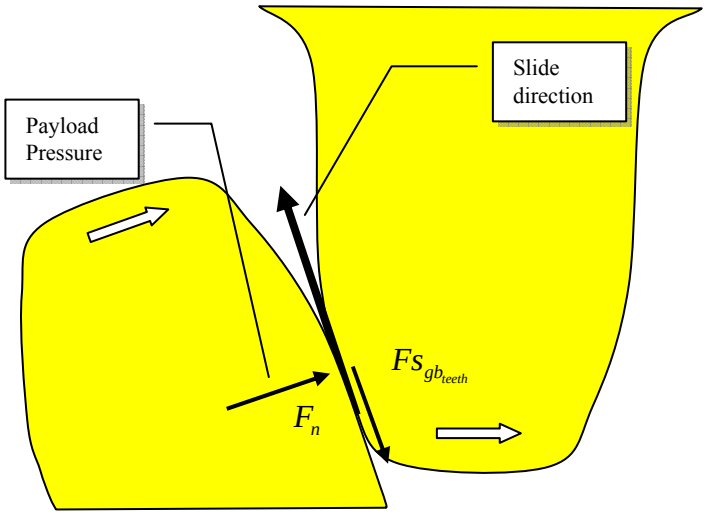

Figure 6.5-3: Engaged gear friction drawing

6.5.4. Experiments

The overall stiction caused by the motor and the gearbox is estimated by observing the torque sensor for the instant motor motion while the torque applied to the arm is increased manually. As we claim that the friction is a function of payload pressure on the engaged teeth it should also depend on the payload.

6.6. Discussion

As conclusion, experimental results show that the gearbox and torque sensor at each joint is considerably elastic. The 1-DOF setup, therefore, can be classified as elastic joint robotic manipulator. For the design of each link of the MANUS robot this result should be considered because this will affect the stability of the total manipulator. The friction of the setup due to the motor brushes is vital to be compensated for a better control of the link torque and link rotation with a feed-forward controller. The necessity will be realized in case of implementation of an impedance controller.

Another problem that will affect the stability of the manipulator is the 1-degree backlash. There are backlash compensators if the translated resolution of the motor encoder is comparable with the resolution of the shaft encoder which means that it's better to use 15 times higher resolution shaft encoder.

The collection of the values will be used in the model can be found in Appendix.

Chapter 7

Dynamical Model of the 1-DOF Setup

This chapter is intended for construction of the competent lumped dynamic model of the system. Every part in the control loop is modeled using a suitable method in 20-sim®[1] and these parts are introduced throughout this chapter. Parts are then combined and simulated. Finally, The simulation results are compared with the experimental results.

7.1. System Categorization

The mechanical drawing in the Figure 7.1-1 (Spong, M., 1987) is employed to illustrate the design steps based on the findings of experimental model identification. The drawing shows 4th order system including two masses with flexible connection. The gravity force introduces the non-linearity to the system with the backlash in the gearbox. The gravity force will not be included in the model for the ease of benchmarking however it can simply be added into the model.

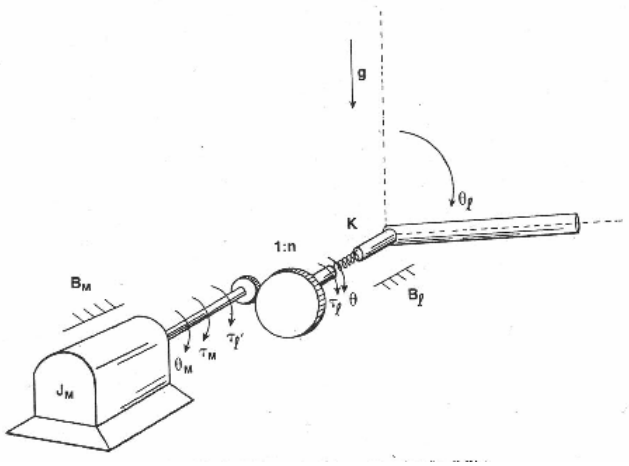

Figure 7.1-1: 1-DOF flexible joint manipulator

Some of the parameters for the dynamic model the 1-DOF setup can be found in the appendix. These parameters in combination with the identified parameters are inserted into the lumped models. These models now will be introduced one by one.

[1] 20-sim is the software of Controllab Products B.V. http://www.20sim.com/

7.2. Power Amplifier

The amplifier is running in current mode. From the datasheet of the device it is mentioned that PI controller controls the current with linear power stage. It is assumed that integral action is very fast to recover the steady-state error. The voltage limiter in the design guarantees that the motor voltage is in range of ±24 Volts. The current is measured from the terminal and feedback to the controller. The model diagram is given below.

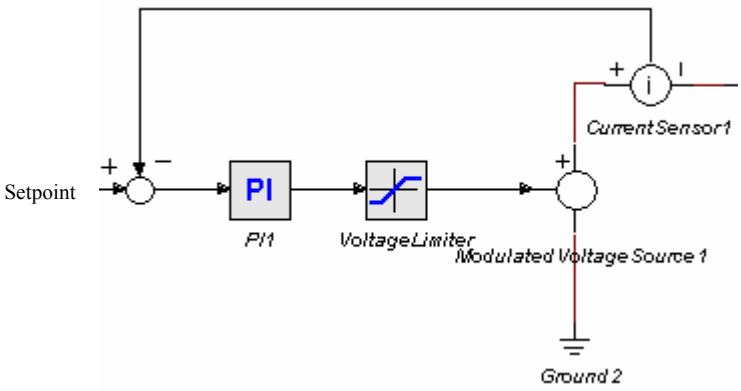

Figure 7.2-1: Amplifier model

7.3. DC motor & Gearbox Model

The standard model for the DC motor is used. The parameters *armature resistance* R_a, *armature inductance* L_a, and the *motor torque constant* K_t have already been supplied in product datasheet. Nevertheless these parameters are also been identified in the previous section. The friction of the brushes is modeled with Lu-Gre friction model since the stiction is very visible in torque measurements.

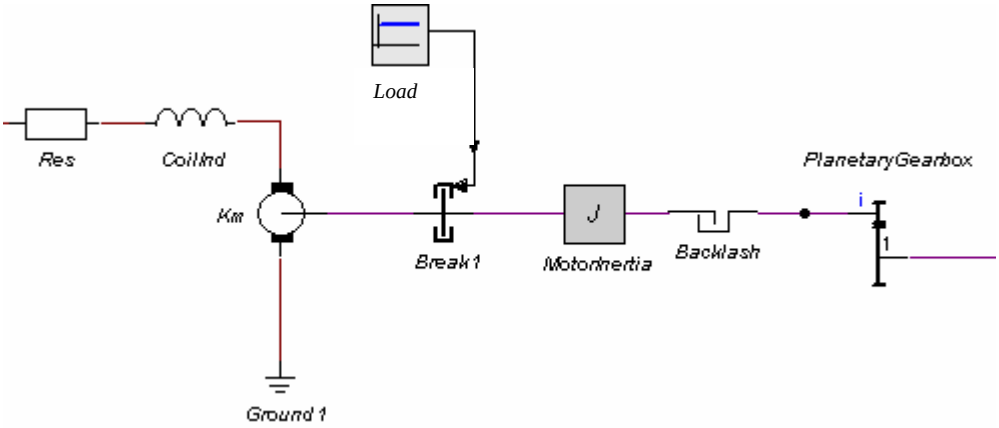

Figure 7.3-1: DC Motor model

7.4. Shaft & The Load Model

Since the shaft is flexible it is modeled by a linear spring. The resonance frequency is around 11 Hz and the damping is modeled as linear because the effect of the stiction and the static friction is very less in the bearings.

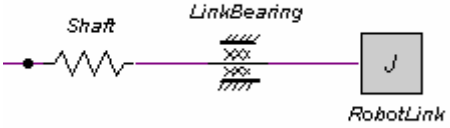

Figure 7.4-1: Link model

7.5. Model Complexity

Due to the backlash and Lu-Gre friction models the simulation only runs using backward differentiation methods. The model contains:

- 32 variables
- 9 independent states

The simulation speed is quite fast for the utilized differentiation techniques.

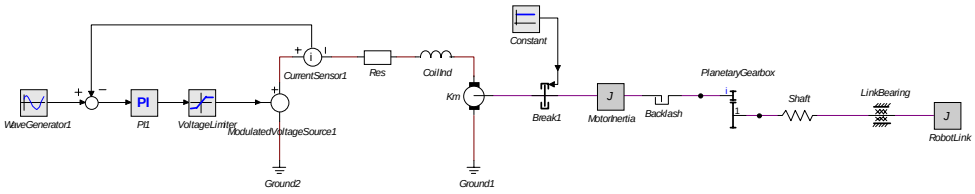

Figure 7.5-1: 20-sim dynamic model of 1-DOF setup

7.6. Simulation

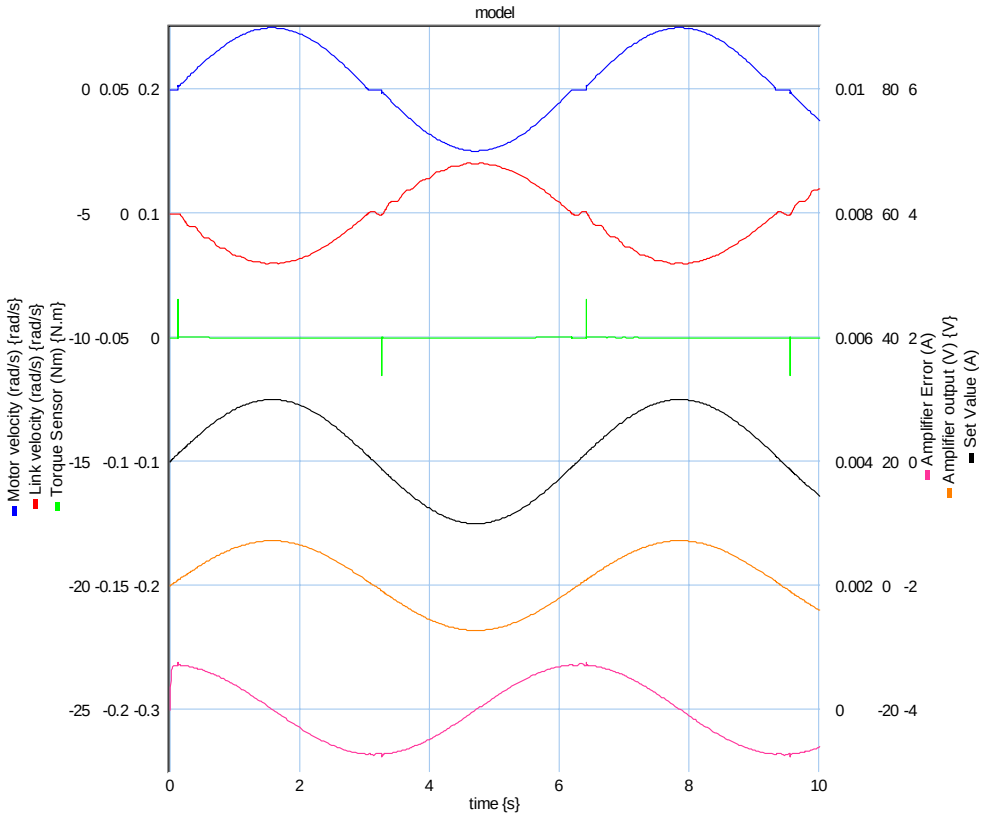

Figure 7.6-1: 20-sim simulation results

From this simulation we observed the stiction when the motor velocity indicated with the blue line is close to the zero point. The flexibility of the shaft is observed with ripples on the red trace, which is the shaft velocity. The backlash is obvious from the peaks of the torque measurement, which is shown with the green trace. The input signal is a sinusoidal wave with black trace. The orange trace shows the unsaturated armature voltage. The PI current controller minimizes the error with in $0.2 \times 10^{-2} A$. It can be seen in pink trace.

7.7. Discussion

The simulation results fit quite well to the experimental results even there are nonlinearities in the setup. The friction in the gearbox is observed that it depends on the load. The impact of the gears due to the backlash generates very high torques and makes simulation difficult using well known simulation methods such as Euler, Runge-Kutta4. The stiction due to the brushes is very hard to model because it is non-linear time variant. The flexibility of the setup is, however, simulated very well. As a conclusion, this model can be used for testing of the new control strategies.

Chapter 8

1-DOF Setup Control

We started with introducing the 1-DOF setup. Then we identified the 1-DOF setup elements and we built the dynamical model of the system. Now in here we will implement some of the important compliant control strategies on the 1-DOF setup that is previously introduced and we will compare their performance with each other based on the experimental results.

8.1. Active Stiffness Control (PD Controller with Gravity Compensation)

Stiffness control (Salisbury, J.K., 1980) derives from a position control scheme of PD type with *gravity compensation.* Let $\mathbf{q}_d$ denote the desired link rotation, the control law can be written as

$$\boldsymbol{\tau}_d = k_p(\mathbf{q}_d - \mathbf{q}) - k_d\dot{\mathbf{q}} + \mathbf{g}(\mathbf{q}) \tag{8.1}$$

where k_p is the gain of an active stiffness on the joint space, and k_d is the gain of the active joint damping. The gravity compensation is denoted with $\mathbf{g}(\mathbf{q})$. The purpose here is to make the joints compliant with respect to the contact forces. For this reason this strategy is also referred to in the literature as (active) *compliance control*. Since damping is controlled besides stiffness, the control law (8.1) can be regarded as an *impedance control*. (Chiaverini, S., Siciliano, B., Villani, L., 1999)

This controller can also be adapted for a robot manipulator. For the manipulator the compliance is desired at the end-effector coordinates. So the manipulator *Jacobian* is involved in the control law. Let p_d denote the desired end-effector position; the driving torques are chosen as

$$\boldsymbol{\tau}_d = J^T(\mathbf{q})k_p(\mathbf{p}_d - \mathbf{p}) - k_v\dot{\mathbf{q}} + \mathbf{g}(\mathbf{q}) \tag{8.2}$$

where k_p is the gain of an active stiffness on the end-effector position error, and k_v is the gain of a joint damping action. Note that the derivative of the set point in the derivative action is removed from the expression since the derivative of the steps of digital set point introduces high noise into the system.

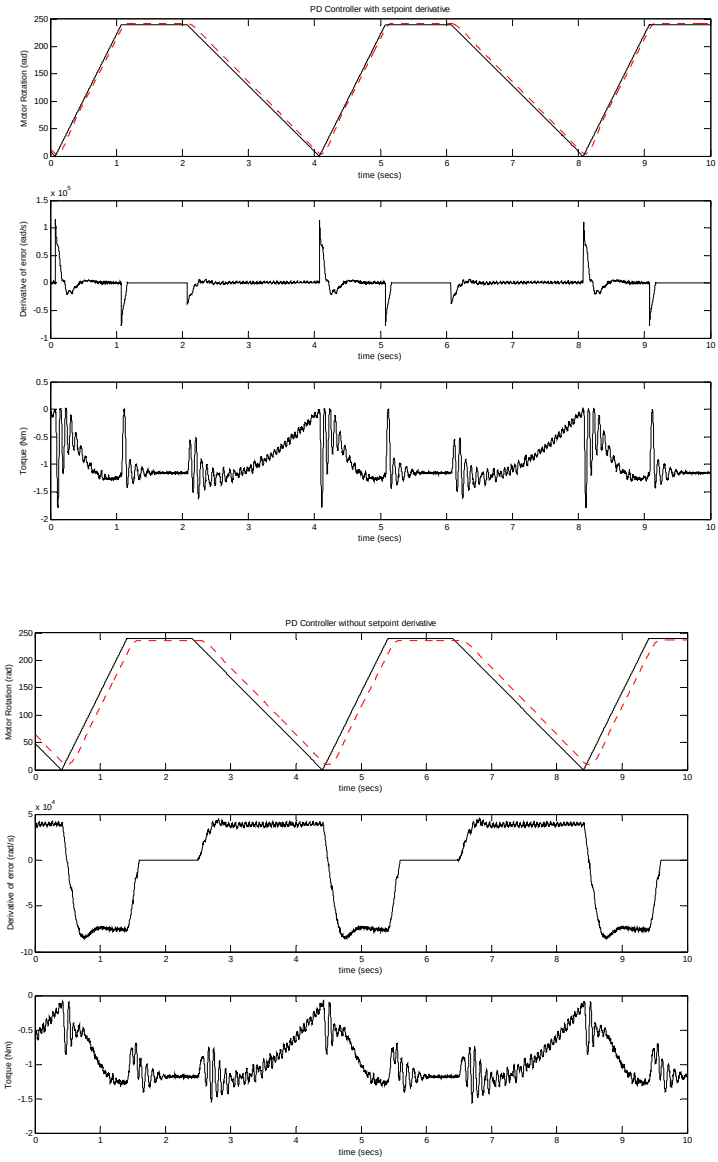

Figure 8.1-1: PD controller with (top) and without (bottom) set point derivative

The effect of including the derivative of the set point is seen in the above figure. The second row show the output of the differentiator that has sparks on the right figure due to the derivative of the error causing torque impulses seen in the third row. We may say that the derivative of the set point is good to reduce the tracking error however it introduce high torques for the abrupt changes of the motion profile.

For the experiments the derivative of the set point is included because it tests wildly the performance of the controller. Nevertheless, the derivative of set point would better left for the long-lasting operation of the manipulator.

8.1.1. Experiments

For the test of the gravity compensated active stiffness controller the repeated trapezoid trajectory is used. The reason for this is high jerks in the acceleration profile induce the vibration modes of the system and challenge the stability so we can easily see the system performance.

The motor rotation is controlled and the motor encoder rotation is fed back to the controller so we may say that this is a collocated controller. Besides, the torque sensor located on the shaft gives the measure of the compliance that is necessary for testing.

The compliance of the PD controller is tested in several steps by gradually decreasing the gain of the P action. Theoretically, when the P action of the controller is reduced it is expected the controller become more compliant. The results of the experiment are seen below.

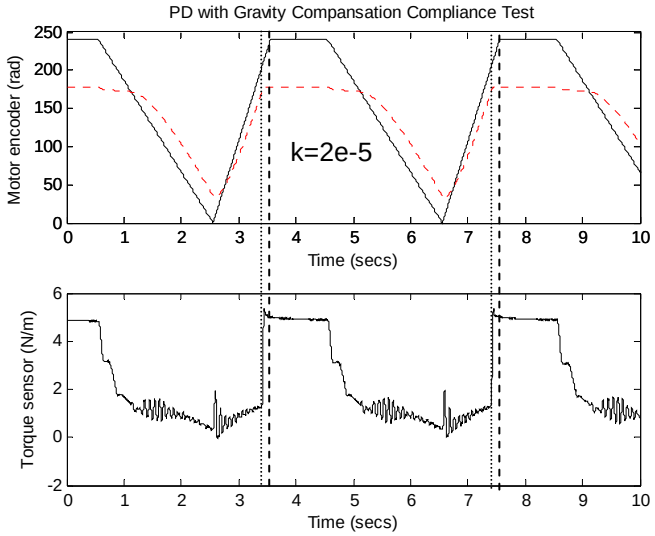

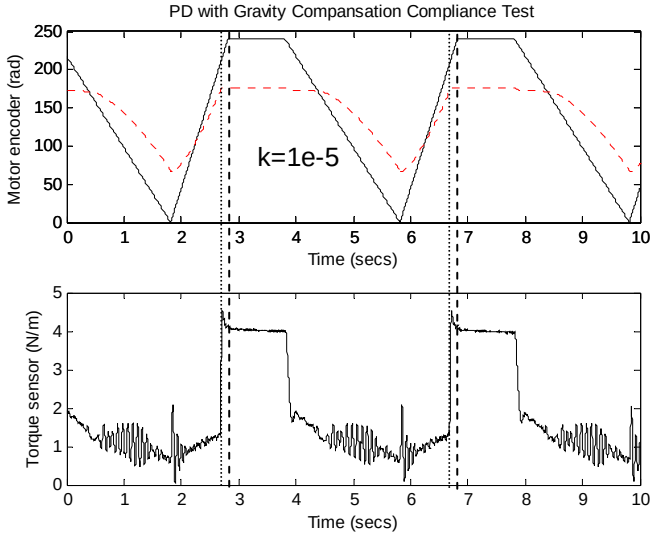

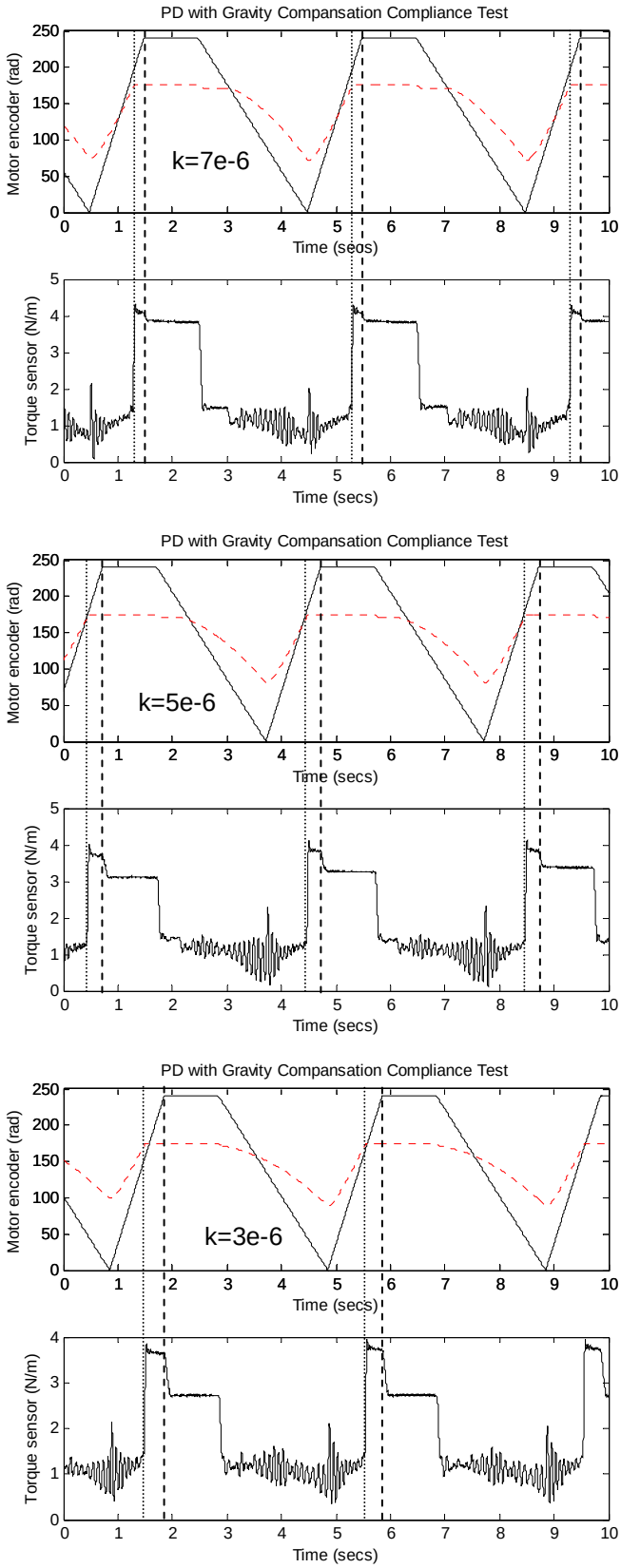

Figure 8.1-2: Compliance test by varying the P action of PD controller with gravity compensation

In the experiment the rotor is commanded to rotate between 0-240 radians and a relatively stiff object obstructs the motion at 175 radians. The rotation of the arm can be calculated by 1:123 gear ratio. The gains of the controller are set $k_p = 0.3\times10^{-5}\ldots2\times10^{-5}$ and $k_d = 8\times10^{-6}$.

Note that k_d is chosen so as to guarantee the well-damped behaviour. From one of the paired figures top superimposed graph shows the tracking performance of the controller. The solid line indicates the desired path and the dotted line shows the plant response. Besides, second row shows the torque measurement during the experiment. The compliance of test has been made in 5 steps. For each step the k_p gain of the controller is reduced to increase the compliance of the controller. The instance of collision is indicated by a vertical dotted line for convenience. The end of the derivative action of the controller is indicated with dashed line. Between the two vertical lines the controller adds the derivative of the error, however, after the dashed line since the error becomes steady the derivative action stops. This will resemble to the control law without set point derivative.

8.1.2. Summary

From this experiment the collision and the equilibrium torques are found inversely proportional with the k_p gain of the controller as expected from the theory. As a result the trade-off between compliance and the tracking performance is observed. For more compliant tasks the controller has very poor tracking performance. The only advantage of this type of controller is the torque sensor feedback is not necessary. It is also seen that for more compliant operations the only derivative of the sensors should be inside the control loop.

8.2. Parallel Position/Force Regulator

From the previous example we are not satisfied with the tracking performance of the controller. So the built-in torque sensor now put into the control loop for improvement. For this case the force/torque input is added in parallel with a PD type controller because the force control is not enough itself for tracking. In literature this type of controller is named as *parallel position/force regulator*. (Chiaverini, S., Siciliano, B., Villani, L., 1999)

The details of the controller are following. The force controller is a simple gain and the output is added with the position controller torque output. The integral action in force controller results undesired behaviour when there is an estimation error of the load weight. The arm slowly goes up or down due to this error and that's why it is not included in the force controller. The nonlinearity introduced by the hanging load (gravity effect) on the link is subtracted from the torque sensor output and filtered by a low pass filter with a small phase shift of interested low frequency region. Position controller can be chosen an appropriate one to minimize the tracking and the steady state error. The diagram of this controller can be seen in the below figure.

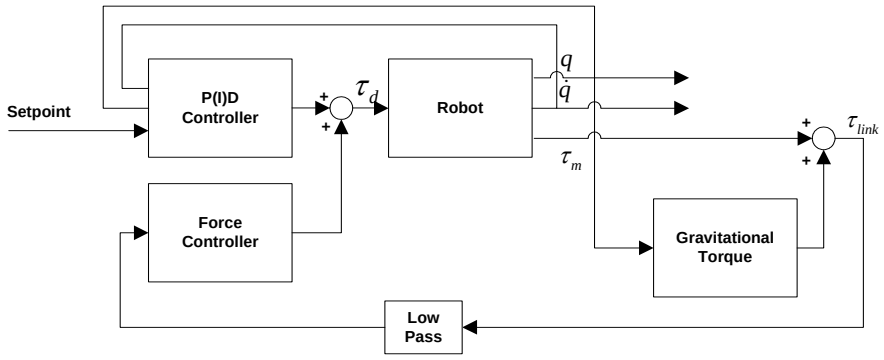

Figure 8.2-1: Direct Force Control Scheme

Just like the active stiffness controller this controller can also be used in the robotic systems. The control action again can be expressed using the manipulator *Jacobian* as

$$\boldsymbol{\tau}_d = J^T(\mathbf{q})\left(k_p(\mathbf{p}_d - \mathbf{p})\right) - k_v\dot{\mathbf{q}} + k_f H_{LP}(s)\left(\boldsymbol{\tau}_m + \mathbf{g}(\mathbf{q})\right) \tag{8.3}$$

where $\mathbf{f}$ is the filtered force feedback vector from the force/torque sensor. The desired force can also be controlled subtracting the force feedback from the desired force into the force controller.

8.2.1. Experiments

A series of experiments have been made to see the performance of the parallel position/force regulator. The force gain is increased gradually till the system is critically stable.

The task was same as before. The same periodic trapezoid motion profile is used like in the active stiffness controller test. Again the desired motor rotation is commanded and direct torque sensor measurement and motor encoder output is collected.

The plots of the experimental results are given below.

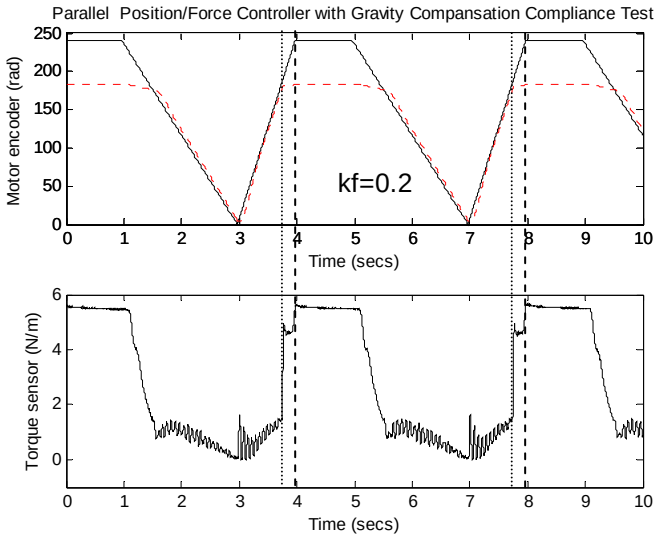

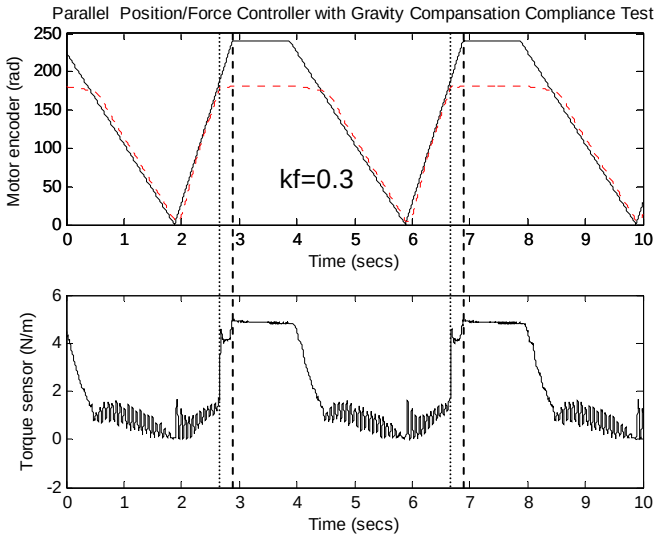

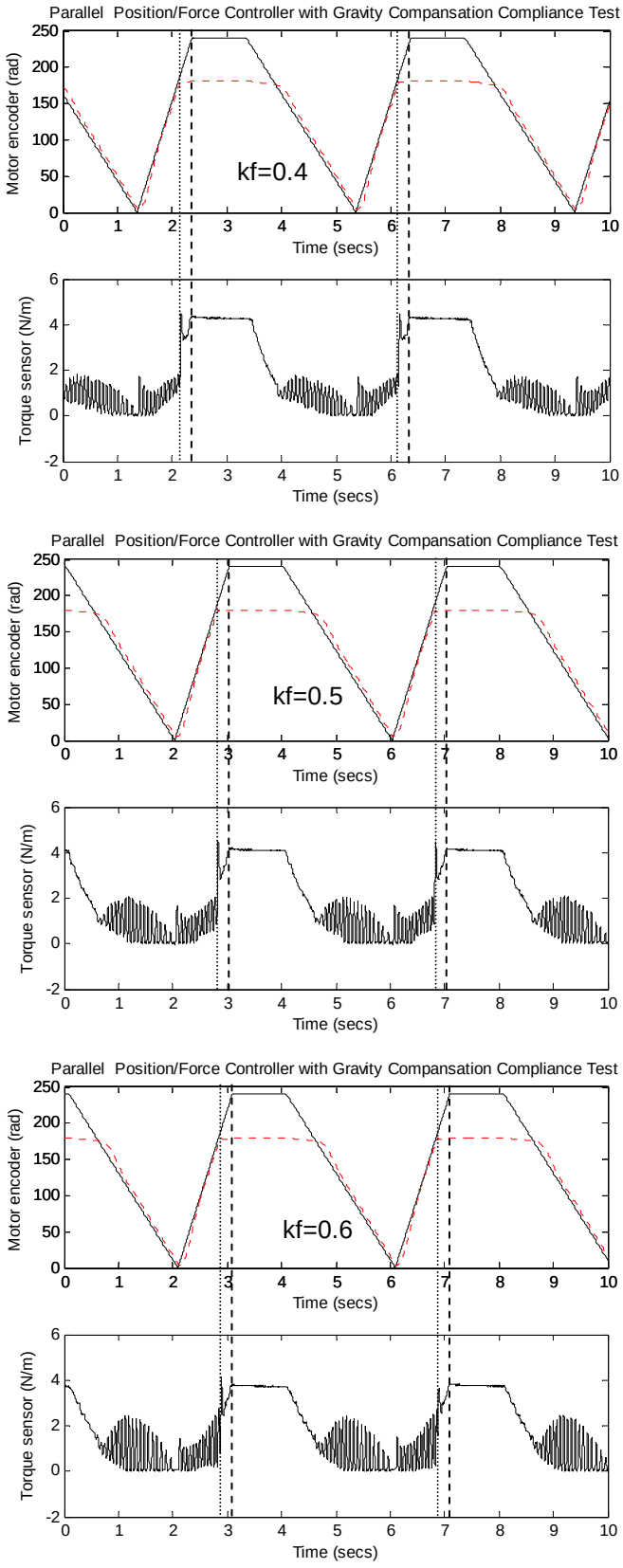

Figure 8.2-2: Compliance test by varying the force gain k_f of parallel position/force controller with gravity compensation

It is expected that the compliance of the controller will be proportional with the k_f force gain factor from the theory. The steady state contact force is seen in the figures that they

reduce with the increasing k_f factor. The impact force, however, is seen less dependent with the k_f factor. This is due to the delay of the force feedback loop in which the effect of large phase shift of the low pass filter is dominant. The high frequency part seen in the torque measurements is due the oscillation of the gears. Since the system has large backlash the gear vibration increases the measurement torque.

Note that the derivative of the set point in the PD controller doesn't affect the system performance

8.2.2. Summary

The tracking performance of this kind of controller is very good with respect to the active stiffness control. Not like in active stiffness controller the tracking performance decrease when the compliance of the controller is increased.

This controller class is robust when the transmission can be considered as rigid and when the backlash is negligible in the system. For higher k_f values the oscillations are intolerable with the systems have large play in the mechanics. Direct force control with higher force gain, however, is not suitable for mechanisms has large backlash. The gear collision observed by the torque sensor induces negative oriented torque that results the motor turn in the opposite direction and collides on the other direction. This collision results positive torque and makes the system unstable. This also means that when the backlash increases due to the gear torn for long term operations the system could be unstable. This is the bottleneck for the compliance of the controller.

When the mechanism is flexible joint the upper limit of the force controller gain also reduced because of the torque of the vibrating load hanging on the link. For this reason flexibility of the joint could be estimated and put into force control for higher force gain and more compliant stable control of the joint.

8.3. Estimator Design for External Torque Determination

It must be mentioned that the dynamic effects of the load were not included in the previous designs. The necessity of the modelling flexibility has already been discussed in the previous part. To design an *observer* to extract the external torque there made some experiments. After those experiments on the joint flexibility the transient response is linearized to a second order spring-damper behaviour. From the analysis the resonance frequency is found as 11 Hz and the damping time constant found as 0.7 seconds. The details of this analysis are given in Section 6.3. As a result the analysis shows that the estimate of the torque due to the flexible joint dynamics seen by the torque sensor is as follows

$$\hat{\tau}_{link} = J_{l+ld}\ddot{q} + b_l\dot{q} + c_l(q_m - q) \tag{8.4}$$

In this dynamic equation J_{l+ld} is the overall inertia of link side, c_l is the rotational stiffness between gearbox and the arm, and b_l is the rotational damping. q indicates the joint rotation and q_m indicates the motor rotation translated to the link side.

The estimator now put inside the system loop in following manner. The enhanced controller schema is given below.

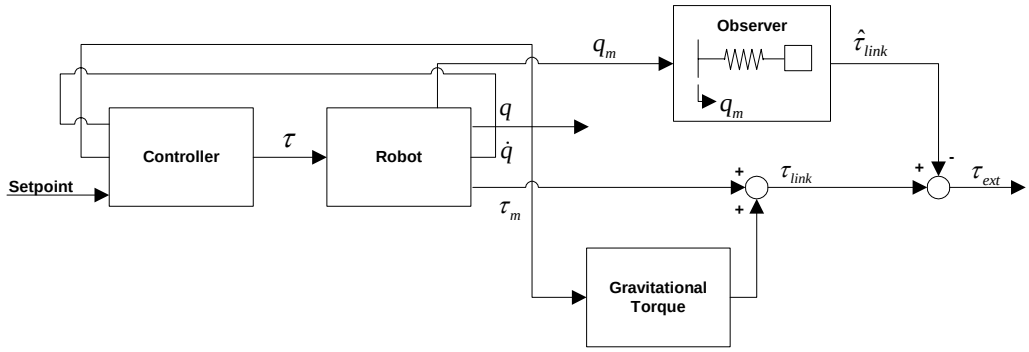

Figure 8.3-1: Estimator in the system

8.3.1. Experiments

To see the improvement of that the observer will add to the system a sinusoidal tracking experiment is performed. The torque sensor and the observer output are subtracted to get the inertial torque. From the experiment it is found that the observer output fits closely to the torque sensor output.

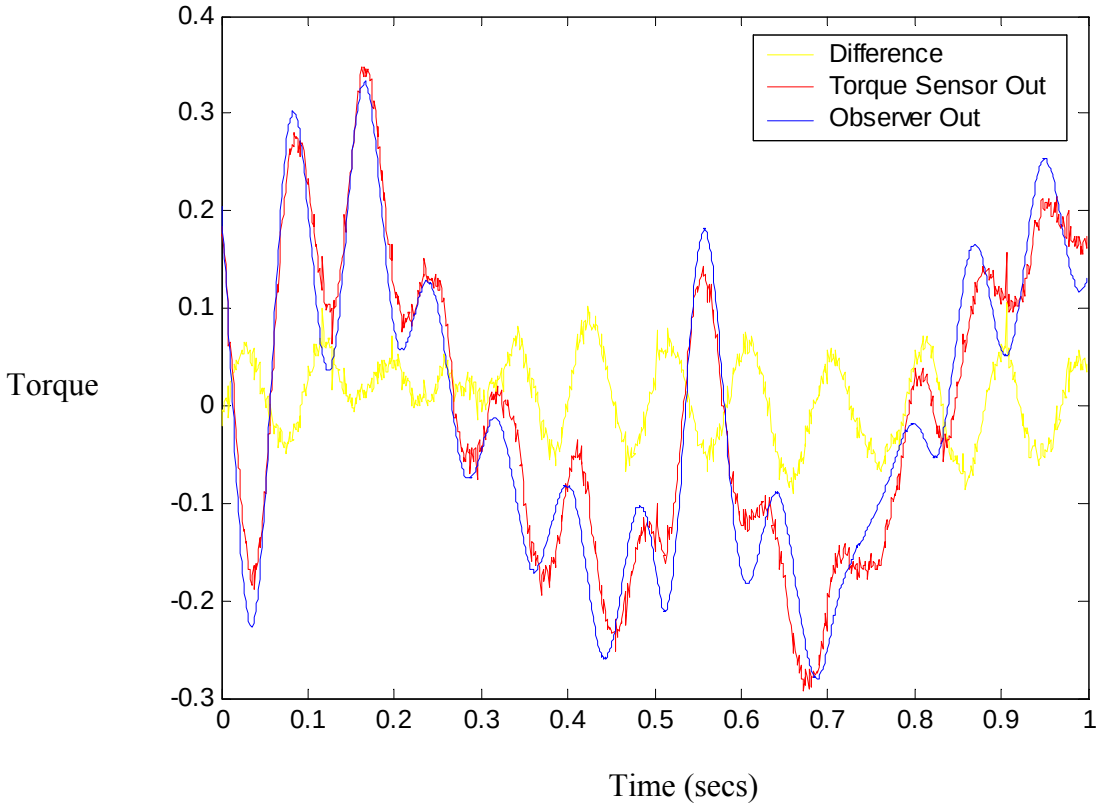

Figure 8.3-2: Trace of the observer output, the torque sensor output, and the difference

The force controller in Figure 8.3-1 is not included. If we want to include the controller the external torque output is filtered again by a low pass filter and feed into the force gain. The output will again be subtracted from the position control as shown in the Figure 8.2-1.

8.3.2. Summary

By utilizing the observer in the design the force gain can be increased more and consequently this will give the system more compliance. The disadvantage of the estimator is the estimation error. If the estimation error is too high or the phase is in phase with the vibration, this error will be amplified by the following filter/controller and make the system unstable. For the design of the controller more attention should be given.

8.4. Impedance Control with Inner Velocity Loop

Outer P type position and inner PI type velocity controller controls the MANUS. Starting from this fact the force feedback is appended in parallel manner to input of the inner velocity controller. The force controller is simply a P type controller. Since the controller relates the force and the velocity, this control can be classified as *impedance control*. (Hogan, N., 1985)

Before the force controller the gravity together with the dynamic torque estimator designed previously is subtracted from the torque measurement. The subtraction then filtered with a low pass filter for removal of the high frequency components due to the backlash and noise. The overall scheme can be observed below.

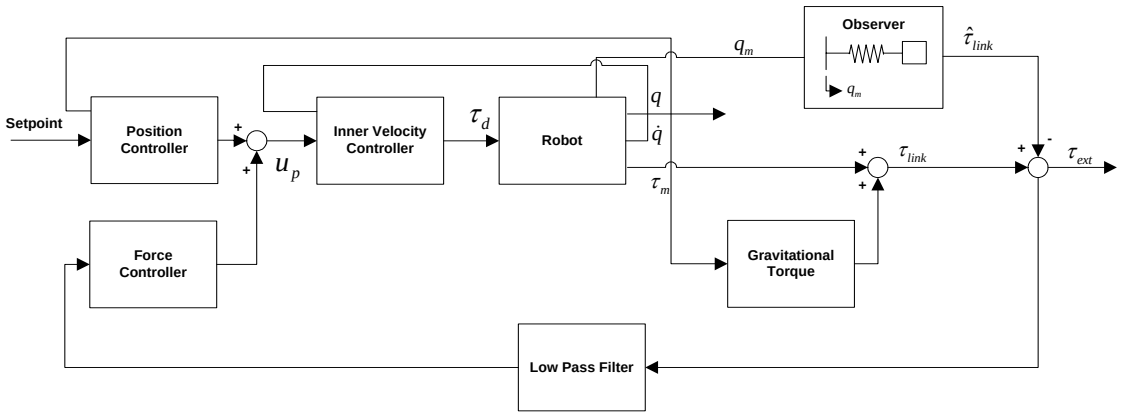

Figure 8.4-1: Impedance Control with Inner Velocity Loop

For the robotic manipulator the controller can be used in the following form

$$\begin{aligned} \mathbf{u}_p &= J^T(\mathbf{q})\left(k_p(\mathbf{p}_d - \mathbf{p})\right) + k_f H_{LP}(s)\left(\boldsymbol{\tau}_m + \mathbf{g}(\mathbf{q}) - \hat{\boldsymbol{\tau}}_{link}\right) \\ \boldsymbol{\tau}_d &= k_v\left(\mathbf{u}_p - \mathbf{q}\right) + k_i \int_0^t \left(\mathbf{u}_p - \mathbf{q}\right) dt \end{aligned} \tag{8.5}$$

8.4.1. Experiments

For the experiment again same trapezoid motion profile is used. The arm starts rotation again from vertically down configuration and turn in clockwise direction of 112 degrees. While the arm was following the trapezoid profile there is the same stiff object obstructs the path at around 100 degree. After the impact the compliance is observed.

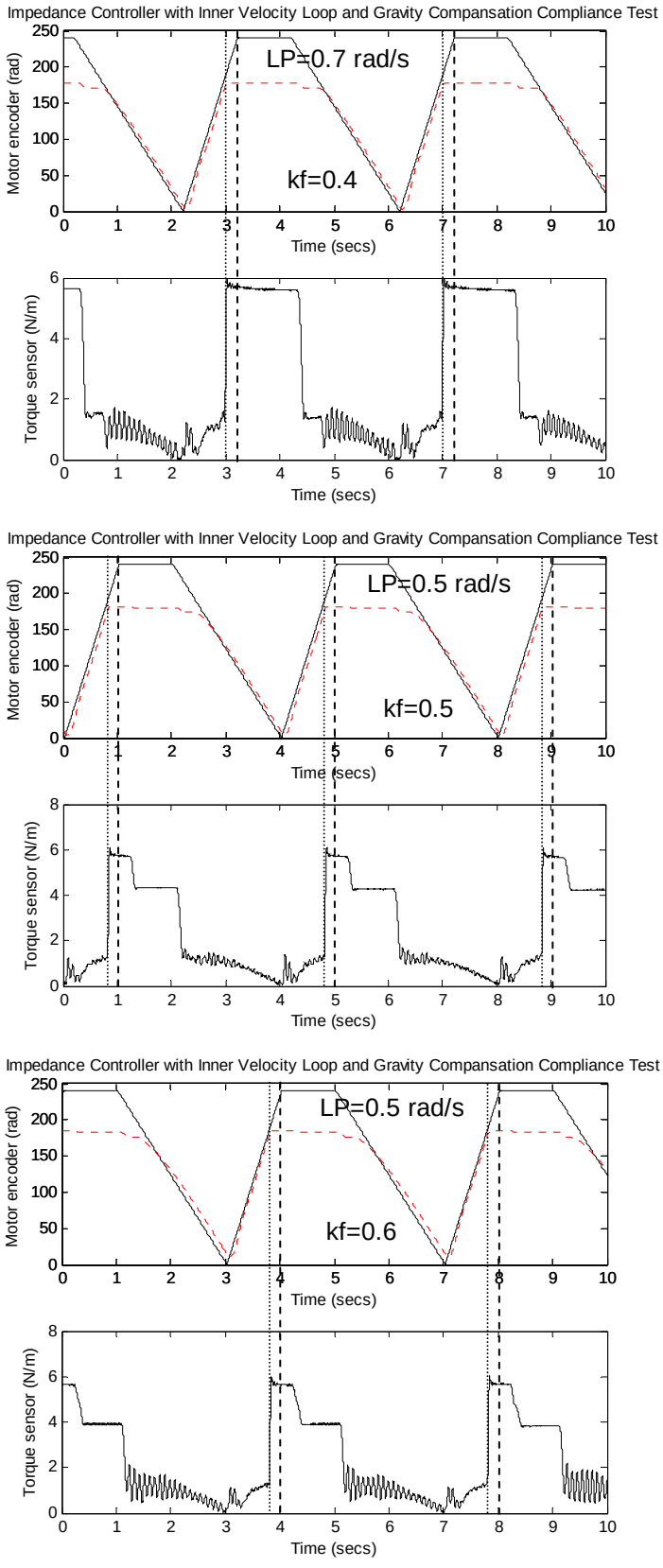

Figure 8.4-2: Compliance test by varying the force gain k_f of impedance controller with inner velocity loop and gravity compensation

The force gain factor k_f is gradually increased for more compliance. The low pass filter cut-off frequency is selected around 0.7-0.5 radians per second.

8.4.2. Summary

The inner velocity controller should be slow otherwise the velocity controller reacts faster to gear play in the system and this makes the system unstable. The tracking performance is as good as parallel position/force regulator.

About the filter design, the low pass filter is not good for the high frequency force responses such as collision with an object. The filter removes not only the backlash but also the desired impact torque, which is fast and removed by low pass filter. This makes the system response slower at the instant of impact. In order to improve this a sophisticated filter should be designed for discrimination and selection of collision torque against backlash torque. The low pass filter used in design has a 0.5 rad/s cut-off frequency in stability region. With the use of the very low frequency low pass filter response becomes very small.

The steady state contact torque/force is reasonable of operation if only a nice filter is used to prevent the high initial contact torque/force in the design.

Chapter 9

Screw Theory

This chapter will be the introduction to the screw theory, which is frequently used in robotics. For the design of the compliant controller on old MANUS, screw theory is used and for that reason the theory is covered in this chapter.

9.1. Introduction

The basic idea of screw theory will be addressed in this part. The reader is required to have basic knowledge of linear algebra since cross product; matrix transpose operation will not be covered in here. As we are dealing with the 3D *Euclidian* space generally three-dimensional cases will be considered.

Traditional vector product can be represented as

$$\wedge : \varepsilon_*(3) \times \varepsilon_*(3) \to \varepsilon_*(3); (v, w) \mapsto v \wedge w \tag{9.1}$$

where $\varepsilon_*(\mathrm{n})$ are the free vectors in *Euclidean* space. This operation changed in our case to a matrix multiplication and called as tilde operation

$$x = \begin{pmatrix} x_1 \\ x_2 \\ x_3 \end{pmatrix} \qquad \widetilde{x} = \begin{pmatrix} 0 & -x_3 & x_2 \\ x_3 & 0 & -x_1 \\ -x_2 & x_1 & 0 \end{pmatrix} \tag{9.2}$$

and (9.1) is rewritten as

$$v \wedge w = \tilde{v} w \tag{9.3}$$

Consider a 3 dimensional Euclidean space $\varepsilon(3)$. We can describe the position and orientation of every body by an element of the *Special Euclidean group* symbolized as $\mathrm{SE}(\mathrm{n})$. (Stramigioli, S., Bruyninckx, H., March 2001)

Now consider two right-handed coordinate frames within this space, Ψ_i and Ψ_j. A general change of Cartesian coordinates in $\varepsilon(3)$ from Ψ_i to Ψ_j can be expressed with a homogeneous matrix of the form:

$$H_i^j = \begin{pmatrix} R_i^j & p_i^j \\ 0_3^T & 1 \end{pmatrix} \tag{9.4}$$

where R_i^j is here gives the rotation of frame Ψ_i with respect to frame Ψ_j and belong to *Special Orthonormal* group of $\mathbb{R}^{3\times3}$.

$$R_i^j \in SO(3);\ SO(3) \in \{R \in \mathbb{R}^{3\times3}; R^{-1} = R^T, \det R = 1\} \tag{9.5}$$

and p_i^j is the displacement vector of frame Ψ_i from frame Ψ_j.

A useful property of the transformation matrices is that they can be cascaded to form transformation matrix from the frame of last *H* matrix to the first *H* matrix or vice versa.

$$H_d^a = H_b^a H_c^b H_d^c \tag{9.6}$$

9.2. Twist Concept

The instantaneous velocity of a rigid body in space is represented as twists in screw theory. A twist has six dimensions such that three of these represent the angular velocity around rotation axis and the other three represents the translational velocity of the rigid body along its rotational axis.

$$\mathrm{T_i^{k,j}} = \begin{bmatrix} w_i^{k,j} \\ v_i^{k,j} \end{bmatrix} \tag{9.7}$$

Twist of frame Ψ_i fixed in body i with respect to frame Ψ_j is represented in frame Ψ_k is shown in (9.7). $w_i^{k,j}$ is called as angular velocity and $v_i^{k,j}$ is translational velocity along the rotation axis. The twist is directly related with the coordinate transformation matrix H. The relation is

$$\tilde{T}_i^{i,j} = \begin{pmatrix} \tilde{w}_i^{i,j} & v_i^{i,j} \\ 0 & 0 \end{pmatrix} = H_j^i \dot{H}_i^j \tag{9.8}$$

$$\tilde{T}_i^{j,j} = \dot{H}_i^j H_j^i \tag{9.9}$$

Twists in (9.8) and (9.9) are represented in *tilde form* so they are 4x4 matrices. First one is twist of Ψ_i with respect to Ψ_j represented in Ψ_i and the latter one is twist of Ψ_i with respect to Ψ_j represented in Ψ_j.

According to the *chasles' decomposition theorem* (Chasles, M., 1830) any rigid body displacement can be represented by a rotation around a unique axis and a translation along that axis:

$$\begin{pmatrix} w \\ v \end{pmatrix} = \|w\| \begin{pmatrix} \hat{w} \\ r \wedge \hat{w} \end{pmatrix} + \lambda \begin{pmatrix} 0 \\ \hat{w} \end{pmatrix} \tag{9.10}$$

This formula illustrates in the following figure. In the figure twist of a rigid body in coordinate frame Ψ_i is shown.

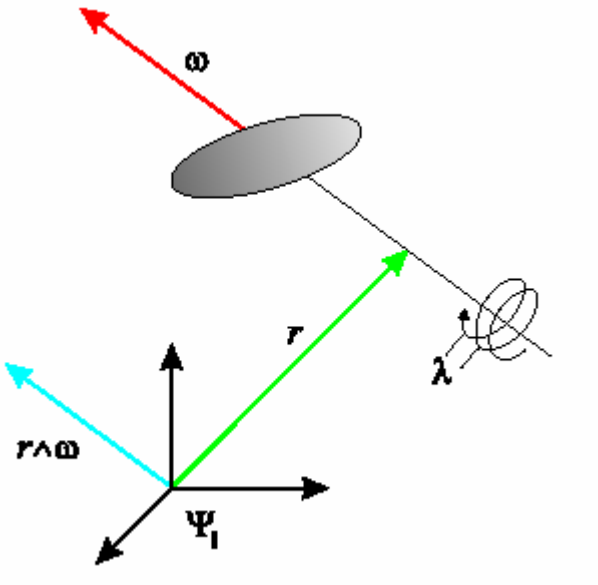

Figure 9.2-1: Intuition of twist

w is the angular velocity vector which passes through the rotation axis. r vector is any vector pointing the rotation axis of the rigid body from the reference frame. λ is the ratio of the translational velocity to the angular velocity. λ is also called as pitch of the screw motion.

9.2.1. Transformation of Twists

Twists are always represented in a reference frame, which lay on the *Euclidian* space. The reference frame may be located in any desired place or translated to another location. If the transformation from initial reference frame Ψ_j to Ψ_k is given with a transformation homogeneous matrix H_j^k the transformation of $T_i^{j,j}$ to $T_i^{k,j}$ can be in following way:

$$T_i^{k,j} = Ad_{H_j^k} T_i^{j,j} \tag{9.11}$$

where Ad matrix is

$$Ad_{H_j^k} = \begin{pmatrix} R_j^k & 0 \\ \tilde{p}_j^k R_j^k & R_j^k \end{pmatrix} \tag{9.12}$$

Derivation of (9.12) is given in (Stramigioli, S., Bruyninckx, H., March 2001).

9.3. Wrench Concept

In bond theory velocity-force couple is considered as power conjugate variables as they give an idea of power flow. In screw theory twist shows velocity behavior as it includes velocities of a rigid body. Similar to the velocity-force pair, peer of the twists are called as wrench, which gives the three dimensional relative force relation of the rigid body. Wrench is represented as

$$\tilde{W} = \begin{pmatrix} \tilde{f} & m^T \\ 0 & 0 \end{pmatrix} \tag{9.13}$$

where f represents linear force and m represents the torque on the body. These representations are all three dimensional so wrench is a six dimensional representation just like twist.

Wrenches can be decomposed according to the *Poinsot's Theorem*. (Poinsot, L., 1806)

$$W = \begin{pmatrix} \tau \\ F \end{pmatrix} = \underbrace{\begin{pmatrix} r \wedge F \\ F \end{pmatrix}}_{force} + \underbrace{\lambda \begin{pmatrix} F \\ 0 \end{pmatrix}}_{moment} \tag{9.14}$$

Illustration of this formula is given below.

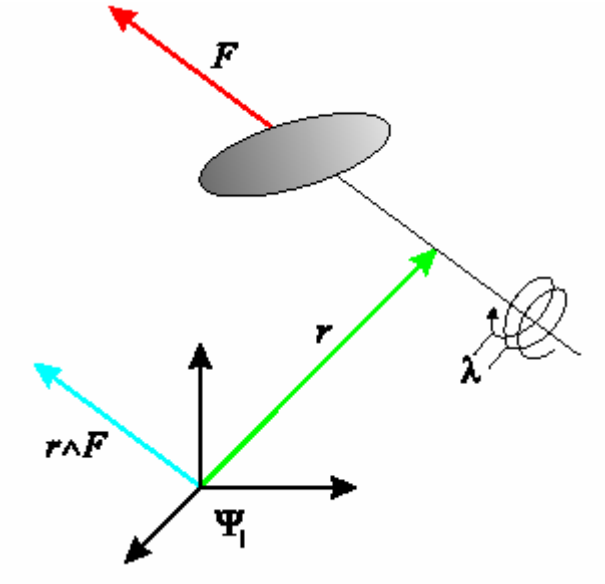

Figure 9.3-1: Intuition of wrench

This figure resembles to twists illustration. The only difference is w replaced with F.

The duality property holds between wrench and twist. If the mapping from Ψ_i to Ψ_j is shown as $Ad_{H_i^j}$ then the transformation of the reference frame of wrench is

$$\left(W^i\right)^T = Ad^T_{H_i^j} \left(W^j\right)^T \tag{9.15}$$

The duality property comes from the power relations of twist-wrench pair. In which frame this couple is represented does not change the power relations and implies that twist and wrench are power conjugate. As we mentioned in the previous part that the bond graphs are power and information transfer between elements, wrench and twist pair can also be represented in bond graphs as they denote power relations. Twist and wrenches can be represented in multi-bond graphs so called screw bond theory. In the following part a basic model which is commonly used in robotics modeling will be introduced.

9.4. Rigid Body with Screw Bond Theory

The robot that is intended to be modeled is following a trajectory in space. Therefore, each part of the robot behaves as rigid body in space. In order to derive the equation of rigid body it is better to start from the simple point mass.

$$p = mv \tag{9.16}$$

This is the basic equation we know for a long time and called as *Eulers equation*. After we take the derivate we get the *Newton's second law,*

$$f = \dot{p} = m\dot{v} \tag{9.17}$$

where we assume that m is not relativistic mass so it is constant. So force f is related with $\dot{v}$. If we consider the case also for rotational domain,

$$L = J\omega \tag{9.18}$$

we get

$$\dot{L} = \dot{J}\omega + J\dot{\omega} \tag{9.19}$$

L represents angular momentum. Since rotational inertia of the rigid body is constant equation can be reduced as

$$\tau = \dot{L} = \dot{J}\omega \tag{9.20}$$

According to the torque and force generalization, we can generalize this concept for rigid body, (Stramigioli, S., Bruyninckx, H., March 2001)

$$\underbrace{(P^i)^T}_{P} = \underbrace{\mathrm{I}^{k,j}}_{m}\underbrace{T_i^{i,0}}_{v} \tag{9.21}$$

P^i is called *momentum* screw and T is the twist of the body according to initial frame expressed in body frame. $\mathrm{I}^{k,j}$ represents *principal inertial frame* and can be calculated according to following formula,

$$I^{k,i} = \begin{pmatrix} J_i & 0 \\ 0 & m_i I \end{pmatrix} \tag{9.22}$$

where

$$J_i = \begin{pmatrix} j_x & 0 & 0 \\ 0 & j_y & 0 \\ 0 & 0 & j_z \end{pmatrix}$$

The generalized formula of Newton law for the rigid body can be written as,

$$\dot{P} = W \tag{9.23}$$

$\dot{P}$ is the time derivative of the momentum of the rigid body W is the applied wrench. After some more manipulations *Euler equation* of the rigid body can be obtain as following.

$$\underbrace{\left(\dot{P}^i\right)^T}_{1} = \underbrace{ad^T_{T_i^{i,0}}\left(P^i\right)^T}_{2} + \underbrace{\left(W^i\right)^T}_{3} \tag{9.24}$$

The derivation of this equation can be found in (Stramigioli, S., Bruyninckx, H., March 2001). First part of the equation gives the inertia internal total wrench of the inertia. Third part is the external wrench which means the force and torque represented in rigid bodies frame. Second part shows the gyroscopic effects of rigid body.

In this theory chapter basic bond graph theory including power direction, causality, and basic elements introduced. Then notion of screw theory is given by introducing transformation matrix, twist, wrench, and adjoint matrix. After the derivation of the *Euler equation* we done and ready for the modeling of any rigid body in space. For additional

information about the derivations or about the rigid body model in screw theory refer to (Stramigioli, S., Bruyninckx, H., March 2001).

Part III –Compliant Control Implementation on MANUS

Not every controller introduced in the Part I can robustly be implemented on the MANUS robotic arm series older than MANUS 502012. We will investigate in this part the reasons due to the mechanic and electronic design drawbacks of the arm. We will discuss how to improve it for the next design of the arm. These discussions will be in the direction of compliance controller application. Following this, we will formulate the kinematics problem encountered for all of the robotics systems. Kinematic formulation can be made in three steps: frame assignment, forward kinematics and inverse kinematics.

MANUS experimental setup is equipped with a force/torque sensor to be used in the control loop to make the robot end-effector compliant to the environment. In order to use the sensor information in the control loop information gathered from the sensor should be transformed and connected with the use of suitable compliant control strategy. We will merge into the details of these concepts and demonstrate the experimental results in this part. Consequently we will finish the thesis and discuss the overall results.

The layout of the report can be given in this way. Chapter 10 will introduce the MANUS experimental setup mechanics and electronics. In chapter 11 kinematic equations are derived. Force and moment transformations are elaborated in chapter 12. Compliant control strategies and experimental results of case studies are in chapter 13. The last chapter, chapter 14, concludes the thesis and discuss about the experimental results and experiences.

Chapter 10

Experimental MANUS Setup

MANUS is a personal robot, which can be classified as articulated elbow manipulator with spherical wrist and shoulder offset. With respect to its joint operation it looks more like PUMA 560 robot, which can be frequently seen in the literature. Additionally, a 6 DOF force torque sensor is attached between wrist and the gripper for compliant control experiments. Just like every other manipulator there are different generations of the MANUS. We used a MANUS_502012 in our experiments.

In this chapter we will discuss the necessary details of the electronics, firmware and the mechanics of the MANUS. The chapter includes some comments on the design drawbacks that might be corrected in the next generation of the robot.

10.1. MANUS Electronics and Firmware

In this part electronic connections of the experimental setup will be examined. Even though MANUS has its own embedded low-level controller it also let's the professional users to send the joint torques externally via *CAN Bus interface*. After the user sends the torques to the manipulator, the incremental encoder values of each joint can be obtained back. With this control loop it is possible to implement an external CAN Bus controller on the manipulator.

In our case the external CAN Bus controller is a real-time LINUX operating computer. A special kernel is developed in TNO-TPD industries for implementation of the controller in MATLAB for convenience. The generated real-time code in MATLAB can be downloaded via Ethernet link into the RT-LINUX system. In the real-time kernel the necessary modules for ISA CAN bus and PCI analog to digital converter has been built. The analog to digital converter interface card reads the 6 DOF force/torque sensor values after amplification. The connection schematics can be seen in the below figure.

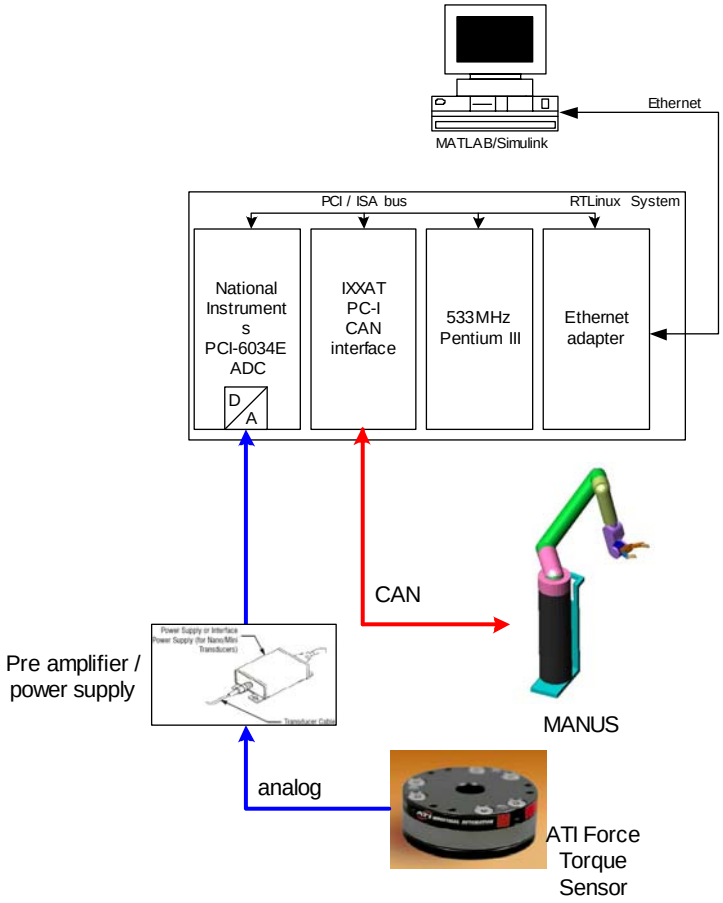

Figure 10.1-1: Electronic connection block diagram of the MANUS setup

The compact and rugged monolithic 6-axis force/torque transducer uses silicon strain gauges to sense forces. The transducer's silicon strain gauges provide high noise immunity and allow high overload protection.

The stand-alone controller outputs the forces and torques via the analog port, which is read by National Instruments A/D converter in the real-time computer side.

MANUS has 7 incremental and 6 absolute encoders for 6 DOF and the gripper states. Gripper doesn't have absolute encoder. The absolute encoders are only used to get the initial states then states are integrated by the values obtained by the incremental encoders. Since the response delay of the absolute encoders is around 2 seconds and indeterministic, it is not possible to get the absolute values after the motion is started.

10.2. MANUS Mechanics

10.2.1. MANUS Actuation and Transmission

The mechanics of the MANUS is quite complicated due to the placement of the actuators. Unlike many industrial robots, all of the actuators are placed in the body. Therefore, the transmission is getting complicated from joint 1 towards joint 6 and the dynamics of the transmission makes the stable control of the robot challenging. The exterior of the manipulator and the joints can be seen in the drawing included in the appendix. In the below diagram you may find a simplified demonstration of the manipulator DOF's.

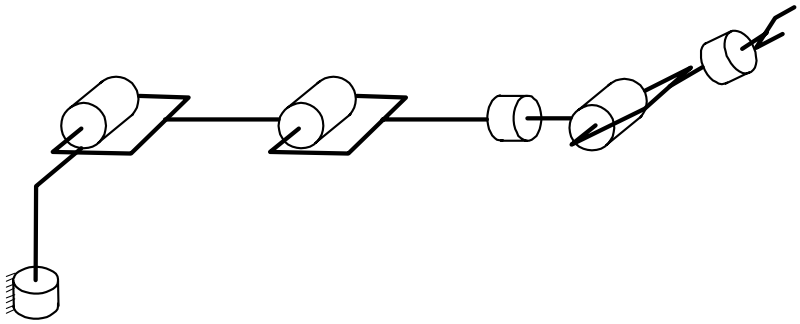

Figure 10.2-1: Schematic diagram of elbow manipulator with spherical wrist

In the design of the MANUS the actuators are placed in the base of the robot, which is only rotated by the first joint actuator. The reason for this is to reduce the power consumption with placing the heaviest components in the base. In this way the links will be lighter and as a consequence will require less power to be actuated. There is another problem to be concerned. The gravitational forces on the links could be either compensated by actuators or with mechanical strategies such as counter weight. Even counter weight seems to be a good solution; however, this might not be suitable for personal robots since the weight will rotate together with the robot will be hazardous. Thus, to make the robot exterior less complicated and to reduce hazardous situations on operation internal gravity compensation mechanism is utilized in MANUS. This mechanism is a different method than counter weight gravity compensation that is frequently used in the industrial robots. This mechanism compensates the gravity with the use of spring element.

The transmission of the power from actuator to the relevant link is conveyed by geared belts attached one another by different mechanical approaches. As a result, further links have more coupled transmission in the design. When the coupling increases the collocation between the actuation and the control point decreases and results less accuracy in the control of the robot gripper. Same problem is also mentioned in (Zollo, L., Siciliano, B., Laschi, C., Giancarlo, T., Dario, P. 2003) This is the main drawback of MANUS mechanical design. The gear belt connections of the links are out of this context. For further reading about this topic refer to (Koops, H.W., 1991).

The most important advantage of placing the actuators in the base is that there is no cabling passing inside the links. This means that the robot joints, except joint 5, can make more than one turn. This ability, however, does not add very much advantage to a personal robot. It might be useful for the tasks require more than one turn such as opening a screw bottle cap inside the workspace but for most of the tasks it is enough to have limited rotation.

On the other side, the actuator placement is a bottleneck for the attainable accuracy. As we mentioned before the transmission dynamics such as backlash, elasticity, and friction is dominant for the latter joints 4,5, and 6. These joints determine the pure rotation of the wrist, which is quite important for basic user tasks. For example if it is desired to track motions by attaching a camera to the wrist this accuracy problem will determine the performance of the system.

The absolute and the incremental encoders are all placed in the body where the actuators stay. The incremental encoders are collocated with the actuator shaft. The actuator shaft then connected to the gearbox then slip-couplings. The other side of the slip-couplings and absolute encoders are fixed together. The same shaft is connected to the gear, which is then connected to the geared belt. Geared belt systems then convey the power till the corresponding link. The motion of the gripper is motivated by a tie extending from the related actuator till the gripper.

A safety feature is included, as well, in the mechanical design. All the actuators have slip-couplings to prevent excessive torque applied on the manipulator links. This safety feature, however, only works for joystick control of the manipulator with user feedback. If we suppose that the user will always see the absolute position and orientation of the gripper this will be good for safe operation. Even there is a collision the manipulator will not apply more force/torque than what is set for slip-couplings. In another approach, if we rely only on the incremental encoders to determine the gripper coordinates, we will lose the absolute rotation information in case of a slip. One might think that it is possible to retrieve the absolute rotation information from absolute encoders. Unfortunately, as we mentioned before due to the non-deterministically delayed response of the absolute encoder data retrieval, it is not possible to recover the absolute rotation of the joints. Thus, for the force control experiments the slip-coupling feature is disabled.

10.2.2. Gripper

The mechanical structure of the MANUS gripper can be described in the following way. The gripper tips are designed to move parallel to each other to prevent the slip of the object between gripper. The tips are connected to the parallel bar structure that is driven by the 7th motor located in the body of the robot. The power from motor to gripper is transmitted via pulling the tie extending between the body and the gripper. The mechanics is illustrated in Figure 10.2-2.

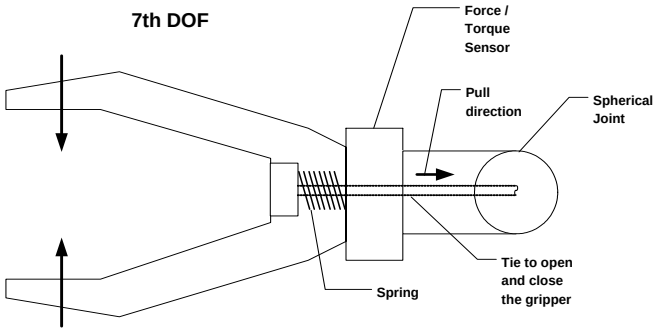

Figure 10.2-2: Gripper mechanism

The tie is passing from the joints in such a way that the joint torques are not affected when the gripper is closed, however the joint impedance increases since the tie changes the friction applying an axial normal force. This friction is mostly due to the use of washers instead of bearings at the bottom of the gripper. This is a major disadvantage of this gripper design. Furthermore, this impedance raise will increase when the washers are aging and for this reason it is making the control quite difficult and raise the necessity of advanced control strategies such as adaptive control.

Another important point that is necessary to be mentioned is the placement of the force/torque sensor between the gripper and the spherical joint. With this mechanical connection the tie to actuate the gripper passes inside the sensor. The problem raises again when the gripper is actuated in case the manipulator is under force/impedance/hybrid control. When the tie is pulled the force along the z-axis of the sensor directly reflects to the force sensor readings. In this case the manipulator may be actuated as if there is a force along the z-axis of the gripper coordinates. There may be a solution to this problem like resetting the z-axis force reading after gripping and releasing the object. This solution may first seem to be good. However, when we think of what will happen after the object slides accidentally from the gripper, the force controller may sense continuous non-existing force along the direction of the gripper. The other case might be when the gripper is moving along the plane where the gripper opens and closes which is shown in the below figure.

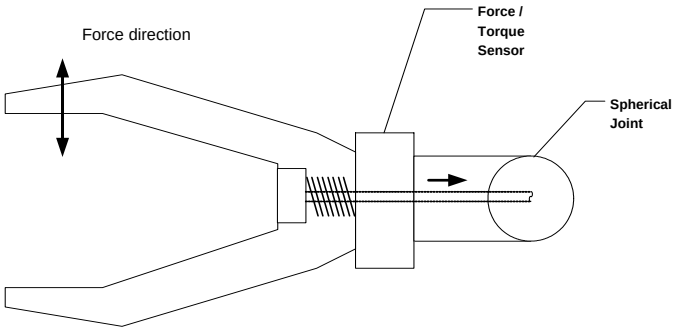

Figure 10.2-3: Disturbance force along x-axis of sensor coordinates

When there is force existing in this plane which forces to open and close the gripper the same problem will again occur. This might be the case simply when the gripper impacts an object in that direction or when opening a door in compliant mode. In order to avoid this problem in our experiments totally the gripper connection is cut and the gripper is fixed with rubber bands. This is only a temporary solution for force feedback operation and experimenting.

Chapter 11

MANUS Kinematics

Kinematics refers to the calculation or description of the underlying mechanics of motion of a spatial object without the forces that cause it. Within the science of kinematics position, velocity, acceleration and the higher order derivatives of the motion are studied.

In this chapter we consider position and orientation related situations of the manipulator. The MANUS mechanism is similar to the Unimation PUMA 560 robot. Both robots are elbow manipulator with spherical wrist. Hence, kinematic equations and their solution for PUMA 560 can be adapted to fit for MANUS as well.

11.1. Frames with Standard Names

As a matter of convention it will be helpful if we assign specific names and locations to certain "standard" frames associated with a robot and its workspace. Figure 11.1-1 shows a typical situation in which a robot has a two-fingered gripper and wishes to position the tool tip to a user-defined location. The five frames indicated below are so often referred to that we will define names for them. The naming and subsequent use of these five frames in a robot programming and control system facilitates providing general capabilities in an easily understandable way. All robot motions will be described in terms of these frames.

Brief definitions of the frames shown in Figure 11.1-1 are listed below.

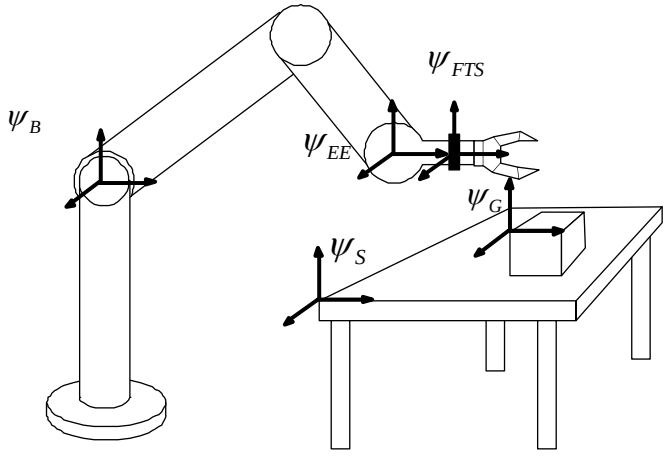

Figure 11.1-1: Schematic diagram of standard frames

- The base frame, ψ_B

ψ_B is located at the base of the manipulator. It is merely another name for frame $\{0\}$. It is affixed to a nonmoving part of the robot, sometimes called as link 0.

- The station frame, ψ_S

ψ_S is located in a task relevant location. Figure 11.1-1, it is at the corner of a table upon which the robot is to work. As far as the user of this robot system is concerned, ψ_S is the universe frame and all actions of the robot are made relative to it. It is sometimes called the task frame, the world frame, or the universe frame. The station frame is always specified with respect to the base frame, that is, H_S^B.

- The end-effector frame, ψ_{EE}

ψ_{EE} is affixed to the last link of the manipulator. It is another name for frame $\{6\}$, the link frame attached to the last link of the robot. Just like in MANUS very often ψ_{EE} has its origin fixed at a point called the wrist of the manipulator, and ψ_{EE} moves with the last link of the manipulator. It is defined relative to the base frame. That is, $\psi_{EE} = H_{EE}^B = H_6^0$.

- The force/torque sensor frame, ψ_{FTS}

ψ_{FTS} is placed at the centre of force/torque measurement device that is located in between end-effector and the gripper. The placement of the frame is where the forces and torques are measured. It is defined with respect to the end-effector, which is, H_{FTS}^{EE}

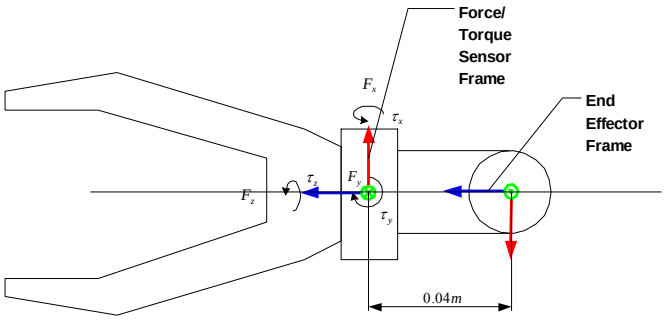

Figure 11.1-2: 6-DOF Force/Torque sensor frame placement

- The goal frame, ψ_G

ψ_G is a description of the location to which the robot is to move its tool tip. Specifically this means that at the end of the motion, the tool frame should be brought to coincidence with the goal frame.

Almost all robot motions may be described in terms of these frames without loss of generality. Their use helps to give us a standard language for talking about robot tasks. (Craig, J. J., 1989)

11.1.1. Tool Frame

One of the first capabilities a robot must have is to be able to calculate the position and orientation of the tool it is holding (or of its empty hand) with respect to a convenient coordinate system. That is, we wish to calculate the value of the tool frame, ψ_{EE}, relative to the station, ψ_S. Once H_S^B has been computed using the kinematic equations we can use D-H

transformation, as studied in Chapter 3, to calculate ψ_T relative to ψ_S. Solving a simple transform equation leads to

$$H_T^S = (H_S^B)^{-1} H_W^B H_T^W \tag{11.1}$$

This equation can be thought of as generalizing the kinematics. H_T^S computes the kinematics due to the geometry of the linkages along with a general transform (which might be considered a fixed link) at the base end (H_S^B) and another at the end-effector (H_T^W). These extra transforms allow us to include tools with offsets and twists, and to operate with respect to an arbitrary station frame.

11.1.2. Homogeneous Transformation vs. Quaternions

Rotation representations in robotics systems have two common forms. They are homogeneous transformation also called as D-H convention (Denavit, J., Hartenberg, R.S., 1955) and quaternion representation invented in early 1860's (Hamilton, W.R., 1866). We will briefly compare these forms considering their pros and cons as following.

The advantage of the quaternions over rotation matrices is that they require fewer multiply adds. Their disadvantage over homogeneous transforms is that you can't quickly simply group coordinate rotation-translation sequences and multiply them together. In our representations we will use homogeneous transformations.

11.2. Kinematic Equations for MANUS

This part has intentionally been removed since it was disclosing company confidential information.

11.3. Inverse Kinematics

This part has intentionally been removed since it was disclosing company confidential information.

11.4. Computational Consideration

In many practical manipulator systems, the time required to perform kinematic calculations is a consideration since it determines the real-time performance such as minimum time step. In this section we briefly discuss various issues involved in computing manipulator kinematics and its solution for the case of the MANUS.

One choice to be made is the use of fixed- or floating-point representation of the quantities involved. Many implementations use floating point for ease of software development, since the programmer does not have to be concerned with alignment operations due to the relative magnitude of the variables. However, when speed is crucial, fixed-point representation is quite possible because the variables do not have a large dynamic range, and these ranges are fairly well known. Rough estimations of the number of bits needed in fixed-point representation seem to indicate that 24 are sufficient (T. Turner, J. Craig, and W. Gruver, 1984).

By factoring equations it is possible to reduce the number of multiplications and additions at the cost of creating local variables, which is usually a good trade-off. The point is to avoid computing common terms over and over throughout the computation. There has been some application of computer assisted automatic factorization of such equations (W. Schiehlen, 1984).

The major expense in calculating kinematics is often the calculation of the transcendental functions, i.e., sine and cosine. When these functions are available as part of a standard library, they are often computed from a series expansion at the cost of many multiply times. At the expense of the required memory, many manipulation systems employ table lookup implementations of the transcendental functions. Depending on the scheme, this reduces the amount of time required to calculate a sine or cosine to two or three multiply times or less (C. Ruoff, 1981).

The computation of the kinematics is redundant in that nine quantities are calculated to represent orientation. It usually reduces computation by calculating only two columns of the rotation matrix and then compute a cross product (requiring only six multiplications and three adds) to compute the third column. Obviously, one chooses the two least complicated columns to compute.

11.5. Summary

We first assigned the coordinate frames that will be used in the rest of this report. We have employed the homogeneous transformations in order to describe the position and orientations of the MANUS end-effector. After that we gave the solution of the kinematic equations in inverse kinematics section. We then derive the computational complexity of the kinematic calculation. These are the basic steps to solve the kinematic problem of any manipulator.

Chapter 12

Force and Moment Transformation

In the MANUS experimental design we have a 6 DOF force/torque sensor attached to the wrist of the robot. The measurements made in the frame of the sensor must be translated into joint torques then into actuator torques. Conversion to actuator sub-space is necessary because the robot controller is working in the actuator subspace. As it will be shown in this chapter there is no easy way to design robot controller in joint space for the MANUS. The reason for this is unlike the other robotic systems the joints rotations are dependent on each other. As an example positive rotation of the fourth and the fifth actuator rotates the fifth joint but positive rotation of the fourth and negative rotation of the fifth activates the sixth joint.

After we translate the sensed force and torque to actuator space we can develop a control strategy to make the robot compliant. How can we achieve this transformation? The answer is hidden inside the Jacobians.

In this chapter we will give an introduction to the two Jacobians called manipulator and the actuator Jacobians. Using the duality property of power conjugation we will derive the force transformation equations. We then discuss the notion of singular configurations or singularities. In a singular configuration the Jacobian loses one or more degrees-of-freedom.

12.1. Jacobians

The forward kinematic equations define the relation of cartesian position and orientations of the end-effector in terms of joint space variables. The velocity relationship is then determined by the *Jacobian* of this function. The Jacobian is a matrix valued function and can be thought as the vector version of the ordinary derivative of a scalar function. Jacobian is one of the most important quantities in the analysis and the control of the robot motion. It is highly utilized in the planning and execution of the smooth trajectories, in determination of the singular configurations, in the execution of coordinated anthropomorphic motion, in derivation of the dynamic equations of motion, and in the transformation of the forces and torques from the end-effector to the manipulator joints.

In our case, the last one is the use of the Jacobian for the rest of this report. We will utilize two Jacobians, the manipulator and the actuator, to transfer the end-effector force and torque to the actuator space. Firstly, the 6- DOF end-effector force and torque will be transferred into six joint torques by the manipulator Jacobian. Then, with the use of the actuator Jacobian these six joint torques are transformed into actuator torques.

In the following subsections the derivations of the MANUS Jacobians will be given.

12.1.1. Manipulator Jacobian

A manipulator's differential change of its joint space dq_i causes the differential changes of its end-effector position and orientation of $\dot{H}_n^0$. In case of revolute joints, dq_i corresponds to a differential rotation and in case of a prismatic joint, dq_i corresponds to a differential change in the joint distance. In section of forward kinematics we developed the homogeneous transformation expression for the position and orientation of the end-effector coordinates in terms of product of joint transformations

$$H_n^0 = H_1^0 H_2^1 H_3^2 \dots H_n^{n-1} \tag{12.1}$$

Now we need a transformation that will map the joint velocities into the end-effector frame velocities what we call twist of tool frame $T_n^{0,0}$. From the definition of twist

$$\tilde{T}_n^{0,0} = \dot{H}_n^0 H_0^n \tag{12.2}$$

The homogenous transformation substitution of equation (12.1) into the twist formulation yields

$$\tilde{T}_n^{0,0} = \frac{d\left(H_1^0 \dots H_n^{n-1}\right)}{dt}\left(H_{n-1}^n \dots H_0^1\right) \tag{12.3}$$

Using the chain rule the equation can be written as

$$= \dot{H}_1^0 H_0^1 + H_1^0 \underbrace{\dot{H}_2^1 H_1^2}_{\tilde{T}_2^{1,2}} H_0^1 + \dots + H_{n-1}^0 \underbrace{\dot{H}_n^{n-1} H_{n-1}^n}_{\tilde{T}_n^{n-1,n}} H_0^{n-1} \tag{12.4}$$

From this expression using our knowledge of adjoint transformation of the twists to the other coordinates we can further simplify the equation

$$T_n^{0,0} = T_1^{0,0} + Adj_{H_1^0} T_2^{1,1} + \dots + Adj_{H_{n-1}^0} T_n^{(n-1),(n-1)} \tag{12.5}$$

This form is quite useful because it is easier to write the twists of a link in coordinates of the previous link rather that writing the twist of the link in base coordinates like

$$T_n^{0,0} = T_1^{0,0} + T_2^{0,1} + \dots + T_n^{0,(n-1)} \tag{12.6}$$

From the definition of a kinematic pair we have that

$$T_{i+1}^{i,i} = \hat{T}_{i+1}^{i,i} \dot{q}_{i+1} \tag{12.7}$$

where $\hat{T}_{i+1}^{i,i}$ is a unit twist and is constant since all joints are lower pairs and the velocity of the joint is extracted from the expression. Finally, we can define the jacobian matrix combining the two equations (12.6) and (12.7).

$$T_n^{0,0} = \mathbf{J(q)\dot{q}} \tag{12.8}$$

where

$$\begin{aligned} \mathbf{J(q)} &= (\hat{T}_1 \ \hat{T}_2 \ \dots \ \hat{T}_n) \\ \hat{T}_n &= Adj_{H_{n-1}^0} \hat{T}_n^{(n-1),(n-1)} \end{aligned} \tag{12.9}$$

$Adj_{H_n^0}$ depends on the joint position and can be calculated with the adjoint formulation however unit twist $\hat{T}_i^{(i-1),(i-1)}$ is constant. The columns of $J(q)$ are expressed in base frame and J(q) is called a *geometrical Jacobian*.

This 6x6 Jacobian matrix is usually called as *manipulator Jacobian*. It expresses the end-effector velocities in terms of joint velocities for a specific kinematic configuration. Besides, there is another general use of this matrix which is more important for us. The jacobian matrix can also be used to translate the end-effector forces into joint torques for revolutionary joints. This property comes from the duality of power conjugate variables. In our case the twists are power conjugates of the wrenches, joint velocities are conjugates of the joint torques. Similarly the actuator velocities can be matched with the actuator torques. Considering the ideal kinematic transmission (i.e. no friction) the power output should be equal to the power input we may write the equation in this way.

$$\begin{aligned} &P_{\text{actuators}} = P_{\text{joints}} = P_{\text{end-effector}}, \\ &\left(\boldsymbol{\tau}_{\text{actuators}}\right)^T \dot{\mathbf{q}}_{\text{actuators}} = \left(\boldsymbol{\tau}_{\text{joints}}\right)^T \dot{\mathbf{q}}_{\text{joints}} = \left(W^0\right)^T T_0^{0,n} \end{aligned} \tag{12.10}$$

From equation (12.8) we have the relation between joint velocities and the end-effector twist. Using this we may rewrite the power equilibrium in the following way

$$\begin{aligned} &\left(W^0\right)^T T_n^{0,0} = \left(W^0\right)^T \left[\mathbf{J(q)}\dot{\mathbf{q}}\right] = \left(\boldsymbol{\tau}\right)^T \dot{\mathbf{q}}, \\ &\left[W^0 \left(\mathbf{J(q)}\right)^T\right]^T \left(\dot{\mathbf{q}}\right) = \left(\boldsymbol{\tau}\right)^T \dot{\mathbf{q}} \end{aligned} \tag{12.11}$$

This equation states that

$$\boldsymbol{\tau} = W^0 \left(\mathbf{J(q)}\right)^T \tag{12.12}$$

Our goal was finding the transformation of the external forces and moments to joint torques. For this reason the dynamic effects due to the acceleration, friction of the joint, and the gravity were not considered. As an example, MANUS geometrical Jacobian is given in appendix.

Similarly, the same transformation holds for actuator Jacobian if an only if the mapping between the spaces is bijective like in our case. Using the transpose of actuator Jacobian we can translate the joint torques into actuator torques. Thus, we can show this formula with the following graph.

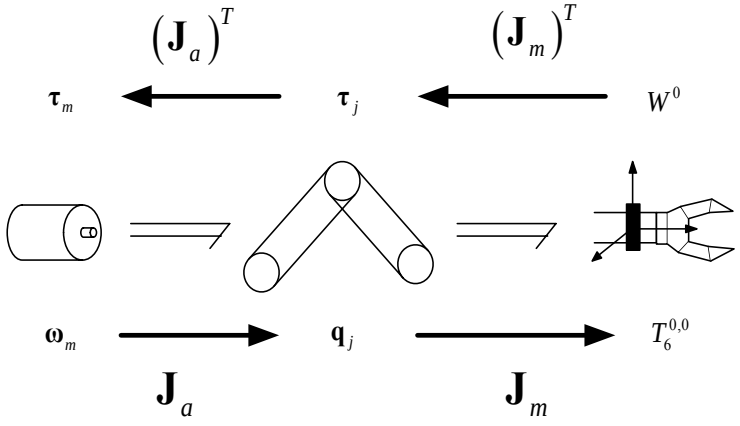

Figure 12.1-1: Power variable's transformation

12.1.2. Actuator Jacobian

We have shown the systematic way to transform the wrench from Cartesian space to the joint space with equation (12.12). Now in here we will give the general formulation of actuator Jacobian.

The joint velocities can be written in this way

$$\dot{q}_i = \sum_{j=1}^{6} \frac{\partial q_i(\boldsymbol{\theta})}{\partial \theta_j} \dot{\theta}_j \tag{12.13}$$

where every joint rotation q_i is a function of actuator variables θ_j. $\boldsymbol{\theta}$ is the vector form of the actuator variables. This formula can be generalized with the use of the actuator Jacobian given as

$$\mathbf{M}_a = \begin{bmatrix} \frac{\partial q_1}{\partial \theta_1} & \frac{\partial q_1}{\partial \theta_2} & \cdots & \frac{\partial q_1}{\partial \theta_6} \\ \frac{\partial q_2}{\partial \theta_1} & \frac{\partial q_2}{\partial \theta_2} & \cdots & \vdots \\ \vdots & \ddots & \ddots & \vdots \\ \frac{\partial q_6}{\partial \theta_1} & \cdots & \cdots & \frac{\partial q_6}{\partial \theta_6} \end{bmatrix} \tag{12.14}$$

And the final relation will be the following

$$\dot{\mathbf{q}} = \mathbf{M}_a \dot{\boldsymbol{\theta}} \tag{12.15}$$

where $\dot{\mathbf{q}}$ is the row vector of the joint velocities, $\mathbf{M}_a$ is the *6x6* actuator Jacobian matrix, and the $\dot{\boldsymbol{\theta}}$ is the row vector of the actuator velocities.

Note that the actuator Jacobian is constant when the relation between actuator velocities and joint velocities are linearly dependent in case of an elbow manipulator such as MANUS. Thus, comparing with the manipulator Jacobian actuator Jacobian is simpler because actuator Jacobian doesn't depend on the kinematic configuration. The actuator Jacobian for MANUS is given in appendix.

12.1.3. Singularities

Since the manipulator Jacobian is a function of kinematic configuration, those configurations for which the rank of $\mathbf{J}_m$ decreases are special significance. Such configurations are called *singular configurations* or *singularities*. Identifying manipulator singularities is important for several reasons.

- At singular configurations, finite end-effector velocities may correspond to infinite joint velocities. (i.e. at the boundaries of the work space)
- Singularities usually corresponds to the point on the boundary of the robot workspace
- Singularities correspond to the points in the workspace that can not be reached under small perturbations of the link parameters.
- Near singularities there will not exist unique solution of the inverse kinematics problem.

Here it is seen some of the singular configurations of the MANUS robot.

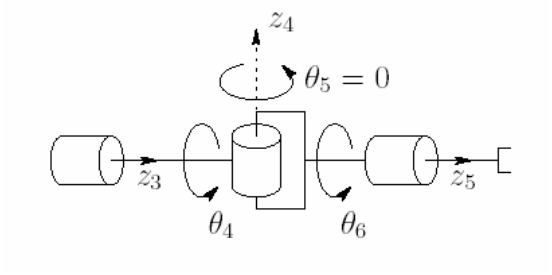

Figure 12.1-2: Spherical wrist singularity

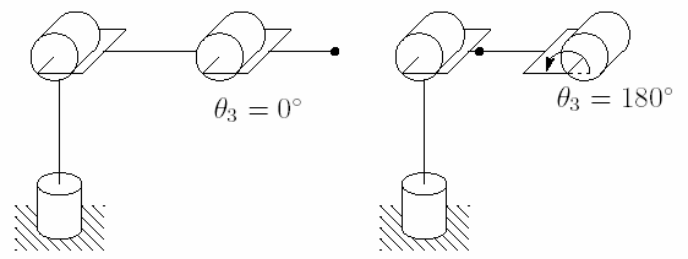

Figure 12.1-3: Elbow singularities

Chapter 13

Compliant Control Strategies on MANUS

In this chapter of the thesis the force control techniques applied on the MANUS will be introduced. In this way, the manipulator will be compliant for the environment. The user of this manipulator have various tasks to handle with the manipulator and almost all of them have physical contact with the environment, which means the manipulator might apply force on the objects. (Romer, G.W., Johnson, M., Driessen, B., 2003) The goal of the compliant control concerned here is minimizing the contact force while keeping the system stable for any kind of objects contacted. We will discuss that for each task different kind of compliant controller should be used to get high performance. In the following sections we will introduce, examine and validate successful two new design compliant controllers for different operations.

13.1. Introduction

When a manipulator is operating free (i.e., the tool is not in contact with any object), it is sufficient to specify and control the position and orientation of the tool. The majority of the robotic tasks, however, require constrained motion, wherein the motion of the robot is constrained by its environment. The robotic hand and the interacted environment therefore should have a certain amount of softness at either the tool or at the piece in contact. Classification of these constrained tasks and their models can be found in (Mason, M. T., 1981). In general for personal robots, since it may not be possible to control the softness of the environment, preferably, this softness is desired to be given to the tool either mechanically or within a compliant control strategy.

Mechanical softness can be attained with the use of relatively elastic materials such as springs, steel beam components. This simple method, however, statically defines the softness of the tool whereas for different kind of objects contacted softness should be adjusted. For example, the softness when the robot inserting a peg into hole should be different than when it is inserting an egg into the hole. Therefore, for different kind of objects in the environment the mechanically compliant tool head must be changed every time. On the other hand, the adjustment of the softness will be time and labour saving with the use of a suitable compliant controller strategy as it is defined numerically in the firmware for a digital controller. Besides, it would even be possible to dynamically adjust the compliant behaviour for advanced controllers.

There are many different kinds of compliant control strategies discussed in Chapter 4. Two of the most common used categories are hybrid (position/force) control and impedance control. These two controller categories are suitable for daily user tasks discussed in Section 2.3 because of their following characteristics:

1. Virtual spring behaviour of impedance controller is suitable for peg-in-hole or insertion operations
2. Softness of the impedance controller is suitable for impact reduction against environment.
3. Zero force/torque regulation of the hybrid controller category is suitable for constraint tasks where the external force on environment is minimum.

Using these two controllers, interaction with the environment of a complex transmission personal robot like MANUS can be handled successfully. To the best of authors knowledge, in the hybrid control category a new *force servo controller* will be introduced in this chapter. In the impedance control category a *force regulated impedance controller* is implemented. These two controllers are tested then with three benchmarking cases and tabulated according to the applicability for different tasks.

13.2. Low Level Controller Design

Before starting to introduce our compliant controller designs it is better to start with the core controller called low level controller (LLC). A position feedback loop is closed in actuator space as it is the best place to implement the position controller due to the previously discussed dynamical dependencies of the MANUS in section 12.1.2. For this reason LLC design is implemented in actuator space. The high level compliant controller is designed on top of this controller.

We have explained in Chapter 8 that the inner velocity and outer position (IVOP) controller has good performance for the systems which has large gear backlash. This is the main reason for choosing IVOP controller for the base of our compliant controller design as MANUS introduces more than 1 cm backlash in the end effector.

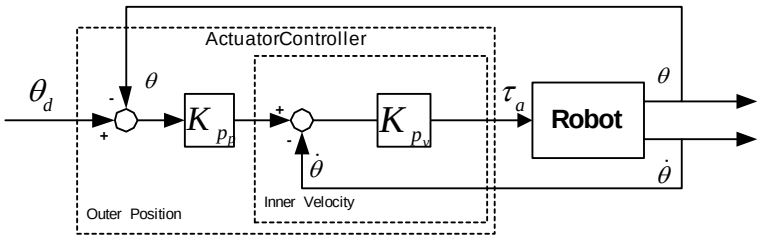

Figure 13.2-1: Inner velocity outer position controller

The IVOP used can be formulated in following way

$$\tau_a = \left(K_{p_p} (\theta_d - \theta) - \dot{\theta} \right) K_{p_v} \tag{13.1}$$

Here K_{p_v} is the inner velocity controller gain and regulates the speed of the actuator where the velocity feedback is coming from the actuator shaft incremental encoder. In case of gear bouncing the inner controller regulates the speed of actuator according to the position error of outer position controller. Outer position controller is a P type controller, of which stiffness is

determined by K_{p_p}. The gravitational forces are assumed to be fully compensated by the mechanical gravity compensation system of MANUS.

One other benefit of inner velocity controller is the inner velocity controller recovers the steady state error well without an integral action. (De Schutter, J., van Brussel, H., 1988) There should be no integral action in LLC to be able to adjust the compliancy of the controller.

13.3. Force Signal Filtering

Directly using the wrist force measurement in the force control loop is not preferable. The system could easily be unstable in case of a collision with a stiff environment since the measured impulse will not be filtered. The other drawback is that the system will not be immune to the force measurement noise. For these reasons filtering of wrist force measurement is necessary.

Without the wrist sensor in the force feedback loop, the dynamics of a simple manipulator in contact with its environment can be shown as in Figure 13.3-1.

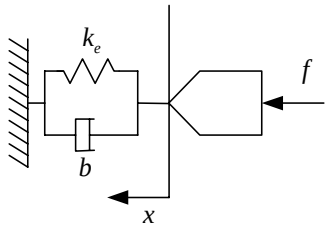

Figure 13.3-1: 1-DOF end-effector model in contact with the environment

The contact dynamics without the force sensor can simply be modeled with this equation.

$$f - k_e x = m\ddot{x} + b\dot{x} \tag{13.2}$$

where f is the commanding force or torque, x is the end-effector physical position with mass m and b is the damping of the environment.

If the system is driven purely by the actuator force f, in open loop, the system response might be under-damped since the stiffness of the environment k_e may be high. One most common used method is to create a dominant pole in the loop transfer function. This can be done simply by putting a low pass filter in the forward path so that,

$$f = B(s)\, f_m, \tag{13.3}$$

where f_m is the measured force or torque and $B(s)$ is the filter. A 4^{th} order Butterworth filter with a cut-off frequency of 8 Hz is used for MANUS. In order to show the difference of using low pass filter it is assumed that $m = 1,\ b = 10,\ \mathrm{k_e} = 10000$. The total constitutive relation is described by

$$x(s) = B(s)\, f_m \left(\frac{1}{ms^2 + bs + k_e} \right). \tag{13.4}$$

The compensated system behaves stable despite the existence of two high frequency under-damped poles. Figure 13.3-2 compares the step responses of above system with the original system without force filtered.

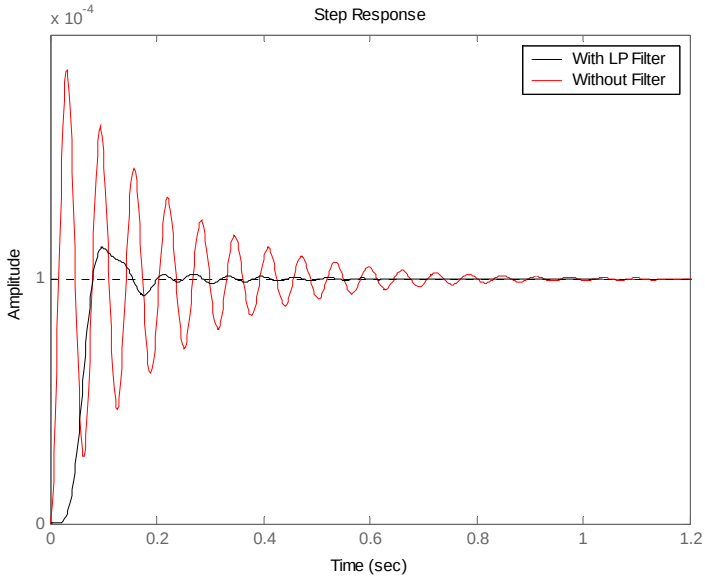

Figure 13.3-2: Step response of system in contact with and without Butterworth filter

It is seen that the system without force signal filtering has high oscillations due to the high frequency components in the force signal. For this reason the controller bandwidth should be reduced with the addition of low pass filter.

The Butterworth filter is indeed a discrete type filter running at 200 Hz sampling frequency. In order to prevent aliasing force sensor is over-sampled at 1600 Hz and then decimated to 200 Hz.

So far the basic elements force filtering and LLC of the two compliant controllers are introduced. Now we are ready to give here the definition and implementation of the two controllers with their experimental evaluation.

13.4. Force Servo Controller

In this section we will give the formulation, implementation, and experimental test of the force servo controller. This controller belongs to the hybrid controller category. The force servo controller, however, regulates the external force/torque to zero. In force servo control, depending on the task definition, necessary DOF is position controlled and the rest is force controlled.

First of all, a frame which is attached to the origin of the force sensor frame but has always same orientation with the world frame needs to be defined. This frame will be the motor frame which sets the reference translational and rotational velocities of the end-effector. Later, the dimensions will be filtered using the switching matrix **S** depending on the user task. The main reason for definition of this frame is many daily user tasks generally are defined in the world frame. For example, opening a door around the vertical axis corresponds to a rotation around an axis parallel to the z-axis of the world frame or pulling a drawer requires a translation along a vector in x-y plane of the world coordinates.

Definition of such a frame might be made in several different ways. In our approach the adjoint transformation matrix from sensor frame to the world frame is modified. The idea is if the position vector in the homogeneous transformation matrix, which composes the relevant adjoint matrix, is set to zero then using this adjoint matrix a transformation can be made from sensor frame to a frame which has the same orientation with the world frame but is on the sensor frame since the relative position is zero.

This new adjoint matrix can be derived from $Adj^{T}_{H^{ft}_{0}}$ responsible for transformation of the wrenches from sensor frame to world frame. The explicit form of this matrix will be given directly since the derivation of this matrix can be deduced from the information supplied in Chapter 9.

$$\left(Adj_{H^{ft}_{0}}\right)^{T} = \begin{bmatrix} R^{0}_{ft} & R^{0}_{ft}\tilde{p}^{0}_{ft} \\ 0 & R^{0}_{ft} \end{bmatrix}, \tag{13.5}$$

where R^{0}_{ft} is the rotation matrix and $\tilde{p}^{0}_{ft}$ is the tilde form representation of the position vector of H^{0}_{ft} which is the homogeneous transformation matrix from sensor frame to the world frame H^{0}_{ft}. As it is mentioned before to make the desired transformation the position vector $\tilde{p}^{0}_{ft}$ is set to zero and this changes the upper three rows which correspond to the torque in the wrench representation.

From this point the transformation is divided into two sections:

a) *Transformation of forces:*

The transformed force into world frame is, in deed, hidden inside the corresponding wrench $\bar{W}^{0}$. The overall transformation can be given with the following formula.

$$\left(\bar{W}^{0}\right)^{T} = Adj^{T}_{H^{ft}_{0}}\left(\bar{W}^{ft}\right)^{T} \tag{13.6}$$

This is not different than the wrench transformation property in equation(9.15). The frame name convention has been given in section 11.1. Here $\bar{W}^{0}$ represents the *1x6* wrench converted into world frame. $\bar{W}^{ft}$ denotes the force/torque measured by the sensor in sensor frame and H^{ft}_{0}, the homogeneous matrix from world frame to force/torque sensor frame, is calculated in real-time from the forward kinematics. After obtaining the external wrench in world coordinates we can get the forces from Poinsot Theorem (Poinsot, L., 1806).

$$\bar{W}^{0} = \begin{bmatrix} \bar{\tau}^{0} \\ \bar{F}^{0} \end{bmatrix}, \ \bar{W}^{0} \in \mathbb{R}^{6\times 1} \tag{13.7}$$

$\bar{F}^{0}$ is the *3x1* expression of the external forces in the world coordinates. $\bar{F}^{0}$ obtained from equation (13.6) is same as the desired conversion since its value does not depend on position vector p^{0}_{ft}. The upper 3 row of the matrix, $\bar{\tau}^{0}$, however, is not desired torque expression for the force servo controller since making p^{0}_{ft} zero changes its value.

For this reason another method is needed to obtain external torques in Cartesian space. It might be conceived that the screw theory has been misused here. However, the wrench $\bar{W}^{0}$ conversion is used since it is necessary for impedance control which will be described in next section.

b) *Transformation of torques:*

It has been seen from equation (13.5) that when the position vector p^{0}_{ft} is set to zero the torque transformation only depends on R^{0}_{ft} rotation matrix. Then the transformation from sensor frame to the world frame can be made by R^{0}_{ft} in this way

$$\bar{\eta}^{0} = R^{0}_{ft}\bar{\tau}^{ft} \tag{13.8}$$

After converting the force/torque sensor measurement into floating world frame attached to the sensor, the force servo controller equation is given by this formula

$$T_6^{0,0} = \mathbf{S}\widehat{T}_6^{0,0} + (\mathbf{I}-\mathbf{S})\begin{bmatrix} K_{p_\tau}\overline{\tau}^0 + \dfrac{K_{i_\tau}}{s}\overline{\tau}^0 \\ K_{p_f}\overline{F}^0 \end{bmatrix} \tag{13.9}$$

where $\mathbf{S}$ is the 6×6 diagonal selection matrix and has same size with the identity matrix $\mathbf{I}$. $\widehat{T}$ is the desired position input twist from the user. $T_6^{0,0}$ which is the twist of end-effector with respect to world frame in world coordinates, later, integrated in order to get H_6^0, homogeneous matrix showing the desired end-effector placement in world coordinates. With the use of inverse kinematics the end-effector coordinates are then transformed into joint rotation vector $\mathbf{q}_d$. The desired joint rotation $\mathbf{q}_d$ is then transformed into the desired actuator rotation vector $\boldsymbol{\theta}_d$ with the use of the inverse of the actuator jacobian $\mathbf{M}_a^{-1}$ given in Equation (12.14). $\boldsymbol{\theta}_d$ is finally passed to the LLC.

While giving the formulation of the force controller we assume the availability of the following information and conditions.

1. The kinematic Jacobian, $J(q)$ is full rank in trajectory during task accomplishment.
2. The inverse kinematic solution exits and is unique during the task.
3. The reference trajectory $H_6^0(t)$ is inside the workspace of the robot.
4. The mapping from the actuator space to the joint space is bijective. Then the inverse of the manipulator jacobian $\mathbf{M}_a^{-1}$ exists.

Force servo controller utilizes PI type controller for the rotational axes and P type controller for the translational axis. The overall schematic of the force servo controller is given in Figure 13.4-1.

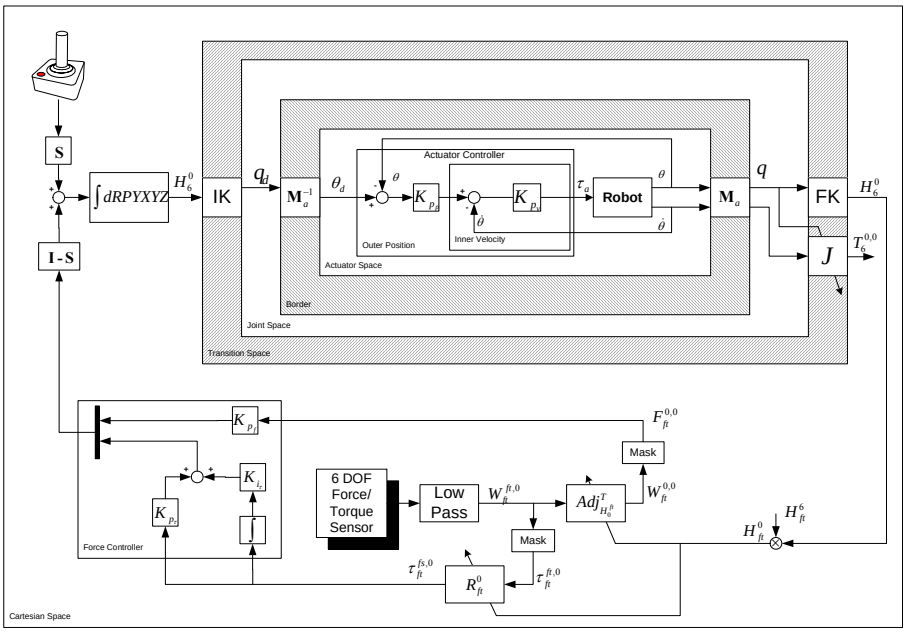

Figure 13.4-1: Force servo control block diagram

In the figure for force servo controller there is two 3x1 vectors which are $\tau_{ft}^{fs,0}$ and $F_{ft}^{0,0}$. $\tau_{ft}^{fs,0}$ is the transformation of the measured torque from the sensor frame into the desired force servo frame which has the same orientation with the world frame but its origin collocated to the sensor frame origin. On the other side $F_{ft}^{0,0}$, representation of the measured force in world frame, is same as the transformation of the measured force from the sensor frame into the desired force servo frame as it is explained earlier. Mask blocks are used to select the desired components of the wrenches. For torque selection force component of the wrench is removed and vice versa.

Validation of this controller is made with two case studies. First one was opening a screw bottle, which is a helical constrained motion. Later, the controller is tested with pulling a door, which constitutes a circular constraint motion.

13.4.1. Case Study: Opening the screw bottle cap

Opening a bottle cap is more complicated than twisting door handle since the action is a screw type constrained motion and it requires more rotations around the screw axis. For more than one rotation around the screw axis, the force along the pitch direction can not be neglected. For this reason this task can be used as a benchmarking test for rehabilitation robots of which wrist is capable of multiple rotations.

While opening the screw bottle cap all translational axes should be controlled by force servo since there will be an extra motion due to the pitch of the screw different than twisting a door handle. This requirement is enough to set switching matrix $\mathbf{S}$ given in the formulation of the controller. Only the rotational axis screw axis is necessarily to be controlled by the user, as the translational axis errors will be recovered from the zero external force requirement of the force servo controller.

In this experiment a bottle is opened using force servo controller in XY translational axis of the base frame. Even though rotation about Z-axis constrained due to the screw motion that

axis is not connected to force servo just to observe the force along Z-axis. The rotation about Z-axis of the base frame (Y- axis of end effector frame) is controlled with joystick in other words with position controller.

In Figure 13.4-2 the trajectory of the end-effector in X-Y plane is seen with some of the time points. The symbolic end-effector shape is superimposed on the graph to give a better visualization of the task.

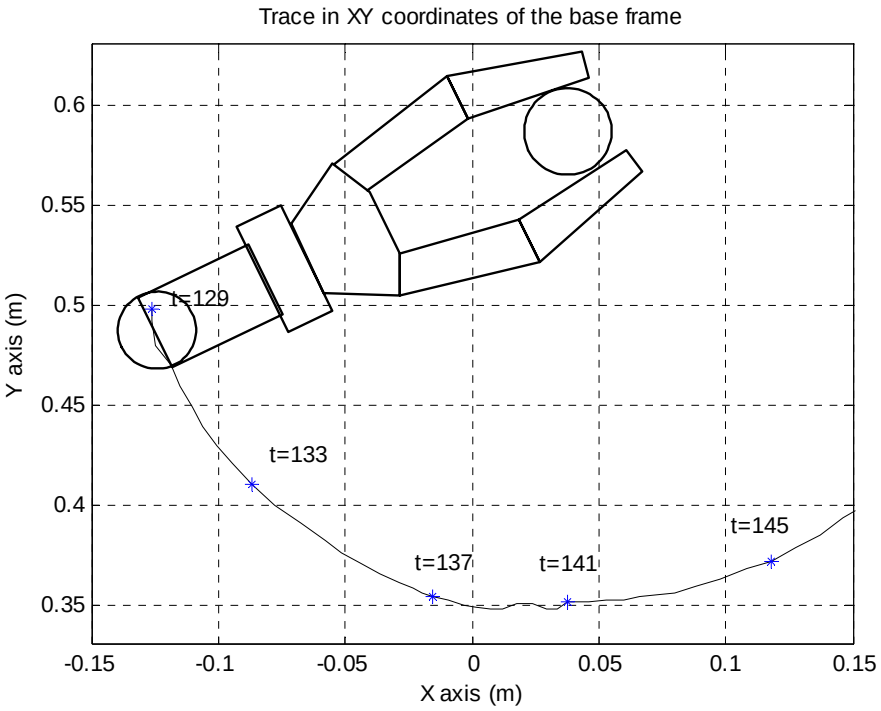

Figure 13.4-2: The trace of the end effector frame while opening a screw bottle cap

The tracking performance is measured and the average rotational tracking error is found around 2 degrees. Tracking performance can be seen in Figure 13.4-3 together with the contact torque and force measurements. From the figure it is seen that the steady-state forces in X and Y axes are zero. These axes are those under control of the force servo-controller. For this case study the effect of screw pitch can be seen from the force measurement along the Z axis. The rotational axes X-Y should be controlled by force servo controller however to see the screw axis misalignment problem they are set as position controlled. As it is expected the X-Y rotational axes measurements more or less show 120 degrees sections of a sinusoidal wave. This also shows that only one axis needs be controlled and the other five axes should be left for force servo controller.

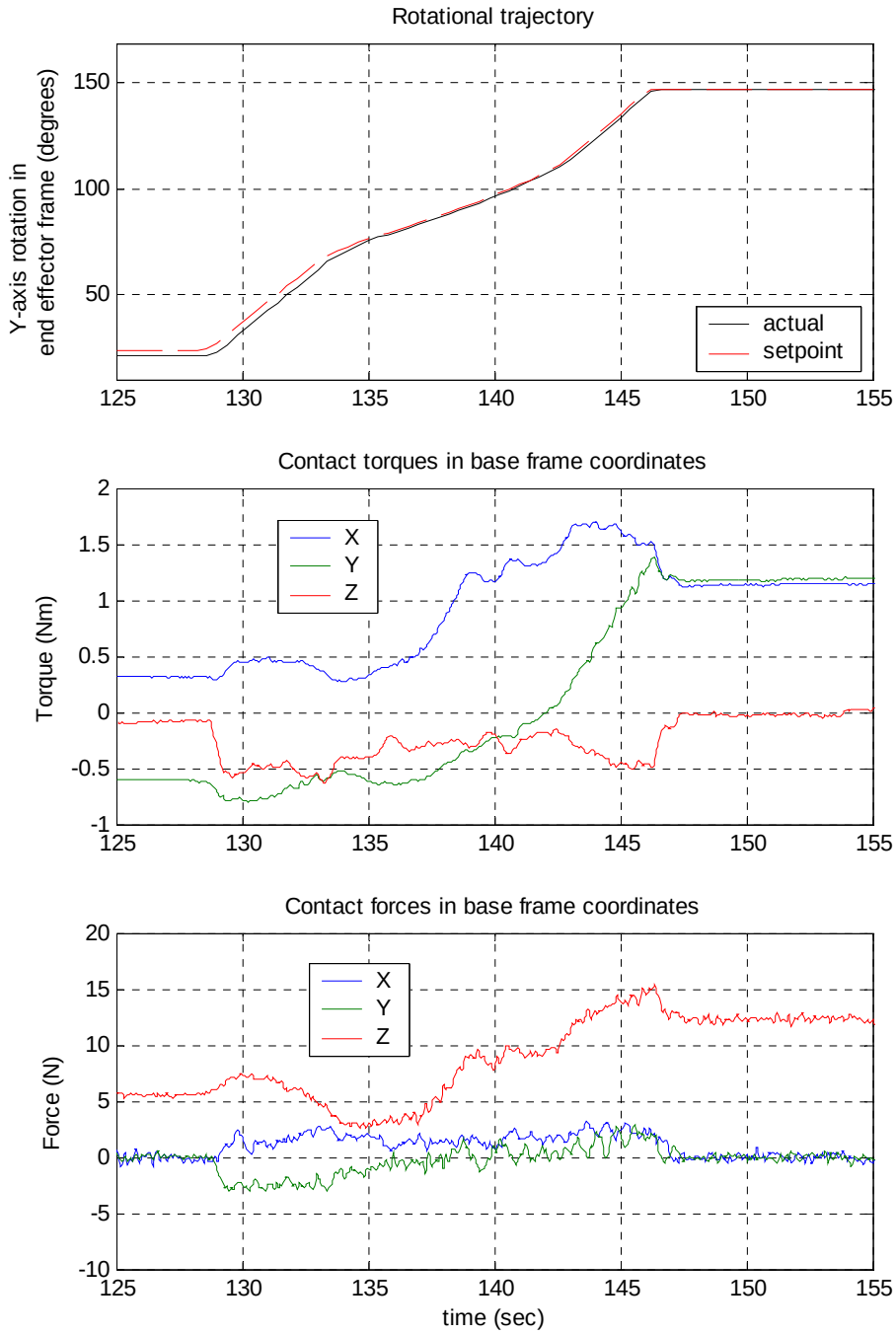

Figure 13.4-3: Rotational trajectory and torque/force measurement

During the force servo case studies given controller parameters are used.

	q1	q2	q3	q4	q5	q6
K_p (Outer Position)	30	16	27	12	8	8
K_p (Inner Velocity)	1.2	2.0	1.8	1.4	1.4	0.6
K_p (Rotational Force Servo)	10^{-7}	10^{-7}	10^{-7}	10^{-7}	10^{-7}	10^{-7}
K_I (Rotational Force Servo)	10^{-10}	10^{-10}	10^{-10}	10^{-10}	10^{-10}	10^{-10}
K_p (Translational Force Servo)	10^{-2}	10^{-2}	10^{-2}	10^{-2}	10^{-2}	10^{-2}

Table 13.4-1: Force servo controller parameter table

From here we see how an impossible task with joystick control is possible using force servoing.

13.4.2. Case Study: Pulling the door

Revolute constraint motion type experiment is commonly used as a benchmark testing of the compliant controllers. One of those is given in (Zollo, L., Siciliano, B., Laschi, C., Giancarlo, T., Dario, P. 2003) without evaluation of the force and torque measurements.

In this experiment a door opening and closing problem is considered. The end-effector is loosely clamped to the door side with the gripper as shown in Figure 13.4-4. The door rotation axis is placed parallel to the z-axis of the world coordinates so the constraint motion takes place in x-y plane. The constraint motion can be given with these formulas.

$$\begin{aligned} x^2 + y^2 &= R^2 \\ \cos(\theta) v_x + \sin(\theta) v_y &= 0. \end{aligned} \tag{13.10}$$

where R is the radius of the circular motion, x and y are the location in the frame illustrated in Figure 13.4-4. v_x and v_y represents the velocities in relevant axes. θ is the rotation of the door.

In traditional methods there are three ways to handle this problem. (Mason, M. T., 1981)

1. Use the planned value for θ, computed from the goal trajectory.
2. Compute the θ from the actual manipulator's z rotation in real time.
3. Compute θ from the manipulators position in the x-y plane in real time.

These three methods suffer from the unplanned stray due to the slip of the gripper resulting large trajectory errors. With the appropriate use of the force servo controller this task can be accomplished only commanding one of the degree-of-freedoms. In this case the y-direction is commanded and the x-direction and rotational axis z is left for force servo controller.

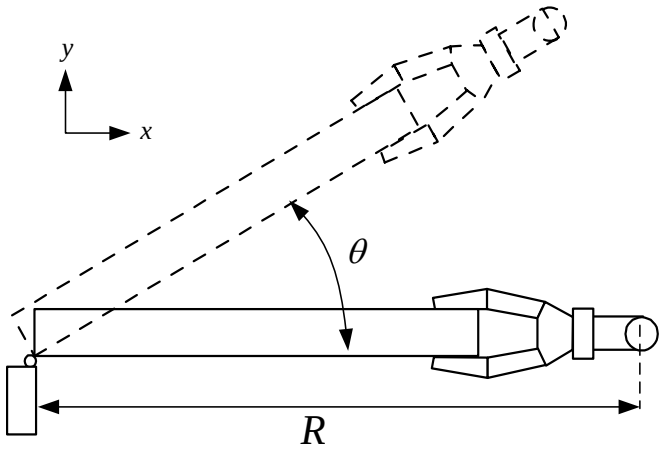

Figure 13.4-4: MANUS door opener

The trajectory of the end effector is shown in Figure 13.4-5. Here the door is pushed forward and pulled back around 20 cm in y axis.

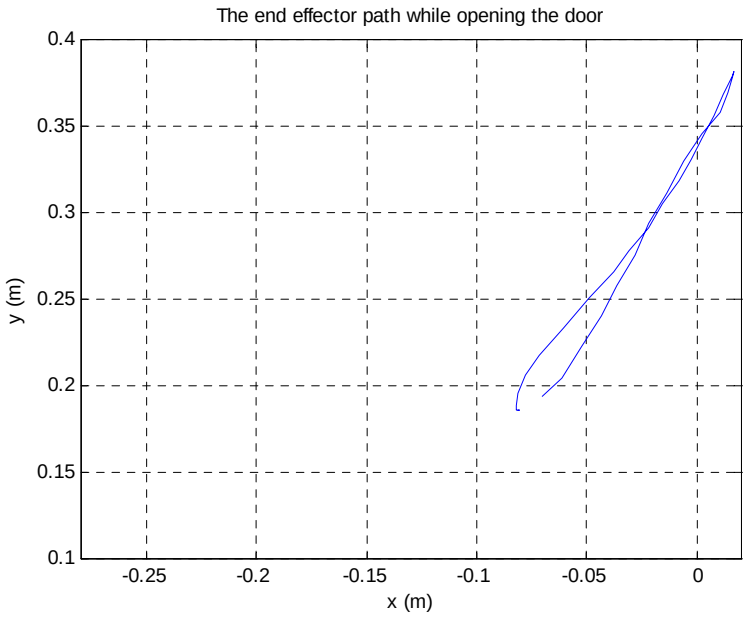

Figure 13.4-5: Path of end effector while opening the door

During this experiment the controller parameters are set with the parameters given in Table 13.4-2.

	q1	q2	q3	q4	q5	q6
K_p (Outer Position)	30	16	27	12	8	8
K_p (Inner Velocity)	1.2	2.0	1.8	1.4	1.4	0.6
K_p (Rotational Force Servo)	10^{-7}	10^{-7}	10^{-7}	10^{-7}	10^{-7}	10^{-7}
K_I (Rotational Force Servo)	10^{-10}	10^{-10}	10^{-10}	10^{-10}	10^{-10}	10^{-10}
K_p (Translational Force Servo)	10^{-2}	10^{-2}	10^{-2}	10^{-2}	10^{-2}	10^{-2}

Table 13.4-2: Force servo controller parameter table

While the manipulator was following the motion profile an average of 5 mm tracking error occurred. The maximum torsion in world coordinates are recorded as 0.7 Nm and the maximum force occurred with 6 N.

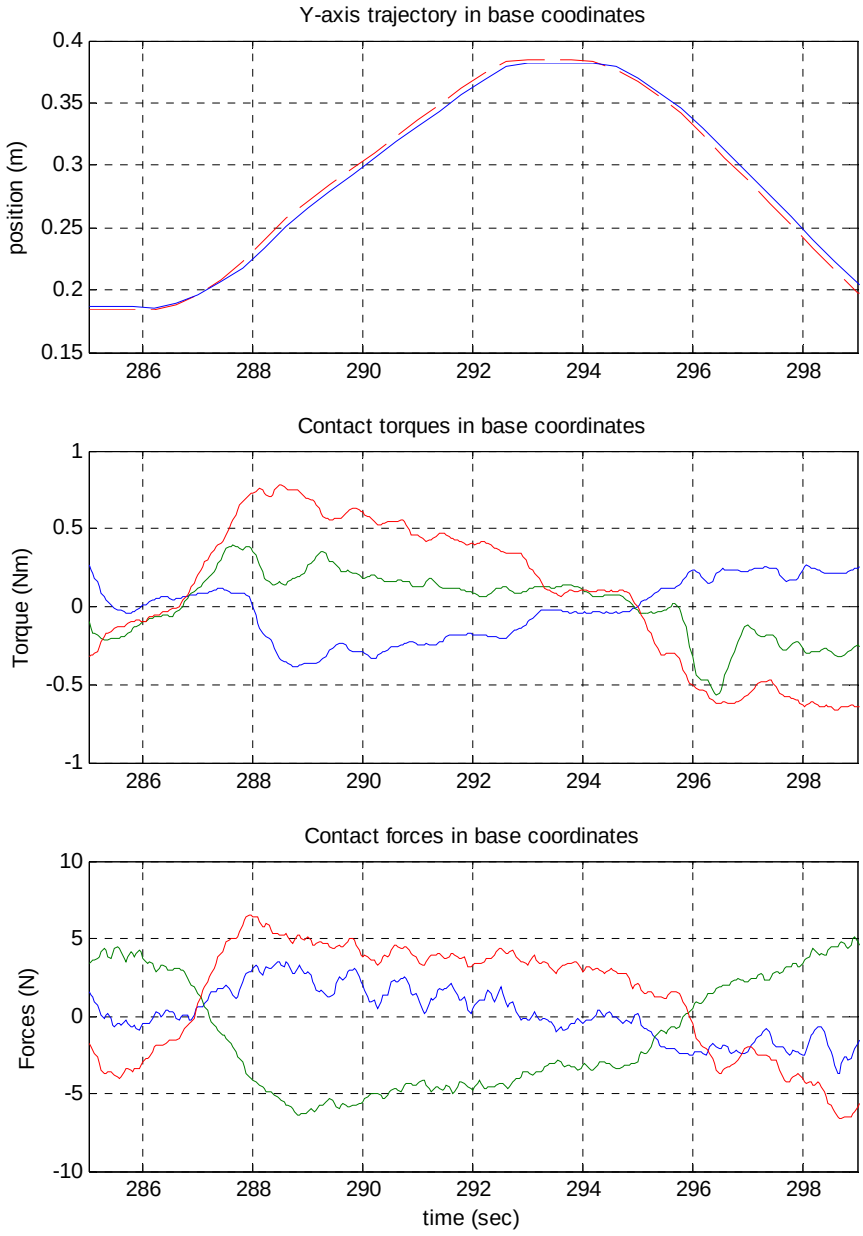

Figure 13.4-6: Trajectory along the y-axis and the torque force readings while opening the door

13.5. Force Regulated Impedance Control

The idea behind force regulated impedance control (FRIC) is that the joint compliance can autonomously be varied as a function of the external wrench. In case of contact with the environment the compliance of the LLC controller increased exponentially with the detected external force.

The impedance controller is placed under joint space different than force servo controller which is working in Cartesian space. The controller takes the external wrench in world frame

which is later translated into joint space as an input and modifies LLC compliance working in actuator space.

While introducing the force feedback controller we described the coordinate transformation of the sensed wrench in force/torque sensor frame into a frame which has same orientation with the world frame but has same origin with the sensor frame. In this transformation $\overline{W}^0$, the external wrench in world frame, has partially been used. However, in FRIC this wrench is completely used. It is transformed into joint space by Jacobian. The wrench transformation into joint torques has been discussed in chapter 12. According to conservation of the energy the relation was given with this formula

$$\overline{\boldsymbol{\tau}}_l = \overline{W}^0 \left(\mathbf{J}_m(\mathbf{q})\right)^T \tag{13.11}$$

$\overline{\boldsymbol{\tau}}_l$ stands for the translated external joint torque column vector and the $\mathbf{J}_m(\mathbf{q})$ is the geometrical manipulator Jacobian calculated with equation (12.8). The next step is the formulation of the regulation parameter vector $\boldsymbol{\beta}$

$$\boldsymbol{\beta} = e^{-\mathbf{K}_{\mathbf{pf}}|\overline{\boldsymbol{\tau}}_l|} \tag{13.12}$$

where $\mathbf{K}_{p_f}$ is the impedance control weight vector controls the impedance of the related joint. $\boldsymbol{\beta}$ vector regulates the LLC compliance by directly effecting the outer loop gain after being translated into the actuator space with $\mathbf{M}_a^{-1}$ which is the actuator Jacobian inverse. The adaptive control law is given as

$$\tau_a = \left(K_{p_p}\left(\mathbf{M}_a^{-1}\beta\right)(\theta_d - \theta) - \dot{\theta}\right)K_{p_v} \tag{13.13}$$

The force regulated impedance controller reduces the gains of the outer position loop with the factor of $e^{-K_{q_n}|\tau_{q_n}|}$ where τ_{q_n} is the translation of external forces into joint torques and K_{q_n} is the reduction parameter. The amount of the reduction can be seen in Figure 13.5-1.

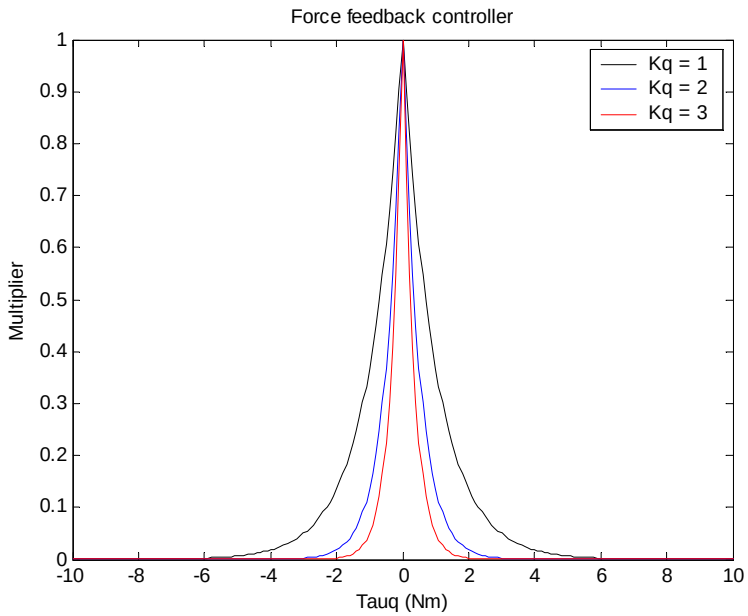

Figure 13.5-1: Force feedback multiplier

The desired coordinates are again translated into joint rotations by inverse kinematics then into actuator rotations by inverse actuator jacobian. The overall controller schematic is given in Figure 13.5-2.

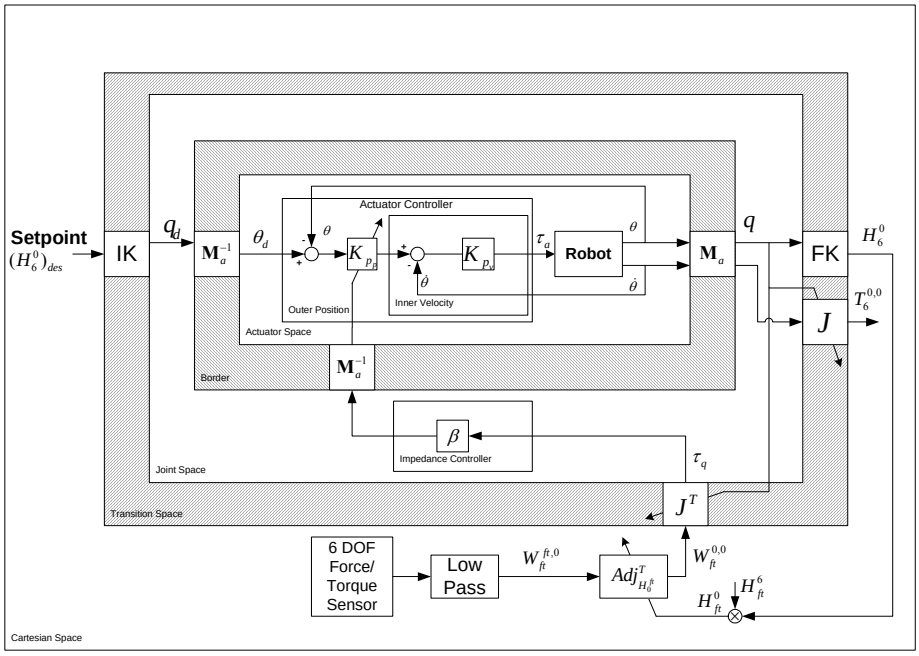

Figure 13.5-2: Impedance control block diagram

13.5.1. Case Study: Impact on box test

In this experiment the gripper is placed slightly above a wooden box on the table. The gripper is then descent in Z-axis of base frame within the limit of 30 N that the manipulator can handle. The impedance of the controller is observed. Then the same experiment is repeated with the impedance control.

Without impedance control the desired position is set to 2 cm below the actual position and the reaction force is observed as 30 N along Z-axis. The experimental measurements of the tracking performance is given in Figure 13.5-3 and the resulting counter force is plotted in Figure 13.5-4.

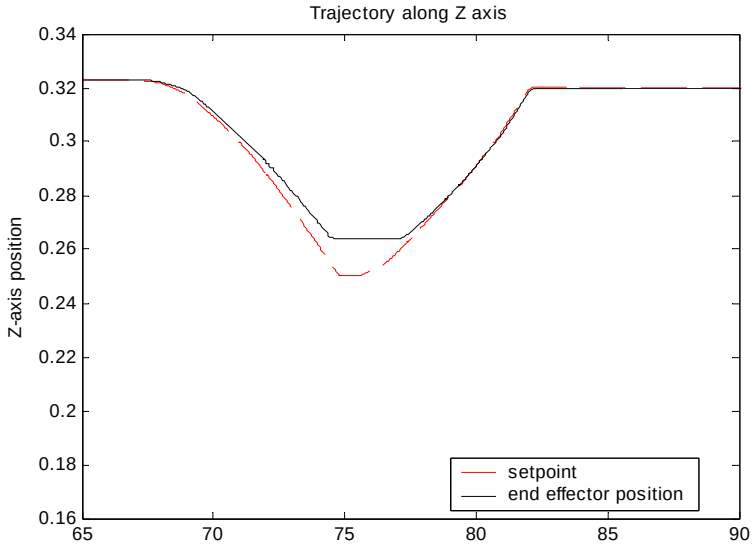

Figure 13.5-3: The trajectory without impedance controller

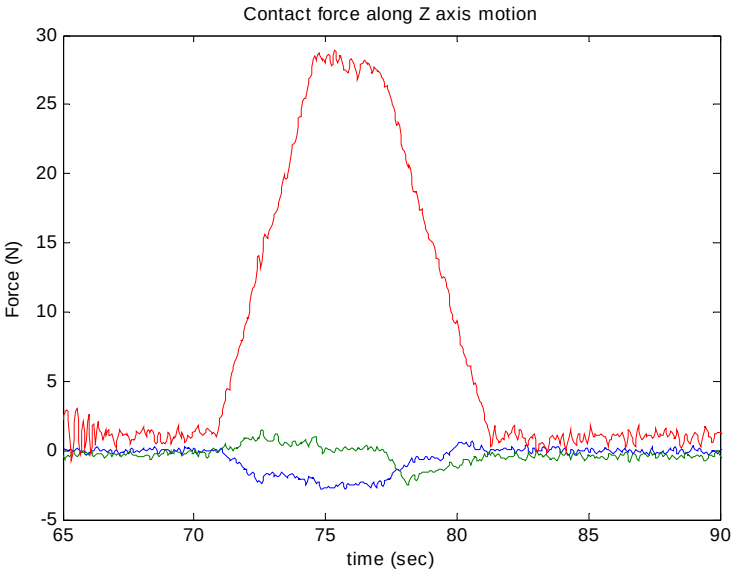

Figure 13.5-4: Force readings without impedance controller

The experiment is repeated with the impedance controller on the same object. This time the end-effector desired height is set 10 cm below the contact surface and around 7 N force is measured on the object. With this result given in Figure 13.5-6 the force regulated impedance controller is found 21 times compliant than the normal position control. If we look at the tracking performance of the controller shown in Figure 13.5-5 it is not worse than the position controlled MANUS.

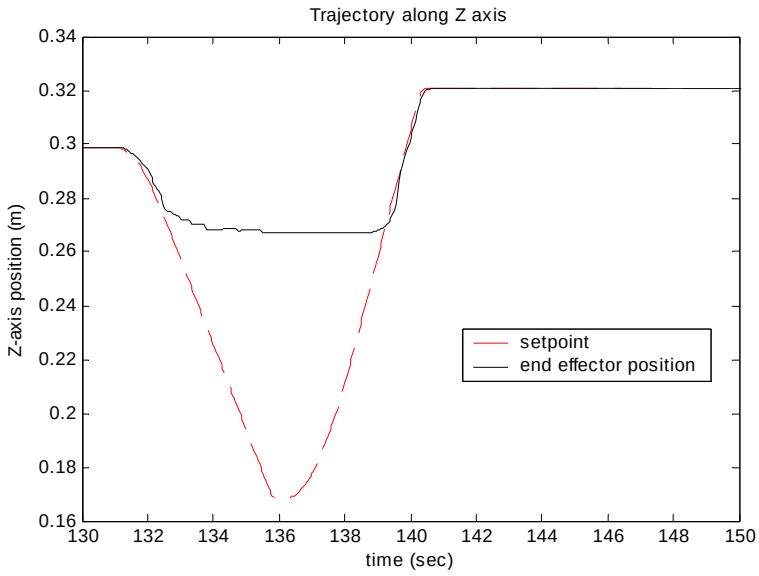

Figure 13.5-5: The trajectory with impedance controller

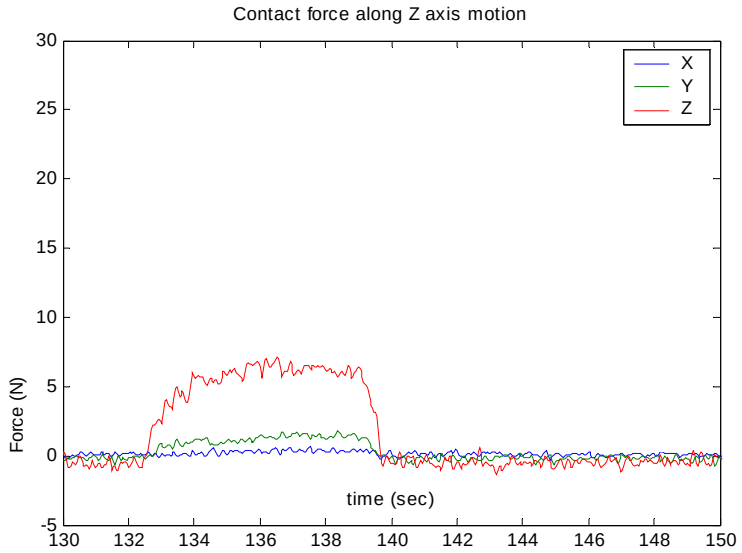

Figure 13.5-6: Force readings with impedance control

The controller parameters are given in the table.

	q1	q2	q3	q4	q5	q6
K_p (Outer Position)	30	16	27	12	8	8
K_p (Inner Velocity)	1.2	2.0	1.8	1.4	1.4	0.6
K_p (Force)	1.0	2.0	3.0	1.0	0.1	0.1

Table 13.5-1: Impedance controller parameter table

From this experiment it is seen that the impedance control could reduce the amount of force exerted on the object to 7 N. It is also observed that the performance of the controller is inversely proportional with the low pass filter delay.

As a conclusion, force regulated impedance control is more suitable for free motion of the-end effector with the probability of collision with an object. However, the impedance control

might also suitable for some type of the constraint operation such as insertion tasks. For the other kind of constraint tasks force servo controller can be used as it is shown in the bottle opener case study. Switching between two controllers many difficult daily user task can be accomplished.

Chapter 14

Conclusion & Discussion

This thesis was composed of three parts. In the first part we researched available compliant control strategies applied to the robotic manipulators. Later, in the second part we identified, modeled the 1-DOF experimental setup of new generation MANUS and applied several control strategies including the observer-based controller in order to improve external force detection. Finally, in the third part we built hybrid and impedance controllers in order to ease achievement of daily life tasks by a rehabilitation robot.

As a summary of the Part-I we have investigated several categories of controllers. The most primitive one is active stiffness controller (ASC), which the compliance is achieved with the expense of tracking. Later, the parallel position/force regulator (PPFR) is experimented and giving good tracking and compliance to the system. This type is very satisfactory and is applicable to the systems with dynamically complex structures since it is not necessary to have dynamic model. This controller also has very high noise rejection and is robust. The attainable compliance of this type of controller is inversely proportional with the amount of backlash. Finally, we have inspected the impedance control with inner velocity loop (ICWIVL). This controller gave motivating results since steady state contact force is as good as PPFR. The vibration due to the gear backlash is less than PPFR. The stability of the controller is limited with the performance of the torque sensor low pass filter. And the design of this filter determines the impact force duration of the ICWIVL. For more detailed information read the related summaries of the each controller type.

Several control strategies are treated in Part-I with experimental results. In both class either dynamic or static model-based approaches parallel position/force controllers also known as hybrid controllers gave desired behaviors for the alignment and constraint tasks.

The new design of the MANUS gives availability of the application of the dynamic model-based approaches since the mechanical complexity of the design will be simpler than the older versions. Implementation of the dynamic model-based controller on the old MANUS will require the identification of friction and elasticity parameters which are dominant dynamic characteristics of it in addition to well known inverse dynamics parameters. Thus, compliant control with resolved acceleration is not suitable for the old MANUS due to its complex mechanical transmission.

When the stability issues are considered static-model based control looks more robust for the application of force control on the previous MANUS versions. Advance adaptive control,

however, can be implemented to overcome problems caused by dynamic parameter uncertainty.

Nevertheless, if we design a non-complex robot for instance a direct drive manipulator without complex gravity compensation mechanisms or a non-flexible body manipulator it is better to use dynamic model based controller to reduce the impact force. The dynamic model based controllers also have good tracking behaviors. The dynamic model based controllers are robust for the systems with low backlash. As a conclusion of Part II, for the mechanical design the flexibility and the backlash of the system should be adjusted so that they will not be dominant on the force/torque measurement.

Finally, we can compare wrist force/torque sensing to joint torque sensing. It is crucial to choose which method is suitable for the application. Wrist sensor provides an accurate high bandwidth force/torque measurement at the hand. Since the robot mechanism is low bandwidth and the sensor placed at the end of the manipulator has low noise immunity, high gain force feedback can make the system easily unstable. For this reason a slow force feedback might guarantee the stability. On the other hand, since the joint torque sensors are placed close to the actuators, it is possible to increase the bandwidth of the force feedback. As the sensors are not at end-effector this time it is not possible to be sensitive to the hand forces and torques due to the manipulator dynamics.

The main disadvantage of using wrist force/torque sensor is non-observability of arm collision detection. When the arm surface instead of wrist collides with an obstacle on the trajectory the robot will not be compliant any more. This is potentially dangerous if the possibility of collision of the arm with environment is considered. This hazard can be reduced using the torque sensors in the joints or using tactile sensors implanted on the surface of the robot arm.

14.1. Matching of Tasks with Control Strategy

In Part III we have presented a critical analysis of feasible two interaction control schemes implemented on MANUS, 6+1 DOF personal robotic manipulator, realized for rehabilitation robotics. These two schemes are not compared with each other since they are in the different domains. With the use of only these two schemes, force servo and impedance control, many difficult user tasks are proven to be accomplished much simpler then before. Some of the frequent user tasks have been listed in Table 14.1-1. The corresponding control method for each task is given as well.

Tasks	Rotational Axes			Translational Axes		
	R_x	P_y	Y_z	X	Y	Z
Opening a bottle cap about Z-axis	-	-	JC	FS	FS	FS
Pulling a door along Y-axis	FS/-	FS/-	FS	FS	JC	-
Dragging box on the table	-	-	-	JC+IC	JC+IC	-
Inserting DVD into player along Y-axis	IC	IC	IC	JC+IC	JC+IC	JC+IC
Twisting the door handle	-	JC	-	FS	FS/-	FS
Pulling a drawer	FS/-	FS/-	FS	FS	JC	-
Operating a switch	-	-	-	-	JC+IC	-

Table 14.1-1: Table of control actions for various tasks

FC : Force servo control
IC : Impedance control
JC : Joystick control (Position control)
Legend

Experimental results show that difficult tasks such as opening a bottle cap can be aided with the use of force servo controller. The impedance controller reduced the interaction forces from 35 N to 7N.

According to the Table 14.1-1 sensation of all axes force/torque is necessary. For this reason a 6 DOF force/torque sensor must be used. Having less DOF force/torque sensor will narrow the ability of the compliant controller.

14.2. Assessment of the MANUS

According to our experiences with the MANUS arm we found it suitable for laboratory experiments. With the use of the TNO-TPD build real-time Linux kernel it is possible to quickly run controller models designed in Matlab Simulink interface. Rapid prototyping capabilities increase with real-time acquisition of the experimental data to the Simulink platform.

At the same time, we encountered a number of difficulties with the MANUS arm mechanically and electronically. The design of the mechanical setup for the new generation MANUS has a drawback. In order to control to compensate the backlash of the setup it will be better to increase the resolution of the absolute encoder 15 times of the current one. Then the translated incremental encoder resolution will be comparable with the absolute encoder when both encoders are in control loop.

As regards the actuation, MANUS arm shows a series of critical problems, such as non-linear friction, coupling in the degree of freedom. Coupling in the degrees of divides the control space into three. It also reduces the applicable controller strategies since some of them are implemented in upper space.

Another problem is the absolute encoders in the MANUS_502012. The encoders are not suitable for the real-time operation since they have a response latency of around 6 sec. According to experiments on average every 2 seconds it is possible to get new absolute values. Furthermore the latency is indeterministic. This poses double trouble.

As we pushed performance limits, flaws in the MANUS emerged rather than conceptual problems with the controllers. The 2 cm play of the end-effector limit us to get better results from stable compliant controller.

14.3. Recommendation

The control strategy can be extended to advanced control such as adaptive or learning control for compensation of the friction in order to increase the accuracy. For the redesign of the MANUS the mechanical complexity should be reduced. The mentioned problems in this thesis should be taken into consideration while designing the new robotic arm.

The bandwidth of the system is increased from 100 Hz to 200 Hz on 533 MHz PC/AT. This fact proves that the code is optimized. This also shows that the implementation can also be done on embedded platforms such as PC104 systems for compact operation.

We have seen both wrist and joint force/torque sensing have good and bad features. In the newer designs these two methods can be combined to increase the bandwidth and stability. This might be done using lower bandwidth economic 6-dof force/torque wrist sensor and 6 joint torque sensors.

Appendix A 1-DOF Setup Components

Necessary parameters from the datasheets supplied by the vendor are given below.

Data Sheet Values

Incremental Motor Encoder

Model N^{o}	HEDL-5540 A11
Manufacturer	Maxon (http://www.mpm.maxonmotor.com/)
Count per turn	500

Incremental Shaft Encoder

Model N^{o}	EDH751-3-1024-05-T-S/1m
Manufacturer	INDUcoder (http://www.inducoder.de/)
Count per turn	4096

DC Motor

Model N^{o}	A-max 32 Order# 236647
Manufacturer	Maxon (http://www.mpm.maxonmotor.com/)
Power	15 W
Nominal Voltage	24 V
Torque Constant	38.2 mNm/A = 0.0382 Nm/A
Speed Constant	250 rpm/V = 26,18 rad/sec/V
Terminal Inductance	1.05 mH
Terminal Resistance	7.13 Ohm
Rotor Inertia	41.9 gcm^2 = 4.19x10^{-6} kgm^2

Planetary Gearbox

Model N^{o}	GP 32 A Order# 166170
Manufacturer	Maxon (http://www.mpm.maxonmotor.com/)
Reduction Ratio	123:1
Backlash	1 degree
Mass inertia	0.7 gcm^2 = 0.7x10^{-7} kgm^2

Servo Amplifier

Model N^{o}	4-Q-DC Servo amplifier LSC 30/2
Manufacturer	Maxon (http://www.mpm.maxonmotor.com/)
Max. output current	2A
Set value range	-10…+10 V

Rotary Torque Sensor

Model N^{o}	2200-5.0 V06
Manufacturer	Fast Technology (http://www.fast-sensors.com/)
Torque conversion	213.66 mV/Nm
Nominal Torque Range	0 to 5.0 Nm
Bandwidth	1 KHz

Bellow Coulings

Model N^{o}	MK2/100/50
Manufacturer	R+W (http://www.rw-antriebselemente.de/)
Torsional Stiffness	9050 Nm/rad

Measured and calculated parameters

Load and Link Inertias

Load inertia	1.83×10^{-2} kgm^2
Link inertia	3.14×10^{-2} kgm^2

Identified LuGre Friction Parameters

Coulomb friction	α_0	0.35 Nm
Stribeck friction	α_1	0.14 Nm
viscous friction	α_2	1.4 Nm/rad/s
bristles stiffness	σ_0	0.4×10^{6} Nm/rad
bristles damping	σ_1	2.5×10^{3} Nm/rad/s
Stribeck velocity	v_{sk}	0.2×10^{-3} rad/s

Appendix B 1-DOF Setup 3D View

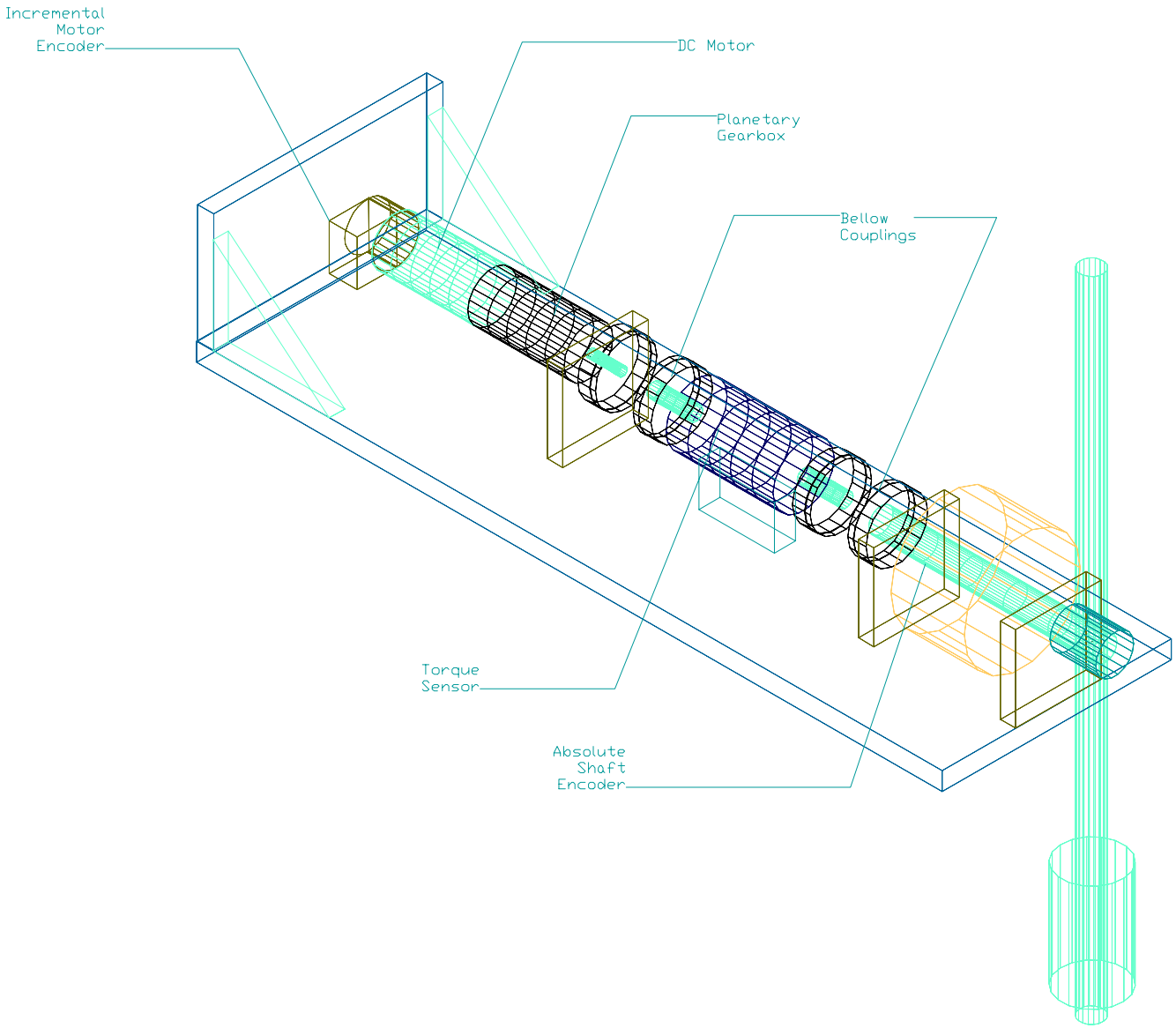

Appendix C MANUS Technical specifications

Arm	
DOF:	6 + 1 (gripper) + 1 (lift, optional)
Dimensions:	See figure
Reach:	80 cm (31.5”)
Weight:	14.3 kg (31.5 Lb)
Payload:	1.5 kg (3.3 Lb)
Repeatability:	± 1.5 mm (± 0.06 ”)
Max. velocity:	9.9 cm/s (3.9 ”/s)
Max. rot. vel:	30˚/s (0.52 rad/s)
Power supply:	24V DC, 1.5A (nominal), 3A (peak)
Gripper	Two fingered, with hinged fingertips ensuring three-point grasping
Grasp force:	20N (4 Lb’s)
Max. opening:	9 cm (3.5”)

Appendix D MANUS Setup Components Technical Description

Necessary parameters from the datasheets supplied by the vendor are given below.

Data Sheet Values and Prices

6 Axes Force/Torque Sensor

Model N^{o}	Mini 45 SI-580-20
Manufacturer	ATI (http://www.ati-ia.com/)
Sensing Fx, Fy Range	580 N
Sensing Fz Range	1160 N
Sensing Tx, Ty Range	20 Nm
Sensing Tz Range	20 Nm
Price	EUR 6,316.- (including sensor reader)

ADC (Analog Digital Converter)

Model N^{o}	NI PCI-6034^{E}
Manufacturer	National Instruments (http://www.ni.com/)
Inputs	16 Analog – 16 Digital
Sampling frequency	200K samples/s
Price	EUR 525.-

Can Bus Interface

Model N^{o}	PC-I 03
Manufacturer	IXXAT (http://www.ixxat.de/)
CAN Controller	Philips SJA 1000 (2x)
Price	EUR 277.-

MANUS

Model N^{o}	502012
Manufacturer	Exact Dynamics(http://www.exactdynamics.nl/)
DOF	6+1
Reach	80 cm
Weight	14.3 kg
Payload	1.5 kg
Repeatability	±1.5mm
Power Supply	24V DC, 1.5A (nominal), 3A (peak)
Gripper	Two fingered with hinged finger tips
Grasp Force	20 N
Maximum Grip Opening	9 cm
Price	EUR 25000,-

Appendix E MANUS Technical Drawing

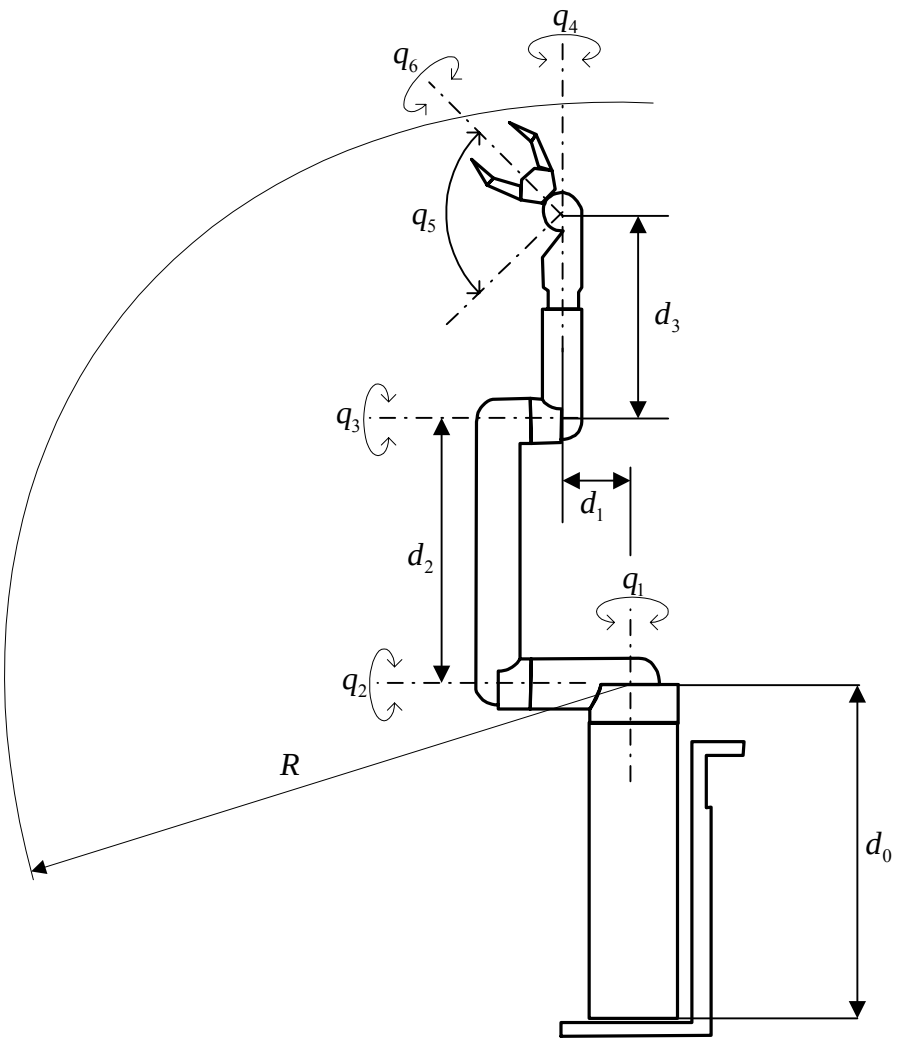

Bibliography

Books

An, C.H., Atkeson, C.G., Hollerbach J.M., “Model-Based Control of a Robot Manipulator”, Cambridge, MA, MIT Press, 1988 5

Angeles, J., “Fundamentals of Robotic Mechanical Systems”, New York, Springer-Verlag, 1997 8

Craig, J. J., “Introduction to robotics: mechanics and control”, Addison-Wesley, 1989..... 74

dSPACE Installation and Configuration Reference, 2003 31

Luh, J. Y. S., Fisher, W. D, and Paul, R. “Online computational scheme for mechanical manipulators”, *Journal of Dynamic Systems, Meas., Control*, 102: 69-76, 1983 7

Mukerjee, A., “Self-Calibration Strategies for Robot Manipulators”, *Dept. Computer* Science, TR193, Rochester, NY, 1986 6

Paul, R.P., “Robot Manipulators: Mathematics, Programming, and Control”, Cambridge, MA, MIT Press, 1981 8

Sciavicco, L., Siciliano, B., “Modelling and Control of Robot Manipulators”, London, Springer, 2000 8

Siciliano, B., Villani, L., “Robot Force Control”, Boston, MA, Kluwer Academic, 1999..... 8

Spong, M. W., Vidyasagar, M., “Robot dynamics and control”, New York, Wiley, 1989 9

Stramigioli, S., “Modeling and IPC control of interactive mechanical systems : a coordinate-free approach”, London, Springer, 2001 8

W. Schiehlen, "Computer Generation of Equations of Motion" in *Computer Aided Analysis and Optimization of Mechanical System Dynamics,* Springer-Verlag, 1984 85

Yoshikawa, T., “Foundations of Robotics”, Cambridge, MA, MIT Press, 1990..... 8

Publications

An, C.H., Atkeson, C.G., Hollerbach J.M., “Model-Based Control of a Robot Manipulator”, Cambridge, MA, MIT Press, 1988 38

C. Ruoff, "Fast Trigonometric Functions for Robot Control," *Robotics Age,* November 1981 85

Caccavale, F., Chiacchio, P., “Identification of dynamic parameters and feedforward control for a conventional industrial manipulator”, *Control Engineering Practice*, 2:1039:1050, 1994 21

Chasles, M., “Bulletin des Sciences Mathematiques, Astronomiques, Physiques et Chiniques,” 14, *Baron de Ferrusac*, Paris, pp.321-326, 1830 60

Chiaverini, S., Sciavicco, L., “The parallel approach to force/position control of robotic manipulators”, *IEEE Trans. Robot. Automation*, 9:361–373, 1993 15

Chiaverini, S., Siciliano, B., Villani, L., "Force position regulation of compliant robot manipulators" *IEEE Trans. Automat. Contr.,* 39:647-652 1994 19

Chiaverini, S., Siciliano, B., Villani, L., “A survey of robot interaction control schemes with experimental comparison”, *IEEE/ASME Trans. on Mechatronics*, 4:273-285, 1999.... 15, 47

Dagalakis, N. G., Myers, D. R., “Adjustment of robotic joint gear backlash”, *International Journal of Robotics Research*, 4(2): 65-79, 1985 6

De Schutter, J., van Brussel, H., “Compliant robot motion II. A control approach based on external control loops”, *Int. J. Robot. Res.*, 7:18–33, 1988..... 15

De Wit, C. C., Olsson, H., Astrom, K. J., Lischinsky, P., “A new model for control systems with friction”, *IEEE Trans. Automatic Control*, 40:419-425, 1995 39

Denavit, J., Hartenberg, R.S., "A kinematic notation for lower-pair mechanisms based on matrices and quaternion representation.", *Journal of Applied Mechanics,* pp. 215-221, 1955 75
Good, M. C., Sweet, L. M., Strobel, K. L., "Dynamic models for control system design of integrated robot and drive systems", *ASME Journal of Dynamic Systems, Meas., Control*, 107: 53-59, 1985 6
Hamilton, W.R., "Elements of quaternions", *Longmans Green*, London, 1969 75
Hogan, N., "Impeadance control: An approach to manipulation: Part i - theory, part ii - implementation, part iii - applications", *ASME J. of Dynamic Systems, Measurement and Control*, 107:1-24, 1985 ..... 15, 56
Hunt, K., "Kinematic Geometry of Mechanisms", London, Oxford University Press, 1978 .. 10
Luh, J.Y.S., Walker, M.W., Paul, R.P.C., "Resolved-acceleration control of mechanical manipulators", *IEEE Trans. on Automatic Control*, 25:468-474, 1980 21
Mason, M. T., "Compliance and force control for computer controlled manipulators", *IEEE Trans. Syst., Man, Cybern.*, 6:418–432, 1981 15
Poinsot, L., "Sur la Composition des moments et la composition des aires", *J. Ec. Polyt*., Paris, 6, pp.182-205., 1806 62
R. Paul, B. Shimano, G. Mayer, "Kinematic Control Equations for Simple Manipulators", *IEEE Transactions on Systems, Man, and Cybernetics*, vol SMC-11, No. 6, 1981 78
Raibert, M. H., Craig, J. J., "Hybrid Position/Force Control of Manipulators", ASME J. of Dynamic Systems, Measurement and Control, 103:126-133, 1981 15
Romer, G.W., Johnson, M., Driessen, B., "Towards a performance benchmark for rehabilitation robots", *Proceedings of the 1st International Conference On Smart Homes & Health Telematics*, Paris, pp. 158-164, 2003 93
Spong, M., "Modeling and control of elastic joint robots", *IEEE J. of Robotics and Automation*, RA-3:291-300, 1987 ..... 10, 43
Stramigioli, S., Bruyninckx, H., "Geometry and screw theory for robotics", *tutorial from IEEE International Conference on Robotics and Automation*, University of Twente, Seoul, Korea, 2001 59
Takegaki, M., Arimoto, S., "A new feedback method for dynamic control of manipulators", *ASME J. of Dynamic Systems, Measurement, and Control*, 103:119-125, 1981 17
Volpe, R., Khosla, P., "A theoretical and experimental investigation of explicit force control strategies for manipulators", *IEEE Tran.. on Automatic Control*, 38:1634–1650, 1993 15
Wen. J., Murphy. S., "Stability analysis of position and force control for robot arms", *IEEE Tran.. on Automatic Control*, 36:365-371, 1991 17
Whitney, D.E., "Force feedback control of manipulator fine motions", *ASME J. of Dynamic Systems, Measurement, and Control*, 99:91-97, 1977 15
Won, J., Stramigioli, S., Hogan, N., "Comment on "The equivalence of second-order impedance control and proportional gain explicit force control"", *The International Journal of Robotics Research*, pp. 873-875, 1997 106
Yoshikawa, T., "Dynamic hybrid position/force control or robot manipulators - Description of hand constraints and calculation of joint driving force", *IEEE J. of Robotics and Automation*, 3:386- 392, 1987 15
Zollo, L., Siciliano, B., Laschi, C., Giancarlo, T., Dario, P., "An experiment study on compliance control for a redundant personal robot arm", *Robotics and Autonomous Systems*, pp. 101-129, 2003 69

Conference Papers

Salisbury, J.K., "Active stiffness control of a manipulator in Cartesian coordinates", In *Proc. 19th IEEE Conf. on Decision and Control*, Albuquerque, NM, pp. 95-100, 1980 ..... 15, 47

T. Turner, J. Craig, and W. Gruver, "A Microprocessor Architecture for Advanced Robot Control," 14th ISIR, Stockholm, Sweden, October 1984 85

Index